



Norwegian University of  
Science and Technology

# Simulations and Measurements of Streamer discharges near Dielectrics

**Sigurd Gard Midttun**

Master of Science in Physics and Mathematics

Submission date: June 2017

Supervisor: Jon Andreas Støvneng, IFY

Co-supervisor: Robert Marskar, SINTEF Energi  
Nina Sasaki Støa-Aanensen, SINTEF Energi

Norwegian University of Science and Technology  
Department of Physics



# ABSTRACT

A novel numerical fluid model for simulating streamer discharges has been tested and utilized with a two-dimensional triple junction configuration. The triple junction was located at the upper end of a 1 cm dielectric rod, and positive streamers were initiated by applying a constant voltage of 18.5 kV to the triple junction anode. After inception, propagation along the dielectric rod was investigated, and the streamer velocities was estimated to be about 0.05 mm/ns. The streamers were found to be very thin, only spanning across three layers of cells, if the charge density was used as a measurement. This was unexpected, and as far as the author is concerned, such a result has not been reported elsewhere. Most likely, the narrow width of the surface streamers is caused by the fact that only one photon frequency band is included in the model. In the layer of cells closest to the dielectric, a very high charge density with a maximal value of 158.3  $\mu\text{C}/\text{cm}$  was seen. Simulations have also been performed using a 0.5 mm rod-plane gap configuration with a grounded dielectric barrier, displaying similar results for streamers propagating along the dielectric surface. With this configuration, multiple simulations were performed in order to probe how various electron yield coefficients  $\gamma_{\text{ph}}$ , describing photoemission from the dielectric surface, affected the dynamics of the streamers. With the coefficient value  $\gamma_{\text{ph}} = 10$ , the discharge behaved quantitatively different than what was observed when a value of 0.1 and 1 was used. All simulations were performed in a nitrogen-oxygen mixture under normal conditions.

Due to use of an explicit second order Runge-Kutta method for advancing the hydrodynamic equations in time, restrictions on the sizes of the time steps had to be followed to avoid instability. Because of stiffness in the equation set, time steps of the order of  $10^{-13} - 10^{-15}$  was found to be necessary for stability. Another issue with the numerical code was uncovered in form of memory leakage, causing the simulations to crash after approximately 13 000 time-iterations. With these limitations, simulations of streamer propagation along the full lengths of the dielectric surfaces were prohibited.

Also experimental work has been performed with a triple junction configuration similar to that used in the simulations. By means of a high-speed camera with a minimal exposure time of 10 ns, streamer discharges along the dielectric rod was arrested. Based on the experimental data, a lower propagation velocity of 1 mm/ns is estimated. It must however be noted that excess charge present on the rod from earlier experiments could have influenced the estimated lower bound propagation velocity.



# SAMMENDRAG

En nylig utviklet numerisk fluidmodell for å simulere streamerutladninger har blitt testet og brukt til å utføre simuleringer på en trippelpunkt-konfigurasjon. Trippelpunktet var plassert i den øvre enden av en 1 cm lang dielektrisk stav, og positive streamere ble initialisert ved å tilføre trippelpunkt-anoden en positiv spenning på 18.5 kV. Streamer-propagering langs den dielektriske flaten ble så studert, og propageringshastigheten ble anslått til å være rundt 0.05 mm/ns. De observerte streamerne var svært tynne, og med utgangspunkt i ladningstettheten ble streamerne anslått til å kun strekke seg over tre celler i bredden. Dette var uventet, og det ser ikke ut til at lignende resultater finnes i litteraturen. Forklaringen på at streamerne blir så tynne er mest sannsynlig at bare én fotonfrekvens er inkludert i modellen. Videre observeres det en veldig høy ladningstetthet med en maksimalverdi på 158.3  $\mu\text{C}/\text{cm}$  i cellelaget nærmest den dielektriske overflaten. Simuleringer har også blitt utført ved bruk av en stav-plate-konfigurasjon med et 0.5 mm gap og en jordet dielektrisk plate. Også her ble overflate-streamerne observert å være veldig tynne. For å teste hvordan fotoemisjon fra den dielektriske flaten påvirket utladningene, ble det foretatt simuleringer ved bruk av forskjellige effektivitetskoeffisienter,  $\gamma_{\text{ph}}$ , som bestemmer graden av fotoemisjon fra flaten. Med verdien  $\gamma_{\text{ph}} = 10$  ble utladningsforløpet kvalitativt annerledes enn da verdier på 0.1 eller 10 ble brukt. Alle simuleringene ble utført i en blanding av oksygen og nitrogen under normale forhold.

I simuleringene ble det brukt en eksplisitt andreordens Runge-Kutta-metode for å tidsintegrere de hydrodynamiske ligningene. Stabilitetsbetraktninger medfører imidlertid at eksplisitte metoder er forbundet med strenge krav til hvor store tidsstegene kan være. Grunnet stivhet i ligningssettet var det nødvendig å bruke tidssteg av størrelsesorden  $10^{-13} - 10^{-15}$  for å unngå ustabile løsninger. Videre ble det oppdaget at minnelekkasjer i kildekoden hindret simuleringene fra å kjøre mer enn 13 000 tidsiterasjoner. Disse utfordringene førte til at det ikke var mulig å simulere streamer-propagering langs den fulle lengden av de dielektriske flatene.

Det har også blitt foretatt eksperimentelle målinger på en trippelpunkt-konfigurasjon lignende den som ble brukt i simuleringene. Ved hjelp av et høyhastighetskamera med en minste eksponeringstid på 10 ns ble det tatt bilder av streamerutladninger langs den dielektriske staven. Ut fra disse ble en nedre propageringshastighet estimert til 1 mm/ns. De eksperimentelle målingene er imidlertid ikke direkte sammenlignbare med de numeriske målingene, da det under eksperimentet mest sannsynlig allerede forelå en del ladning på den dielektriske staven fra tidligere utladninger.



# PREFACE

This thesis is submitted as a final part of a five-year master's degree programme in Applied Physics and Mathematics at the Norwegian University of Science and Technology (NTNU). The work presented here has been conducted during the 2017 spring semester and amounts to 30 ECTS credits. The focus of this thesis is a novel simulation tool implemented and developed by Robert Marskar at SINTEF Energy for modeling streamer discharges in gases. During the writing of this thesis, Robert has been my main supervisor and I want to thank him for his unparalleled guidance and support. I would also like to thank my other supervisor at SINTEF Energy, Nina Sasaki Støa-Aanensen, and PhD candidate Hans Kristian Hygen Meyer for valuable assistance and guidance in the lab. Furthermore, I am grateful to the members of the "lunch group" for all the fun and interesting breaks we have shared. Lastly, a special thanks to my girlfriend Ingrid for her unconditional support and care.

*Sigurd G. Midttun*

Sigurd G. Midttun  
Trondheim, June 2017





# CONTENTS

<b>Abstract</b>	<b>i</b>
<b>Sammendrag (norwegian)</b>	<b>iii</b>
<b>Preface</b>	<b>v</b>
<b>Contents</b>	<b>vii</b>
<b>1 Introduction</b>	<b>1</b>
1.1 Background and motivation . . . . .	1
1.2 Approach . . . . .	2
1.3 Structure of thesis . . . . .	4
<b>2 Theory</b>	<b>5</b>
2.1 Processes between air particles . . . . .	6
2.1.1 Ionization processes . . . . .	7
2.1.2 Deionization processes . . . . .	9
2.2 Processes at metal electrode surfaces . . . . .	10
2.2.1 Photoelectric emission . . . . .	10
2.2.2 Bombardment of ions and metastable atoms . . . . .	11
2.2.3 Other mechanisms . . . . .	13
2.3 Townsend discharges . . . . .	13
2.3.1 The $\alpha$ -process . . . . .	13
2.3.2 The $\gamma$ -process . . . . .	14
2.3.3 Townsend's breakdown criterion . . . . .	15
2.3.3.1 Townsend's criterion in electronegative gases . . . . .	16
2.4 Streamer discharges . . . . .	17
2.4.1 Streamer formation . . . . .	17
2.4.1.1 Formation of positive streamers . . . . .	18
2.4.2 Streamer propagation . . . . .	20
2.4.3 Streamer characteristics . . . . .	21
2.4.4 Photoionization and other sources of free electrons . . . . .	22
2.4.5 Influence of dielectric surfaces . . . . .	23
2.4.5.1 Polarization effects . . . . .	23
2.4.5.2 Processes at dielectric surfaces . . . . .	23
2.4.5.3 Streamer propagation close to a dielectric surface . . . . .	24
<b>3 Streamer model</b>	<b>27</b>

3.1	The computational domain . . . . .	27
3.1.1	Representation of embedded boundaries . . . . .	27
3.2	Hydrodynamic equations . . . . .	29
3.2.1	Implementation . . . . .	30
3.2.1.1	Computation of the model source terms . . . . .	31
3.2.1.2	Transport coefficients and rate coefficients . . . . .	31
3.2.1.3	Photoionization . . . . .	32
3.2.1.3.1	The multigroup approximation . . . . .	33
3.2.2	Boundary conditions . . . . .	34
3.3	Electrodynamic equations . . . . .	35
3.3.1	Boundary conditions . . . . .	36
3.4	Radiative transfer equation . . . . .	36
3.4.1	The Eddington approximation . . . . .	37
3.4.2	Computation of the RTE source term . . . . .	38
3.4.3	Boundary conditions . . . . .	39
3.5	Scalar conservation equation . . . . .	40
3.6	Surface mechanisms . . . . .	40
3.6.1	Metal surfaces . . . . .	41
3.6.1.1	Anodes . . . . .	41
3.6.1.2	Cathodes . . . . .	42
3.6.1.2.1	Electron yield coefficients . . . . .	42
3.6.2	Dielectric surfaces . . . . .	44
3.6.2.0.1	Electron yield coefficients . . . . .	44
3.7	Numerical method . . . . .	45
3.7.1	Implementation details . . . . .	45
3.7.2	Spatial discretization . . . . .	46
3.7.2.1	Adaptive mesh refinement . . . . .	46
3.7.2.2	The Poisson and Eddington equations . . . . .	48
3.7.2.2.1	Embedded boundary fluxes . . . . .	50
3.7.2.2.2	Solver considerations . . . . .	51
3.7.2.2.3	The AMR multigrid method . . . . .	52
3.7.2.3	The hydrodynamic equations . . . . .	53
3.7.2.3.1	Embedded boundary fluxes . . . . .	54
3.7.3	Temporal discretization . . . . .	54
3.7.3.1	Time stepping method . . . . .	54
3.7.3.2	Time step restrictions . . . . .	55
3.8	Model limitations . . . . .	56
<b>4</b>	<b>Method</b>	<b>59</b>
4.1	Experiments . . . . .	59
4.2	Simulations . . . . .	61
4.2.1	Triple junction geometry . . . . .	61
4.2.2	Rod-plane geometry . . . . .	62
<b>5</b>	<b>Results and discussion</b>	<b>65</b>
5.1	Experiments . . . . .	65

5.2	Simulations . . . . .	67
5.2.1	Triple junction geometry . . . . .	69
5.2.2	Rod-plane geometry . . . . .	72
5.2.2.1	Propagation in air . . . . .	72
5.2.2.2	Propagation along the dielectric surface . . . . .	74
5.3	Evaluation . . . . .	77
<b>6</b>	<b>Conclusion</b>	<b>79</b>
	<b>Bibliography</b>	<b>81</b>



# Chapter 1

## INTRODUCTION

### 1.1 Background and motivation

A streamer is an electrical discharge phenomenon characterized by a narrow and weakly ionized non-thermal plasma channel with a self-propagating head consisting of a thin curved layer of either net positive or negative charge [1, 2]. In air at ground pressure, streamers are formed through electron avalanches in electric fields greater than about 30 kV/cm and propagate with typical speeds of 0.1 – 10 mm/ns [1]. Due to the high concentration of charges in the streamer head, the streamer front is associated with an enhanced electric field. This allows streamers to propagate in their own field in regions with a background field well below the point of breakdown. The work presented in this thesis investigates the dynamics of positive streamers in air at atmospheric pressure, i.e. streamers with a net positively charged head propagating in the opposite direction of the electron drift direction.

Streamers have a wide range of industrial applications due to their ability to activate chemical reactions almost without heating [1]. Examples include production of ozone, water cleaning and removal of pollutants such as SO<sub>2</sub>, NO<sub>x</sub> and fly ash [3, 4, 5]. Another example is the use of cold plasma to break up higher order hydrocarbons and thereby improve combustion efficiencies [6]. Streamers also appear in nature in the form of so-called sprites which form high above thunderclouds at an altitude of about 80 km. The formation of sprites is not yet fully understood, but they are known to be the first self-propagating stage of a lightning discharge [1, 7].

Although streamers may be of great industrial use when induced under controlled conditions, the phenomena can also potentially have destructive effects when occurring uncontrollably. In the high-voltage industry for example, a lot of research is put into preventing streamer development, as streamers are predecessors of electrical sparks, which may cause damage to high-voltage components [2]. A worst-case scenario occurs if a streamer bridges the gap between two high-voltage electrodes (or high-voltage and ground), allowing very large currents to run through the plasma channel. However, also smaller partial discharges may over time cause significant degeneration of high-voltage components, causing their life-time to decay [8]. So-called

triple junctions, where gas, solid insulators and metal conductors are in very close proximity are regarded as weak points in high-voltage gas-insulated systems [8, 9, 10, 11]. At such points, the electric field is enhanced due to increased dielectric polarization of the insulator, making the surrounding local region more susceptible to inception of discharges. Understanding the exact mechanisms and underlying conditions triggering such discharges is still a relatively open field of research. A better insight into these mechanisms might open for improved insulator designs, leading to increased electrical withstand in high-voltage gas-insulated systems.

In recent years, numerical modelling of streamer discharges has gotten a wider attention, both thanks to better and faster numerical algorithms and due to more powerful computers [12]. Streamer dynamics is influenced by a vast number of different physical mechanisms, and through experiments alone it is almost impossible to single out specific mechanisms to measure their relative strength of influence on the streamer propagation. In simulations however, the implemented physical mechanisms may be turned on and off and tuned to fit experiments. In this way, numerical simulation makes it possible to obtain a much deeper understanding of streamer dynamics than what can be obtained only through experiments [1]. However, it must be noted that all numerical models build on simplifying assumptions and approximations. Moreover, only a small number of physical mechanisms are usually implemented, most of which depend on macroscopic parameters whose values are at best approximate. Therefore, numerical simulations are of most value when used to complement and support experimental data. However, performing accurate experiments often requires costly measuring equipment and specially designed set-ups. In this respect, numerical simulations offer a valuable, low-cost and versatile option increasingly being embraced by the industry.

## 1.2 Approach

During the writing of this thesis, both numerical simulations using a newly developed and until now untested streamer code and experimental work have been performed. The goals of this thesis is to

- i) Evaluate, validate and tune the streamer model to fit experimental data.
- ii) Use simulations and experimental data to outline the behaviour of streamer discharges in triple junctions and along dielectric surfaces.

Over the course of this work, several smaller and larger errors in the code have been exposed. In fact, the process of debugging, testing and adjusting the code turned out to be much more time consuming than first anticipated. Subsequently, most of the effort has therefore been concerned with i).

The experimental work was conducted using a triple junction configuration resembling that found within switches in gas-insulated high-voltage systems. The considered configuration consisted of two parallel disk-shaped aluminum electrodes joined by a 1 cm cylindrical dielectric rod of relative permittivity  $\epsilon_r = 4.6$ . The rod was made of polyoxymethylene (POM) with added 25% glass fiber, and the experiments were performed in ambient air under normal pressure and temperature. A pulsed positive direct current (DC) voltage was applied to one of the electrodes,

whereas the other electrode was grounded. Under these conditions, positive streamers were incepted from the triple junction located at the stressed electrode.

Concerning the simulations, two different geometries have been considered. The first geometry was designed as a two-dimensional (2D) replica of the experimental triple junction configuration, allowing for direct comparison between experimental and numerical data. In contrast, the second geometry was a 0.5 mm hemispherically capped rod-plane gap configuration consisting of a parallel dielectric barrier resting on a grounded metal plate. The rod was stressed with a constant positive DC voltage for positive streamer inception. This configuration was chosen because it permits studying how the numerical code performs modeling streamers propagating in air. Furthermore, when the discharges eventually bridge the gas gap, a second dynamical phase where the streamers spread out on the dielectric material is examined.

The streamer code is implemented in a dimensionally independent manner, meaning that switching between 2D and 3D (three-dimensional) simulations only involves updating an input script. The aim was to use 2D simulations for the sake of point i) described above and then run full 3D simulations for ii). However, due to various challenges and lack of time, only 2D simulations were performed. All the simulations were executed using a temperature of 300 K and atmospheric pressure. Moreover, the gas adopted for the numerical simulations was a synthetic air mixture of nitrogen and oxygen in a 4:1 ratio.

Modeling streamers is intrinsically difficult due to the spatial multiscale nature of the phenomenon [1, 3, 13]. Whereas the length of a streamer channel in air at standard temperature and pressure (STP) may be tens of centimeters, there exists a space charge layer surrounding the channel with thickness of only a few micrometers [13]. In order to obtain sufficient numerical resolution, the computational mesh sizes should at least match the physical spatial scales. At the same time, the number of grid points should be kept as low as possible in order to minimize the simulation time and memory usage. The solution to this challenge is use of adaptive mesh refinement (AMR) techniques, allowing the mesh to be locally refined only in regions where finer spatial resolution of the solution is required.

The different streamer simulation models found in the literature may roughly be grouped into one of three categories; kinetic models, fluid (continuum) models or hybrid models (a fourth category might include so-called tree models simulating the fractal structure of streamer branching, but such will not be discussed here) [1, 3, 13]. Kinetic models are based on a microscopic treatment and therefore give the most accurate and detailed description of streamer dynamics. However, such models are computationally much more expensive than fluid simulations, where only macroscopic quantities like average densities, mean velocities and temperature appear [14]. The two main approaches for solving kinetic equations are particle-based methods and direct solver methods for solving the Boltzmann equation describing classical transport phenomena [14]. Particle-based methods, such as Particle-in-Cell [15] and Direct Monte Carlo Simulations [16], are stochastic and involve tracking of individual particles, whereas direct solver methods, such as the Discrete Velocity Method, use a computational grid in phase space. Fluid equations for conservation of mass, momentum and energy can also be applied to streamers, but these models are restricted to the validity of the continuum breakdown approximation. Because of this, fluid models can not describe the initial stages of inception. Hybrid models are designed to maximize computational efficiency without compromising accuracy through joint fluid-kinetic

descriptions. For example, Zabelok et al. [17] have developed an AMR fluid-kinetic simulation tool with automatic cell-by-cell selection of kinetic or fluid solvers based on continuum breakdown criteria. For increased performance, their code is adapted for CPU-GPU systems in order to utilize the great computational power of Graphical Processing Units (GPUs), giving double digit speedups.

The streamer model presented here is formulated within the minimal plasma model, using the fluid approximation. This means that only the spatiotemporal evolution of the volumetric densities of massive species is solved for, leaving transport coefficient as input parameters. In this work, three massive species are considered; electrons, positive ions and negative ions. The ionic species are generic, meaning that they are modeled to roughly account for all the different ions present in air. The hydrodynamic conservation equation for each of these species is nonlinearly coupled to the electric field, which is calculated by first solving Poisson's equation for the electric potential. Furthermore, photon transport is accounted for by solving the radial transfer equation (RTE) in the Eddington approximation. Lastly, a scalar conservation equation is imposed on dielectric boundaries in order to enforce conservation of electrical charges. Internal dielectric and conductor boundaries within the computational domain (embedded boundaries) are accurately described using cut-cell representation<sup>1</sup>.

The elliptic Poisson and RTE equations are solved by using an AMR geometric multigrid solver, whereas the hydrodynamic equations and the scalar equation are advanced in time by using an explicit second order Runge-Kutta method. The elliptic equations are discretized using a finite volume approach. In contrast to many other discretization methods, finite volume schemes are flux conservative. Schemes not sharing this property are in some cases known to produce unphysical results [18]. The hydrodynamic equations are discretized using Godunov's approach with Van Leer limiting. This method is adopted from the field of shock discontinuities in hydrodynamic flows and was chosen because it is associated with very little numerical diffusivity.

### 1.3 Structure of thesis

This thesis is structured as follows: the second chapter starts off by placing streamer discharges into a historical and physical context, before it proceeds with an in-depth description of streamer inception and propagation. The third chapter presents the numerical streamer model, focusing on both derivation of the equations included in the model and on the numerical methods used to solve them. The chapter ends with a review of the approximations and simplifications made and how these place limitations on the model. In chapter four, the conducted experiments and simulations are described in detail. The outcome of this work is presented and discussed in chapter five. Finally, a summary and concluding remarks are provided in chapter six.

---

<sup>1</sup>When solving the Poisson equation, the implementation does currently not support cut-cell representation of dielectric boundaries. See sections 3.1 and 3.3 in chapter 3 for further elaboration.



# Chapter 2

## THEORY

Electrical breakdown of a gas is an unstable, irreversible, and transient phenomenon caused by self-sustained avalanche processes between two electrodes of unequal potential [19, 20]. In gases, breakdown is often seen as a sudden spark resulting from an abnormally high conductivity channel between the electrodes. The breakdown process is intrinsically stochastic and creates a rapid voltage drop across the gap. The electrical breakdown voltage is the critical voltage needed for a breakdown to occur [21]. This thesis focuses on one of the mechanisms that may lead to breakdown, namely the streamer mechanism. However, the actual physical processes involved in a breakdown, such as streamer to leader transitions, will not be discussed.

Paschen's law was empirically developed over a century ago and states that the electrical breakdown voltage  $V_b$  is a function of the product  $pd$  of the gas pressure  $p$  and gap the distance  $d$ , rather than depending on these quantities individually [11]. In the case of uniform fields in gas gaps between two parallel electrodes, the law is in general found to be valid for  $pd$  values ranging from  $4.0 \times 10^{-5}$  atm cm to nearly 3 atm cm [19]. However, deviations from Paschen's law have been measured [22]. Plots of  $V_b$  as a function of  $pd$  are called Paschen's curves, and the curves for air,  $\text{CO}_2$  and  $\text{H}_2$  are given in figure 2.1. Any successful theory trying to explain the mechanisms behind electrical discharges should confine to Paschen's law within the range of its validity and show explicit dependence on the quantity  $pd$ .

Experimental and theoretical studies have shown that there are several mechanisms leading to breakdown, each operating at different values of the product  $pd$  [23]. For extremely low pressures and small gaps, experiments reveal large departures from Paschen's law. Under such conditions, breakdowns occur as a result of evaporation of micro-spikes on the electrode surface caused by a state of thermal instability, and is commonly referred to as vacuum breakdowns [20, 22]. For larger  $pd$  values, breakdowns are highly influenced by the gas particles and occur through very different mechanisms. The Townsend mechanism [24] is dominating for low values of the product  $pd$  (but yet larger than the vacuum breakdown threshold). The process involves electron ionization of gas molecules, forming multiple electron avalanches. For intermediate and high values of  $pd$ , discharges occur through the streamer mechanism of Meek, Loeb and Raether [25, 26, 27], in which a single electron avalanche proceeds to form a dense layer of space charge.

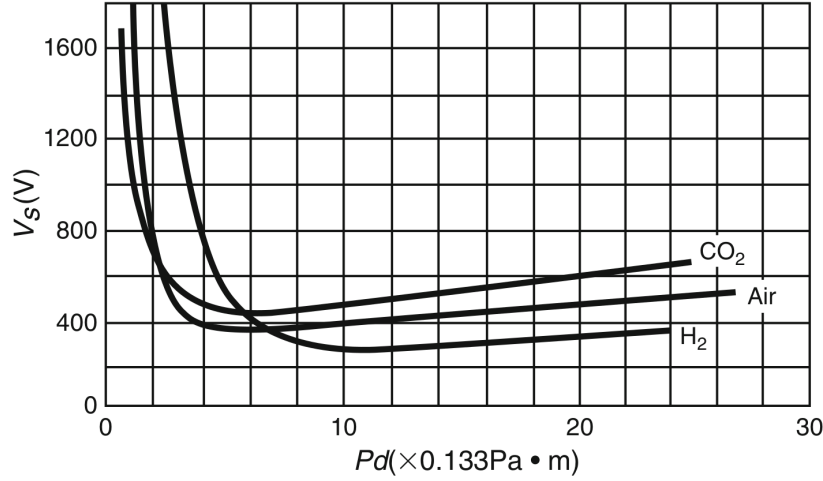


**Figure 2.1:** Paschen's curves for air,  $\text{CO}_2$  and  $\text{H}_2$ . Here,  $V_s$  is the gas breakdown potential between two parallel electrodes at  $T = 20^\circ\text{C}$ . The figure is taken from [21].

The space charge layer is then able to propagate in its own electric field due to various processes in the streamer front. According to Meek [28], the streamer mechanism replaces the Townsend mechanism when the  $pd$  value reaches about  $pd \sim 200 \text{ mm Hg}$  or  $pd \approx 0.3 \text{ atm cm}$  in air. However, the transition is soft, and for a range of  $pd$  values both mechanisms may be active, as reported by Osmokrovic et al. [20] for the case of  $\text{SF}_6$ . Therefore, the value of  $pd$  at which the transition occur for a specific gas is not universally agreed upon. Subsequently, different transition values, such as  $1 \text{ atm cm}$  [29] and  $2.6 \text{ atm cm}$  [23] for the case of air may be found in the literature.

It must be emphasized that the transition to a Townsend discharge or a streamer discharge is not in general synonymous with a complete gas breakdown. Although this is normally the case for uniform fields, it is not true for non-uniform fields, where various discharges may take place long before complete breakdown [23]. For example, partial discharges in form of corona discharges are commonly encountered in rod-plane geometries, producing strong non-uniform fields. Coronas may be observed as a faint glow localized around the rod tip, where the background electric field is strongest.

All simulations presented in this thesis are performed in non-uniform electric fields with the respective  $pd$  values  $0.1$  and  $1 \text{ atm cm}$ . Before proceeding with a more detailed description of the Townsend and streamer mechanisms, the next sections outline some important processes on which these mechanisms rely.

## 2.1 Processes between air particles

In the absence of any significant electric fields, air is a very good insulator at standard temperature and pressure [23]. At any instant there is an ongoing wealth of different interactions between the air particles. Under steady-state conditions, an equilibrium between different ionization and de-ionization (decay) processes exists. This equilibrium is referred to as the background ioniza-

tion, as there under normal conditions always exists a minimum of ionized positive and negative air molecules due to various mechanisms. However, at larger fields, this equilibrium shifts towards increasing levels of ionization. This happens because charged particles gain kinetic energy from the electric field, creating more energetic collisions between the gas particles. Collisions involving electrons are the most important source of gas ionization among massive particles. Due to their low mass, electrons are very easily accelerated in electric fields, and therefore they rapidly gain kinetic energy. This property is quantified through the electrical mobility  $\mu$ , defined as [23]

$$\mu = \frac{u}{E}, \quad (2.1)$$

where  $u$  is the drift velocity in the direction of the field and  $E$  is the magnitude of the electric field.

Collisions between the air particles (neutral molecules, ions, electrons and photons) may be classified as either elastic or inelastic. Elastic collisions are associated with only transfer of kinetic energy, whereas for inelastic collisions, some of this energy is transferred as internal potential energy [23]. If the potential energy received from inelastic collisions are greater than the ionization energy of the receiving molecule, ionization will occur, i.e., a free electron and a positive ion will be created. However, the energy absorbed by the receiving molecule is often only large enough to excite the molecule into a higher vibrational, rotational or electronic state [2]. As a result of quenching of the excited state, the excess energy may after a short time (typically  $10^{-9}$  s) be radiated in a de-excitation process, creating a photon with energy  $h\nu$ , corresponding to the difference between the excited state energy and a lower state energy of the molecule. Here,  $h = 6.63 \times 10^{-34}$  Js is the Planck constant and  $\nu$  is the photon frequency.

De-activation of an excited state may also occur through non-radiating processes. Such includes collisional quenching (the excess energy of the excited state is transferred to a second body), molecular dissociation (the excess energy is used to split the excited molecule) and vibrational de-excitation (the excess energy is transferred into molecular vibrational energy). Usually, non-radiative de-excitation mechanisms dominate, because they are faster than radiative de-excitation. For example, vibrational de-excitation typically occur within 100 fs. Consequently, most molecules therefore absorb photons within a much broader energy range than what they emit [30].

Excitation can occur as a result of numerous types of energy-transferring processes. Of most significance to this thesis is excitation by electron impact and photo excitation. Some of these processes are summarized in table 2.1.

### 2.1.1 Ionization processes

Table 2.2 presents some important ionization processes. These are ionization by electron impact, photoionization and electron detachment. As discussed in later sections, ionization by electron impact is arguably the most essential process relating to both Townsend and streamer discharges, because it gives rise to cascade effects called electron avalanches. Photoionization is of special

Process	Description
$e^- + A \rightarrow A^* + e^-$	Excitation by direct electron impact
$h\nu + A \rightarrow A^*$	Photo excitation

**Table 2.1:** Two important excitation processes.

importance for propagation of positive streamers in air, because it serves as a nonlocal source of free electrons. In contrast, ionization by electron impact is a local process [1]. It must be noted that impact ionization may either occur in a direct or in a stepwise fashion [31]. In the direct case, ionization occur because the incident particle carry an energy greater than the ionization energy of the receiving molecule. However, in the latter case, ionization is achievable even if the incident particle carry an energy less than the ionization threshold. Such is possible if the molecule receiving the energy already was in an excited state due to previous collisions.

Under normal conditions, ionization by ion impact does not occur because ions lose too much kinetic energy in elastic collisions. They are therefore unable to gain the critical energy needed for ionization from the electric field [23]. Also, thermal ionization may under room temperatures be neglected, as this mechanism is only significant at temperatures above 4 000 K.

Another source of free electrons is electron detachment from negative ions. In air at STP, a share of the ionized electrons is found attached, mainly to oxygen molecules. However, in the presence of electric fields, these electrons detach from  $O_2^-$  and become available as unbound electrons [1].

Process	Description
$e^- + A \rightarrow A^+ + 2 e^-$	Ionization by direct electron impact
$h\nu + A \rightarrow A^+ + e^-$	Photoionization
$e^-/h\nu + A^* \rightarrow A^+ + 2 e^-$	Stepwise ionization by electron/photon impact
$A^- + A \rightarrow A + A + e^-$	Two-body collisional electron detachment
$A^- + A + A \rightarrow A + A + A + e^-$	Three-body collisional electron detachment

**Table 2.2:** Some important ionization processes.  $A$  denotes a generic molecule with ionization states  $A^+$  and  $A^-$ , whereas  $A^*$  denotes an excited molecule.

### 2.1.2 Deionization processes

In deionization processes, free electrons and ions are removed from the gas. This occurs through three main mechanisms: recombination, attachment and diffusion [23]. Regarding the last mechanism, charges are not strictly removed, but rather replaced. Diffusion is a result of concentration gradients and applies to all gas particles with a non-uniform concentration. However, diffusion of ions are often neglected in computer models, as this process is slow within typical streamer propagation time frames. A summary of some of the most significant deionization processes is presented in table 2.3.

Recombination is the mechanism where positive and negative charges recombine to form neutral atoms or molecules. The excess energy may be released as a photon (radiative recombination) or transferred to a third body  $B$  (three-body recombination). Recombination may occur between electrons and positive ions or between a positive and a negative ion (ion-ion recombination) [31].

Electron attachment is the reverse of electron detachment, as previously discussed. In this process, electrons attach to neutral molecules, forming negative ions. This is only possible for molecules with high electron affinities, i.e for molecules where the ion state is less energetic than the neutral state [23]. Molecular oxygen, for example, has an electric affinity of nearly 0.5 eV [31]. The excess energy associated with attachment processes may be released through radiation, absorbed by a third body or used to dissociate the molecule. In air, the most electronegative molecules are  $O_2$ ,  $CO_2$  and  $H_2O$  [2]. Under similar conditions, the density of free electrons is therefore lower in humid air than in dry air. Consequently, the air humidity affects how easily streamers are created, as streamers need a certain density of free electrons in order to form and propagate [21, 32].

Process	Description
$e^- + A^+ \rightarrow A + h\nu$	Radiative recombination
$e^- + A^+ + B \rightarrow A + B$	Three-body recombination
$e^- + (AB)^+ \rightarrow A + B + h\nu$	Dissociative recombination
$A^+ + B^- \rightarrow A + B$	Ion-ion recombination
$e^- + A \rightarrow A^- + h\nu$	Radiative attachment
$e^- + A + B \rightarrow A^- + B$	Three-body attachment
$e^- + AB \rightarrow A^- + B$	Dissociative attachment

**Table 2.3:** Some important deionization processes involving recombination and electron attachment.

## 2.2 Processes at metal electrode surfaces

In most experimental setups, discharges are studied between two metal electrodes [31]. By definition, the discharge current runs from the *anode* to the *cathode*. The two electrodes play a major role in the unfolding of a discharge; their geometries and voltages determine the electric field distribution, and they act as both sources and sinks of charged particles.

As will be discussed below, there are several mechanisms that can cause an electron to be liberated from the surface of an electrode. For all of these mechanisms, an important quantity is the material work function  $\phi$ . In the case of metals,  $\phi$  is defined as the minimal energy required to remove an electron from the material surface [19]. At zero temperature, this energy is equal to the difference between the vacuum energy (the potential energy just outside of the metal surface) and the Fermi level energy (the energy of the highest occupied state in the metal). Typical work functions for metals such as aluminum, copper and iron are in the range 4 – 5 eV. See table 2.4 for exact values. It must be noted that the work function is not a property of the bulk of the metal, but rather a property of the surface, determined by the top few layers of atoms. Therefore,  $\phi$  is very sensitive to surface contamination of foreign atoms. Depending on the degree of contamination, the work function can be raised or lowered by as much as 2 eV [19]. Also, the effectiveness of the mechanisms described in the following sections largely depend on the roughness of the metal surface.

Metal	Symbol	Work function $\phi$ (eV)
Platinum	Pt	5.65
Gold	Au	5.10
Beryllium	Be	4.98
Copper	Cu	4.65
Iron	Fe	4.50
Aluminum	Al	4.28
Silver	Ag	4.26
Magnesium	Mg	3.66
Sodium	Na	2.75
Potassium	K	2.30
Caesium	Cs	2.14

**Table 2.4:** A selection of work functions  $\phi$  for different metals. The values are taken from [33].

### 2.2.1 Photoelectric emission

If a photon incident on a metal surface carries an energy  $h\nu$  greater than the metal work function  $\phi$ , an electron may be liberated from the material surface upon absorption of the photon [21].

Such an event is called photoelectric emission, or just photoemission for short. Any excess energy is converted to kinetic energy  $E_k$  according to the formula

$$E_k = h\nu - \phi. \quad (2.2)$$

The photoemission yield  $\gamma_{ph}$  of a metal measures the number of electrons liberated per photon incident on the surface. Some experimental data for various metals is displayed in figure 2.2. As expected, the magnitudes of the yield coefficients increase with increasing photon energies. Comparison with table 2.4 reveals that metals of lower work functions release electrons at lower energies than metals of higher work functions, in agreement with the above discussion.

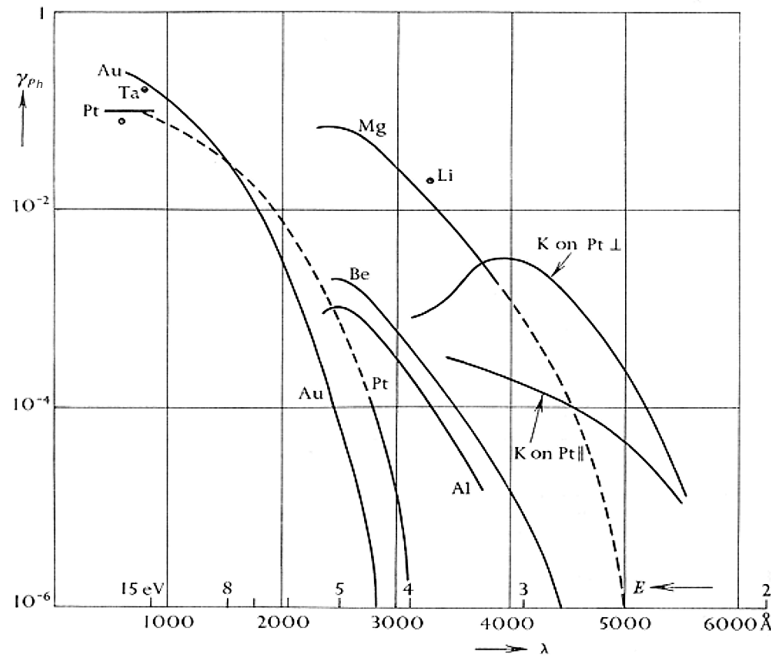


**Figure 2.2:** Experimental photoemission yields  $\gamma_{ph}$  for various metals. The figure is taken from [34].

### 2.2.2 Bombardment of ions and metastable atoms

Due to the electric field between the electrodes, positive ions are accelerated towards the cathode, and negative ions and electrons are accelerated towards the anode. Upon impact with the electrode, they may cause liberation of an electron from the metal surface. Bombardment of positive ions is arguably the most important cathode process and forms the foundation of the Townsend theory.

The interaction between a metal surface and a positive ion must be described quantum mechanically, and the release of an electron occurs through a process called Auger neutralization [35]. This process is possible if the bombarding ion has a vacant quantum state of lower energy than the Fermi energy of the metal. Then, an electron from the metal may tunnel into this lower state, and thereby neutralize the ion. The excess energy corresponding to the energy difference

between the metal and atom states may further be absorbed by a nearby electron in the metal. If the absorbed energy is sufficiently high, the electron may escape the metal. The net result is thus neutralization of the ion, followed by the release of an electron from the metal surface.

A similar process called Auger deactivation may occur when a metastable atom gets sufficiently close to a metal surface [35]. Such atoms are excited atoms with a much longer life expectancy than normal (up to  $10^{-4} - 10^{-2}$  s) [21]. As with Auger neutralization, the first step in an Auger deactivation process is tunneling of an electron from a higher metal energy state into a lower atom energy state. However, in the latter process, the excess energy is not transferred to an electron in the metal, but rather to the excited atomic electron. If the excess energy is large enough, this electron may upon absorption gain enough energy to break free from the atomic state.

The maximum kinetic energies  $E_{\max}$  possible for the released electrons to obtain due to the above processes can be described by the equations [35]

$$E_{\max}^n = E_i - 2\phi, \quad (2.3a)$$

$$E_{\max}^d = E_{\text{ex}} - \phi. \quad (2.3b)$$

Here, the superscripts n and d denote Auger neutralization and deactivation respectively. Moreover,  $E_i$  is the ion ionization potential, and  $E_{\text{ex}}$  is the metastable atom excitation energy.

Note that the above described processes do not depend on the kinetic energies of the incident ions. In this work, the ion kinetic energies are less than 1 eV, and kinetic effects do first become significant at 10 – 100 eV [35]. Consequently, kinetic ejection of electrons can safely be neglected.

Analogues to the photoemission yield, an ion bombardment yield  $\gamma_{\text{ion}}$  and a metastable atom bombardment yield  $\gamma_{\text{met}}$  may be defined as the number of electrons emitted from the metal surface per ion impact and per metastable atom impact respectively. On clean metal surfaces surrounded by an atomic gas, the ion yield coefficient can be estimated as [34]

$$\gamma_{\text{ion}} \approx (0.016/\text{eV})(I - 2\phi), \quad (2.4)$$

where  $I$  is the gas ionization energy. In air, the dominant species is nitrogen with a roughly 80 % share, and the nitrogen ionization energy is 15.6 eV. Moreover, a typical metal work function may be taken as 4.5 eV from table 2.4. Plugging these values into the above equation, and thereby allowing the expression to be extended to the case of molecular gases gives

$$\gamma_{\text{ion}} \approx 0.11. \quad (2.5)$$

It must be emphasized that this is a very rough and general estimate for the ion bombardment yield at a metal surface surrounded by air.



Concerning the metastable ion yield coefficient, experiments have been conducted for various types of metastable atoms and metal surfaces [36, 37]. Depending on the type of atom and metal, in addition to the condition of the metal surface, the magnitude of the yield coefficient was determined to be in the range

$$\gamma_{\text{met}} \approx 0.1 - 1. \quad (2.6)$$

### 2.2.3 Other mechanisms

Another mechanism capable of liberating an electron from a metal surface is thermionic emission caused by metal heating. However, this mechanism is negligible at room temperature, because the potential barrier represented by the work function is usually too high [31]. In the presence of strong electric fields, the potential barrier is however known to be lowered. This phenomenon is called the Schottky effect, and can lead to a significant increase in thermionic emission at STP if the electric field is greater than  $1 - 10 \text{ MV/cm}$  [23, 31].

Both the barrier height and thickness are reduced in the presence of strong electric fields. This allows quantum mechanical tunneling of electrons to yield a significant contribution to the emission current when the field reaches the magnitudes given above. This mechanism is referred to as field emission and was first investigated by Fowler and Norheim [38].

## 2.3 Townsend discharges

The Townsend mechanism was developed by J. S. Townsend in the early 1900s in order to explain breakdown in gases in uniform electric fields at low values of the product  $pd$ . His theory is based upon two main processes, quantitatively described through the coefficients  $\alpha$  and  $\gamma$  [21].

### 2.3.1 The $\alpha$ -process

The quantity  $\alpha$  is Townsend's first ionization coefficient, defined as the average number of ionizing collisions made by one electron per unit length along the direction of the electric field [19]. It can be shown [22] that  $\alpha$  in general depends on the scalar value of the electric field  $E$  and the gas pressure  $p$  in the following way:

$$\frac{\alpha}{p} = f_1 \left( \frac{E}{p} \right). \quad (2.7)$$

By using a model based on simplifying assumptions about electron collisions with neutral molecules, the function on the right hand side of equation (2.7) may be derived [22] to have the form

$$f_1\left(\frac{E}{p}\right) = A \exp\left(-\frac{B}{E/p}\right), \quad (2.8)$$

where  $A$  and  $B$  are constants to be determined experimentally. Experiments have shown that this expression is valid for a limited range of  $E/p$  [19].

In order to mathematically describe the effect of electron ionization (the  $\alpha$ -process), it is necessary to first define a few quantities. In what follows,  $n$  is the number of electrons at a distance  $x$  from the cathode and  $dn$  is the corresponding infinitesimal change in this quantity over an infinitesimal distance  $dx$  along the field direction. Not accounting for any other ionization or deionization processes, the differential equation governing the growth of electrons may be stated as

$$dn = \alpha n dx. \quad (2.9)$$

Integration yields

$$n = n_0 e^{\alpha x}, \quad (2.10)$$

where  $n_0$  is the number of initial electrons at the cathode. If  $\alpha > 0$ , the number of electrons will increase exponentially with  $x$ , and the process is referred to as an electron avalanche [21]. Since the electrical current  $I$  is proportional to  $n$ , the above equation may be restated as

$$I = I_0 e^{\alpha d}, \quad (2.11)$$

where  $d$  is the gap distance between two parallel electrodes. For non-uniform fields, the factor  $\alpha x$  in the exponential term should be replaced by an integral [21], giving

$$I = I_0 \exp\left(\int_0^d \alpha dx\right). \quad (2.12)$$

This expression is only valid if  $\alpha(x) > 0$  over the entire gap. However, unstable large currents due to initial electrons at the cathode does not lead to gas breakdown. In order for breakdown to occur, the process needs to be self-sustained, meaning that the discharge phenomenon can be maintained without an external ionization source [21]. For this to happen, Townsend pointed out that a second process needs to be active at the cathode, namely the  $\gamma$ -process.

### 2.3.2 The $\gamma$ -process

As mentioned earlier on in section 2.2, various mechanism such as ion bombardment, bombardment of metastable atoms and photon impact may liberate secondary electrons from the cathode surface.  $\gamma$  is known as Townsend's second ionization coefficient and measures the effectiveness

of these processes. It is defined as the average number of electrons released from the cathode per incident positive ion [23]. As the definition may suggest,  $\gamma$  did originally only describe bombardment of positive ions. However, it can be shown that inclusion of more mechanisms does not alter the form of equation (2.14) presented below. Therefore it is common to absorb the electron yield coefficients associated with all mechanisms leading to secondary electrons at the cathode into  $\gamma$  [22, 23]. I.e.

$$\gamma = \gamma_{\text{ion}} + \gamma_{\text{met}} + \gamma_{\text{ph}} + \dots \quad (2.13)$$

With a continuous supply of additional electrons at the cathode, the current in a gap of length  $d$  between two planar electrodes is given by the expression [22]

$$I = I_0 \frac{e^{\alpha d}}{1 - \gamma(e^{\alpha d} - 1)}. \quad (2.14)$$

If  $\gamma$  is zero, the expression reduces to equation (2.11) as it should. In general, also  $\gamma$  is a function of  $E/p$  [22], i.e.

$$\gamma = f_2\left(\frac{E}{p}\right). \quad (2.15)$$

However,  $\gamma$  is usually deemed a constant [39].

### 2.3.3 Townsend's breakdown criterion

For a breakdown to occur, the Townsend criterion states that the current  $I$  should approach infinity. This happens if the denominator in equation (2.14) is equal to zero. I.e.

$$1 - \gamma(e^{\alpha d} - 1) = 0, \quad (2.16)$$

or

$$\gamma(e^{\alpha d} - 1) = 1. \quad (2.17)$$

The physical interpretation of this condition is as follows: An initial electron is due to the  $\gamma$ -process created at the cathode and then accelerated towards the anode because of the electric field. Assuming that  $\alpha > 0$ , this electron gives rise to an electron avalanche, creating  $(e^{\alpha d} - 1)$  positive ions and electrons (the “ $-1$ ” is due to the fact that no neutral molecule was ionized when the initial electron was liberated from the cathode surface). The positive ions created are then accelerated towards the cathode, and the associated probability that a second electron will be liberated from the cathode surface is therefore  $\gamma(e^{\alpha d} - 1)$ . If this probability is greater than one, each avalanche will on average give rise to a secondary avalanche, which again will give

rise to a third avalanche and so on. The process is then said to be self-sustained [31].

Since the term  $e^{\alpha d}$  is much greater than 1, the breakdown criterion is usually stated as

$$\gamma e^{\alpha d} = 1. \quad (2.18)$$

As both  $\alpha/p$  and  $\gamma$  is a function of  $E/p$  (equations (2.7) and (2.15)), the above expression may be written as

$$f_2 \left( \frac{E}{p} \right) \exp \left( f_1 \left( \frac{E}{p} \right) pd \right) = 1. \quad (2.19)$$

Moreover, in uniform fields between two parallel electrodes, the applied voltage  $V$  is given by the relation  $V = Ed$  [22]. Consequently, equation (2.19) can be restated as

$$f_2 \left( \frac{V_d}{pd} \right) \exp \left( f_1 \left( \frac{V_d}{pd} \right) pd \right) = 1, \quad (2.20)$$

where  $V_d$  is the breakdown voltage. If solved for  $V_d$ , the above equation gives the relation

$$V_d = f(pd), \quad (2.21)$$

which is in full accordance with Paschen's law. Experimental and theoretical predicted breakdown voltages have been found to give close agreement for low  $pd$  values (see the introductory discussion) [22].

### 2.3.3.1 Townsend's criterion in electronegative gases

As given by equation (2.18), the criterion does not take into account deionization processes such as electron attachment and electron-ion recombination, removing free electrons from the gas. In strongly electronegative gases, such as  $\text{SF}_6$ , attachment is significant and can be quantified by the electron attachment coefficient  $\eta$  denoting the average number of electron attachments made by one electron traveling a unit distance along the field direction [19].  $\eta$  is also a function of  $E/p$  [39], and it can be shown that the breakdown criterion with the additional inclusion of attachment may be approximated with an equation similar to eq. (2.18) and reads [23]

$$\gamma e^{\bar{\alpha} d} = 1. \quad (2.22)$$

Here,  $\bar{\alpha} = \alpha - \eta$  is the effective electron ionization. Taking the logarithm and extending the above criterion to be valid for non-uniform fields ( $\bar{\alpha} d \rightarrow \int_0^d \bar{\alpha} dx$ ), equation (2.22) may be rewritten as

$$\int_0^d \bar{\alpha} dx = \ln \left( \frac{1}{\gamma} \right) = K, \quad (2.23)$$

where  $K$  is a constant. The right hand side of (2.23) may be approximated to be constant because  $\gamma$  is usually very small (less than  $10^{-2} - 10^{-3}$ ), meaning that  $1/\gamma$  is a large number. Although  $\gamma$  varies with different cathode surfaces and are sensitive to changes in the gas pressure and the electric field, the relative change in  $\ln(1/\gamma)$  is normally not too big. For Townsend discharges, the value of  $K$  is therefore typically within the range  $K = 8 - 10$  [23, 31, 40].

## 2.4 Streamer discharges

As stated in the introduction, the Townsend mechanism is unable to explain experimental results obtained at intermediate and high values of the product  $pd$ . Some of the most important, among several observations, that lead to the development of the streamer theory was the recorded mismatch in time lags between experimental and theoretical values between the first electron avalanche process and breakdown. Furthermore, it was evident that the breakdown voltage seemed to be independent of the nature of the cathode [28]. Breakdowns were for example recorded to occur long before the relative slow ions could reach the cathode and liberate secondary electrons [25]. These findings concluded that the  $\gamma$ -process could not possibly be a significant mechanism for breakdown at such  $pd$  values, and therefore ruined the foundation on which the Townsend theory is built.

### 2.4.1 Streamer formation

In contrast to Townsend discharges, which are formed through multiple electron avalanches, it only takes a single electron avalanche to form a streamer [19]. However, it is likely that more than one avalanche in practice is needed to form the background from which the final avalanche proceeding to create the streamer is conceived from [41]. The concept of streamer inception by multiple avalanches applies especially to positive streamers created near a sharp electrode or dielectric surface in non-homogeneous fields (corona discharges) [1].

The key insight provided by Meek, Loeb and Raether was that the numerous positive and negative charges created by electron avalanches should, if grouped densely enough, have a profound distortion effect on the electric field in the vicinity of the avalanche head [26]. A sketch of such a situation is given in figure 2.3, showing an electron avalanche in a homogeneous background field between two parallel electrodes. The total number of electrons in the avalanche head,  $e^{\alpha x}$ , is so large that the charges distort the uniform background field. The heavier ions usually move with velocities more than two orders of magnitude less than the electrons and can therefore be considered stationary during the time it takes for the avalanche to cross the gap [22]. The ions are thus left behind while the front of the avalanche proceeds as depicted.

The Meek criterion states that a streamer will form when the field in the avalanche front due to the space charge is comparable to the applied background field [28]. In air at atmospheric pressure,

an ion density of around  $7 \times 10^{11}$  ions/cm<sup>3</sup> is found to give the necessary field distortion [26], corresponding to about  $10^8$  electrons in the avalanche tip [1, 11, 23]. When this happens, electron trajectories in the vicinity of the avalanche front will be governed by both the field set up by the space charge and the field produced by the applied voltage. The development of streamers is influenced by several factors, such as the applied voltage, the gas pressure, the field gradients, the geometry and curvatures of electrodes and air humidity, in addition to the presence of possible dielectric surfaces. According to these factors, either positive or negative streamers may be formed.

For so-called mid-gap streamers, formed in uniform fields between two parallel electrodes, both a positive and negative streamer emerge from the same electron avalanche [22]. This occurs when the space charge density in the avalanche front reaches the critical number needed for streamer inception. The negatively charged avalanche front will then transition into a negative streamer propagating towards the anode, while the positive ions left behind develop into a positive cathode-directed streamer. This thesis will in the following focus on the formation of positive streamers.

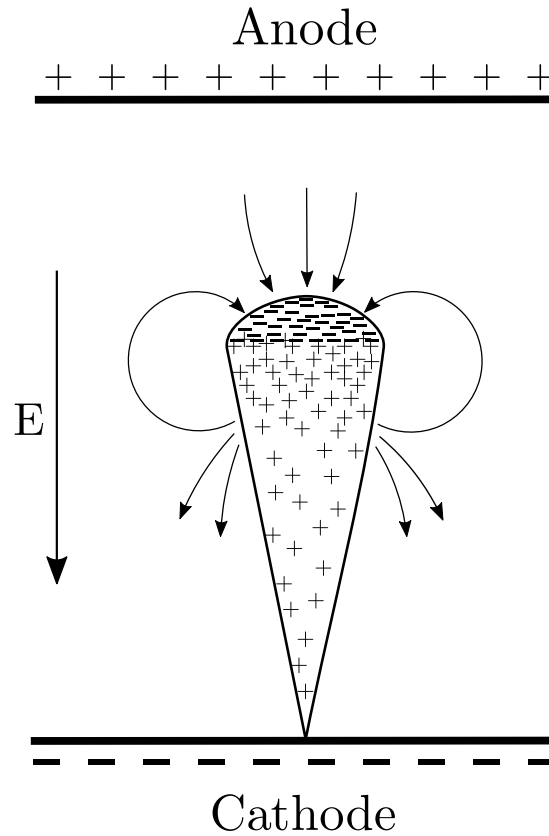


**Figure 2.3:** Illustration of an electron avalanche with associated electric field lines indicated. The figure is based on [22].

#### 2.4.1.1 Formation of positive streamers

If the space charge density in the avalanche front does not reach the critical number needed for a mid-gap streamer to form, the avalanche will proceed until it collides with the anode, leaving

behind only a dense cloud of positive ions. If their numbers and density grows sufficiently, mainly due to photoionization and electron impact ionization, a positive streamer will form at the anode and propagate towards the cathode [28].

Assuming that the avalanche front may be modeled as a spherical cloud of electrons, the critical field distortion needed for streamer inception is given by the Meek criterion, and may be stated as

$$E_r = CE, \quad (2.24)$$

where  $E_r$  is the radial field due to the space charge,  $E$  is the applied background field and  $C \sim 1$  is a constant. Loeb and Meek showed that  $E_r$ , in the case of avalanches in air, is given by

$$E_r = \kappa \frac{\alpha e^{\alpha x}}{(x/p)^{\frac{1}{2}}}. \quad (2.25)$$

The above equation was obtained by using an approximate expression for the ratio of the electron diffusion to the electron mobility, and the approximation was finally determined on the basis of experimental measurements, yielding [40]  $\kappa = 4.815 \times 10^{-8} \text{ kV (mm/bar)}^{\frac{1}{2}}$ . See [22] for a full derivation. As defined earlier,  $\alpha$  is Townsend's first ionization constant,  $p$  is the gas pressure and  $x$  is the distance propagated by the avalanche. For slightly non-uniform fields, the exponent  $\alpha x$  should be replaced by an integral, and the multiplication factor  $\alpha$  should be evaluated at the avalanche front. Of course, the assumptions and approximations leading to the expression for  $E_r$  do not fully conform to reality. For example, the distribution of positive ions in the avalanche front is not really spherical, but rather oval, as electrons in the tip of the avalanche are increasingly accelerated, while the rear electrons are retarded, due to the influence of the space charge field [22]. The field distortion is therefore strongest along the axis of propagation. Moreover, the magnitude of  $C$  to be used in the above criterion is debatable and values in the range  $C \approx 0.1 - 1$  have been proposed [22]. However, the equation is not too sensitive for variations in  $C$ , and with  $E_r$  given by equation (2.25), Meek's criterion has proven to yield breakdown voltages differing a maximum of 6% from experimental data obtained under atmospheric pressure for a range of  $pd$  values up to  $pd = 10 \text{ atm cm}$  [40]. When basing the calculation of  $\kappa$  in equation (2.25) on a different set of experimental data, yielding  $\kappa = 5.6 \times 10^{-5}$ , a maximum of 3 % deviation from empirical observations is achieved [40].

More sophisticated models have been developed for  $E_r$ , and also for the streamer onset criterion itself. For example, Loeb has developed a more rigorous criterion which also includes the effect of photoionization [22]. However, all the proposed models include the factor  $e^{\int_{\Gamma} \bar{\alpha} dx}$ , describing the number of electrons at the avalanche tip (an integral formulation and the effective ionization coefficient  $\bar{\alpha}$  is used for generality). Since this factor is so dominating, the models may in effect be reduced to a single semi-empirical formula [41], given by

$$\int_{\Gamma} \bar{\alpha} dx = \ln(N_c) = K. \quad (2.26)$$

Here,  $N_c$  is the critical number of electrons at the avalanche tip needed for streamer inception, and  $K \approx 18 - 20$  is a dimensionless parameter to be determined experimentally. The integration path  $\Gamma$  should be taken along the strongest field line, provided  $\bar{\alpha} > 0$ . In fact, the above expression is so widely used in practice that it is only referred to as “the streamer criterion” [41]. For air at atmospheric pressure, a typical streamer inception field strength is 26 kV/cm, and the integration length is usually a few millimetres [42].

In strongly non-uniform fields surrounding sharp electrode geometries, Townsend’s first ionization coefficient  $\alpha$  may only be greater than zero in a small region close to the electrode, where the field is very strong. If a positive voltage is applied to the sharp electrode, positive streamers are not formed from single electron avalanches starting at the cathode, but rather from multiple avalanches originating closely to the electrode [1]. As the electrons are drawn into the anode, this cumulative process soon creates a dense layer of positive ion space charge which may transform into a positive streamer when the density reaches the critical value [26].

## 2.4.2 Streamer propagation

Streamers are self-propagating, i.e. propagation is initiated and maintained through local mechanisms taking place in and around the streamer head and sustained by the strong space charge field associated with the streamer front. The field distortion effect is similar for both positive and negative streamers, and leads to an enhanced field in front of the streamer head, and a reduced field behind it. Using the Meek criterion (2.24), the field just in front of the streamer is  $E(1 + C)$ , and the field just behind the streamer head is  $E(1 - C)$ . As described above,  $E$  is the scalar value of the external field. However, it must be emphasized that the field lines associated with a positive streamer points in the opposite direction compared to the field lines associated with a negative streamer. Inside the streamer tip, the most prominent processes are intense electron ionization and photoionization, caused by the strong electric field [32].

Both positive and negative streamers advance as a result of multiple electron avalanches in the streamer front. However, the exact mechanisms are different. Negative streamers advance due to a rapid outwards acceleration of electrons constituting the streamer head, creating numerous electron avalanches directed away from the tip [22]. Positive streamers, on the other hand, propagate as a result of electron attraction of the positively charged streamer head. The electrons originate mainly from the region in front of the streamer, producing multiple avalanches directed towards the positive streamer head. Due to the enhanced field, electron ionization is very effective, and the avalanches grow quickly. In air at atmospheric pressure, the minimum field required for ionization (and development of electron avalanches) is 26 kV/cm [32]. The electrons are immediately neutralized when colliding with the positive charges, leaving behind a dense region of positive ions. Therefore the front shifts, and in this way the advancement of positive streamers may be regarded as a propagating wave of space charge [32]. See figure 2.4 for an illustration of the propagation mechanisms for positive and negative streamers respectively.



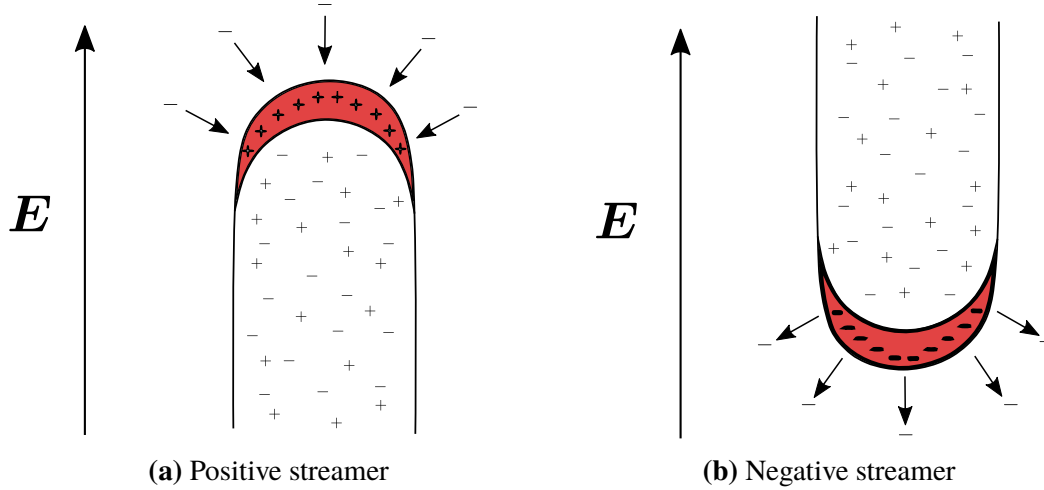


**Figure 2.4:** Illustration of the propagation mechanisms of positive and negative streamers. Positive streamers propagate as a result of the formation of multiple electron avalanches directed into the streamer head (red color). For negative streamers on the other hand, the electron avalanches are formed in the streamer head and are directed outwards.

### 2.4.3 Streamer characteristics

Because electrons in negative streamers move outwards, negative streamer fronts are much more diffusive than the fronts of positive streamers, where the incoming avalanches contribute to maintain their shape [1]. With a broader and less concentrated streamer head, the field enhancement is reduced, resulting in lower ionization rates. Moreover, for negative streamers the electron avalanches always propagate into lower fields, as the field enhancement is reduced with increasing distance from the streamer head. The electron multiplication in the avalanche tips are thus decreasing as the avalanches evolve. For positive streamers, on the other hand, electron avalanches are always propagating into increasing fields, and the creation of electron/ion pairs reaches a maximum just when the avalanches collide with the streamer front. Negative streamers therefore require higher background fields than positive streamers in order to propagate, and are in general harder to initiate experimentally [1]. Empirical data reveal that the minimal propagation field required for positive streamers is 4 – 6 kV/cm, whereas the minimal field needed for negative streamer propagation is in the range 10 – 12 kV/cm [2, 11].

As the streamer propagates, it leaves behind a filamentary plasma channel with a typical radius of 20 – 100  $\mu\text{m}$  [43], and with an electron density usually in the range  $10^{13}$  –  $10^{15}$  electrons/cm<sup>3</sup> for short gaps [32]. For longer gaps (40 mm), the channel radius is measured to be in the range 0.1 – 2 mm, depending on the applied voltage and electrode geometries [44]. The excess of positive ions is mainly found as a very thin positive space layer on the channel boundary, slowly expanding outwards due to electrostatic forces [32].

Typical propagation speeds recorded for streamer propagation in air at ground pressure are of the order 0.1 – 10 mm/ns [1]. This is faster than the velocity of electron avalanches, explaining why breakdowns for larger values of the product  $pd$  are recorded to occur much faster than predicted by Townsend's theory [19]. Experimental data recorded for a 40 mm needle-plane

gap configuration at STP in ambient air suggests that there exist a close relation between the streamer diameter  $d$  and the streamer velocity  $v$ , which may be modeled by the fit function [44]

$$v = 0.5d^2, \quad (2.27)$$

where  $d$  is measured in millimetres and  $v$  is given in mm/ns. This empirical relation applies to both positive and negative streamers, but for streamers with a diameter of 0.2 mm, the above approximation has been found to yield too slow velocities, differing by a factor of 5 from empirical data [44].

In the streamer, most collisions between the rapidly moving electrons and the slower gas particles are inelastic, producing minimal kinetic energy exchange [11]. The temperature of the gas particles is thus close to ambient, whereas the electrons are associated with much higher temperatures. Therefore, no local thermal equilibrium among the different gas species exists, and the plasma is said to be non-thermal [2]. Because of the stochastic nature of the electron avalanches, streamers normally break up into numerous branches [23, 45, 46]. However, this thesis will not go into the subject of streamer branching.

#### 2.4.4 Photoionization and other sources of free electrons

As described above, positive streamers propagate through a mechanism involving growth of multiple electron avalanches directed towards the streamer head. This process requires a certain density of free electrons present around the streamer tip at any instant, in order for avalanches to be initiated.

For streamer discharges in air, photoionization is recognized as an important source of free electrons for positive streamers [22, 32, 46, 47]. The process is attributed to the fact that the ionization potential of molecular nitrogen (15.6 eV) is higher than that of oxygen (12.1 eV) [48]. As nitrogen has many excitation levels with energies exceeding the oxygen ionization energy, radiative de-excitation from such states may produce photons carrying enough energy to ionize  $O_2$  molecules. However, this can only occur within a narrow window of energies, corresponding to the photon wavelengths 98 – 102.5 nm. Photons of shorter wavelengths are heavily absorbed by  $N_2$  molecules, and thus cannot effectively cause photoionization, whereas longer wavelengths correspond to photon energies below the ionization threshold of oxygen. Within this range, photons are mainly produced by radiative de-excitation from the three electronically excited vibrational singlet states  $b^1\Pi_u$ ,  $b'^1\Sigma_u^+$  and  $c_4^1\Sigma_u^+$  to the ground state  $X^1\Sigma_g^+$  [48, 49]. These are all UV photons, and the respective names of the above transitions are Birge-Hopfield I, Birge-Hopfield II and Carroll-Yoshino Rydberg [49]. In air at STP, the absorption coefficient  $\kappa$  of such ionizing photons is approximately  $130 \text{ cm}^{-1}$ , low enough to constantly create free electrons in a not too small region around the streamer head [43]. For a full high-resolution experimental analysis of the  $N_2$  spectrum within the energy range corresponding to the photon wavelengths 80 – 135 nm, see for example the work done by Heays et al. [50].

Another source of free electrons is electron detachment from background ionization. Natural radioactivity constitute the main contribution to background ionization in air on Earth, and

additional background ionization is caused by cosmic rays when they penetrate the Earth atmosphere [1]. Normally, the background ionization level is in the range  $10^3 - 10^4$  electron - positive ion pairs per  $\text{cm}^3$  [51]. However, this value may be much higher for pulse-repetitive discharges, where ions may remain and accumulate in the air gap from earlier discharges. With a 1 Hz repetition rate and a gap of a few centimetres, the background ionization level can reach  $10^7 \text{ cm}^{-3}$  [51].

## 2.4.5 Influence of dielectric surfaces

### 2.4.5.1 Polarization effects

Dielectric materials are electric insulators characterized by their ability to get polarized when influenced by an electric field. The strength of the polarization is determined by the material-specific relative permittivity  $\epsilon_r$ . In the presence of an electric field, the polarization has the effect of reducing the field inside of the dielectric. Because the field inside of a dielectric is reduced, the field just outside of the material is increased. Depending on the field direction, either electrons or positive ions in discharges propagating near the dielectric surface therefore experience a noticeable attractive force if  $\epsilon_r$  is large [1].

### 2.4.5.2 Processes at dielectric surfaces

In general, all the mechanisms outlined in section 2.2 responsible for liberation of electrons at metal surfaces are also active at dielectric surfaces [19]. However, the internal energy band structure associated with a dielectric differs considerably from the band structure of metals. Whereas the Fermi level energy for metals corresponds to the energy of an actual electron quantum state, this is not the case for dielectrics. For such materials, the Fermi level is situated in the middle of the gap between the valence band (the highest energy level filled with electrons at zero temperature) and the conduction band (the lowest energy level not filled with electrons at zero temperature). Typically, this band gap presents a barrier of about 4 eV for polymeres [30]. At room temperature, very few electrons are excited to the conduction band, and the large majority of the electrons are situated in the valence band. Some electrons may also, due to surface contamination of foreign atoms, be placed in so-called impurity levels.

In contrast to metal surfaces, the surface of a dielectric gets electrically charged when emitting or accepting charges. This effect may potentially have a large influence on repetitive discharge experiments [30]. An important mechanism responsible for charging a dielectric surface during streamer discharges is electron bombardment. Upon impact, an electron may either cause a secondary electron to be released from the surface, charging it positive, or the electron attaches to the surface, charging it negative. Jorgenson et al. [30] found that the latter process dominates for typical electron energies that are encountered in the head of a streamer. Thus, this mechanism acts as a sink of free electrons.

### 2.4.5.3 Streamer propagation close to a dielectric surface

For streamers propagating close to a dielectric surface, a large region on one side of the streamer head, where photoionization would normally take place, is blocked by the material. This effect may especially influence the propagation of positive streamers in air, whose mechanism of propagation largely relies on photoionization. However, because of the different surface mechanisms, the surface itself can be an efficient source of free electrons. In fact, experiments have shown that streamers in some cases propagate faster along dielectric surfaces than in air alone [1, 52, 53, 54].

Akyus et al. [53] points out that the increased speed suggests increased ionization intensity in the streamer head. This they attribute to the different mechanisms liberating electrons from the dielectric surface, in addition to the enhancement in the electric field caused by the polarization of the dielectric. They also mention possible deposition of negative charges on the dielectric surface prior to the streamer propagation as a possible contributing factor.

Dubinova [1] proposes that the increased speed is mainly due to photoemission from the dielectric surface caused by photons of energies 2.27–4.63 eV produced in the transition  $N_2^*(C^3\Pi_u) \rightarrow N_2(B^2\Pi_g)$ . Such photons are hardly absorbed by the air molecules, and may serve as a nonlocal source of free electrons ahead of the streamer. However, she did not find evidence of this in her numerical simulations. It must be mentioned that the photon yield  $\gamma_{ph}$  is very low for most dielectrics within the proposed energy range. Using figure 2.5a, the yield for Nylon 6, Polyethylene and Polypropylene is found to be less than  $10^{-8}$ .

A more complete numerical model, including eleven radiative transitions, have been implemented and tested by Jorgenson et al. [30]. By means of Monte Carlo simulations, they found that photoemission from dielectrics did contribute to growth of electron avalanches. However, according to their findings, this mechanism was dominated by electron attachment to the surface, which acted as a sink of free electrons. This efficiently canceled out the growth in electron avalanches.

As experimental data on photon yield coefficients for different materials is scarce, a selection of work functions for different polymers with dielectric constants  $\epsilon_r$  is presented in table 2.5. Assuming that the band gap between the valence band and the conduction band is about the same for all the given polymers, it is reasonable to expect that the photon yields for two polymers of similar work functions are comparable. For example, examining figures 2.5b and 2.5c, the photon yield is roughly a factor of 10 higher for polyethylene than for teflon. Inspection of table 2.5 reveals that polyethylene has a lower work function than teflon, so the fact that polyethylene is associated with a higher photon electron yield is expected. Moreover, from the table it may be noticed that the work functions seem to decrease with increasing values of  $\epsilon_r$ . This observation is also supported theoretically. Based on a simple classical model utilizing image forces, it may be shown that [55]

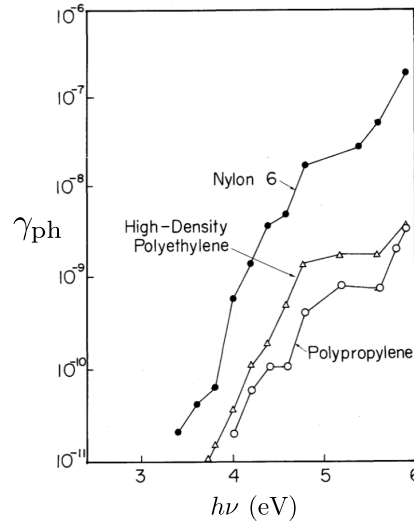
$$\phi \sim \frac{\epsilon_r + 7}{\epsilon_r + 1}. \quad (2.28)$$

This relation suggest that  $\phi$  is a monotonically decreasing function of  $\epsilon_r$ . If the relative dielectric permittivity of a material not included in the table is known, this empirical relation may be used

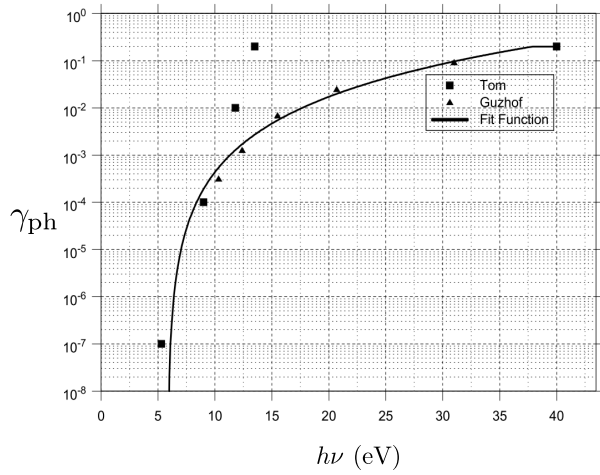
to estimate the work function and thereby also the photon yield of the material. However, it must be noted that such a procedure is highly uncertain.

Material	Work function $\phi$ (eV)	Dielectric constant $\epsilon_r$
Polytetrafluoroethylene (Teflon)	5.75	2.1
Polyvinyl chloride (PVC)	5.13	3-4
Polystyrene	4.90	2.6
Polyethylene	4.90	2.3
Polyvinyl acetate	4.38	5.5
Nylon 6	4.3	3.9-7.6
Polyethylene oxide	3.95	6.0

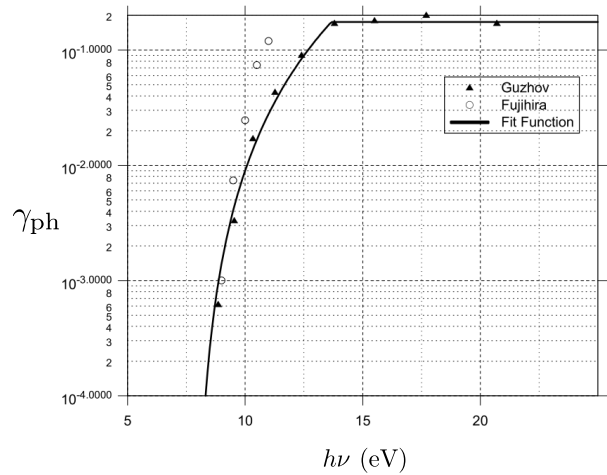
**Table 2.5:** Some work functions  $\phi$  for different dielectric materials of relative permittivity  $\epsilon_r$ . Note that  $\phi$  in general decreases with increasing values of  $\epsilon_r$ . The values presented here are taken from [55].



(a) Nylon 6, Polyethylene and Polypropylene.



(b) Teflon



(c) Polyethylene

**Figure 2.5:** Electron yield coefficients  $\gamma_{ph}$  describing photoemission from Nylon 6 (a), Polyethylene (a and c), Polypropylene (a) and Teflon (b). A function (full line) has been fitted to the experimental data. Note that the range of the axes are not equal. Figure (a) is taken from [56], and figures (b) and (c) are taken from [30]. References to the origin of the experimental data may be found therein.

# Chapter 3

## STREAMER MODEL

The streamer model used in this work is formulated within the fluid approximation for treatment of ions and electrons. The model is centered around a set of four distinct coupled and highly non-linear equations. These, together with appropriate boundary conditions, governs all the physics. As the number of neutral molecules in a gas at normal pressure and temperature is very large compared to the number of ionized molecules, the density of neutrals is assumed constant.

The temporal and spatial evolution of massive species are modeled using the minimal plasma model, meaning that only mass conservation is solved for. Furthermore, the electric field is calculated by first solving the Poisson equation for the electric potential, and photon transport is described through the radiative transfer equation in the Eddington approximation. Lastly, conservation of surface charges is imposed on dielectric boundaries through a scalar conservation equation.

### 3.1 The computational domain

All the equations are solved on a rectangular Cartesian computational grid. Inside the computational domain, conductor or dielectric surfaces may be present in form of embedded boundaries. At all boundaries (both domain boundaries and embedded boundaries), different boundary conditions apply to the different equations. These are discussed along with the presentation of each of the model equations in the following sections.

#### 3.1.1 Representation of embedded boundaries

Preferably, all embedded boundaries should be described using so-called cut-cell representation, which provides accurate geometrical description of dielectric and conductor surfaces. In a mathematical sense, boundaries represent the outer edges of the computational domain. Beyond these edges, no solution to the differential equations should exist. With respect to the hydrodynamic

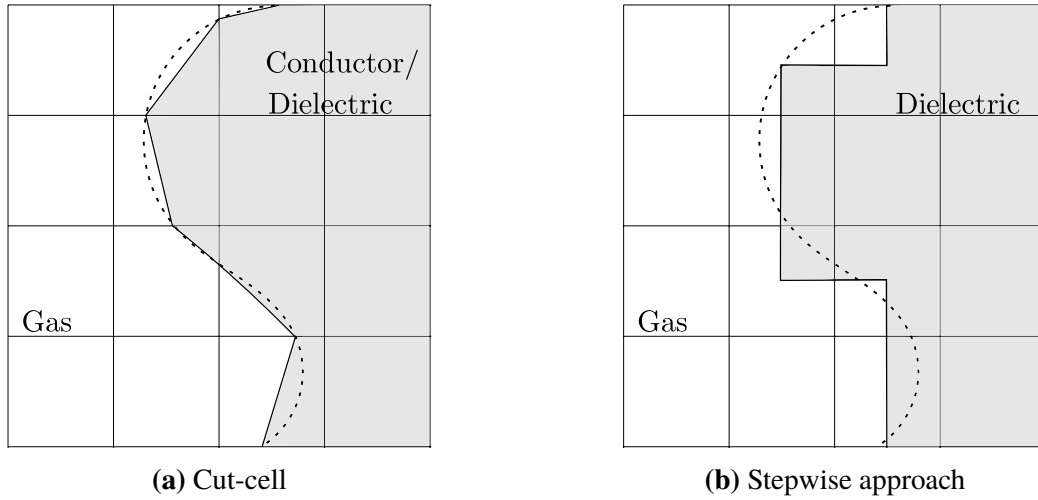


**Figure 3.1:** 2D illustration of embedded boundaries using (a) a cut-cell representation and (b) a stepwise approach. (a): A higher order implicit function describing the boundary (dashed line) is piecewise linearized (full line) inside each of the cells intersected by the function. Every boundary cell is then effectively cut by a straight line segment into two regions; one region is inside the conductor, and one is not. (b): A higher order implicit function describing the boundary (dashed line) is approximated by straight line segments (black line) running stepwise through the cell centers.

equation and the radial transfer equation, both dielectric and conductor boundaries fulfill this definition, as ions, electrons and photons are modeled only within the gas phase. All embedded boundaries conforming to this mathematical definition are described using cut-cell representation. An example of the cut-cell technique is given in figure 3.1a. The dashed line illustrates a higher order implicit function describing the boundary. This function is piecewise linearized (full line) inside each of the cells intersected, creating “cut-cells”, whose interiors are cut by a straight line segment (a plane in 3D). It must be noted that such cells add computational complexity and overhead to the equations, because their treatment requires introduction of special numerical stencils.

Concerning the Poisson equation, only conductor borders conform to the mathematical boundary definition given above. This is because the domain of Poisson’s equation also extends to the inside of dielectric materials. Consequently, dielectric borders must in this context be regarded as *interfaces* rather than mathematical boundaries. Due to reasons discussed in section 3.3, such interfaces are not straightforwardly compatible with cut-cell representation. Instead, when solving the Poisson equation, dielectric surfaces are represented as straight line segments (planes in 3D) running stepwise through the cell centers, as illustrated in figure 3.1b. As seen, this is a simpler approach compared to cut-cell representation. However, the advantage of using such a representation is that no special treatment is required for the interface cells when solving Poisson’s equation.



## 3.2 Hydrodynamic equations

Within a hydrodynamic treatment, motion of ions and electrons are described through changes in their corresponding macroscopic volumetric densities  $n_\alpha$  (the subscript  $\alpha$  denotes a generic charge carrier species). With no external forces, the dynamics is governed by concentration gradients, which gives rise to diffusive volumetric mass fluxes of magnitude  $D_\alpha \nabla n_\alpha$ . Here,  $D_\alpha$  is the diffusivity measured in  $\text{m}^2/\text{s}$ . This process continues until the masses of the charged species are distributed uniformly. However, in the presence of externally applied electric fields, the charged species will start to drift along the direction of the electric field with a drift velocity  $\mathbf{u}_\alpha$ , due to electric forces. This velocity may be expressed as

$$\mathbf{u}_\alpha = \pm \mu_\alpha \mathbf{E}, \quad (3.1)$$

where the negative sign applies to advection of negatively charged particles, as they drift in the opposite direction of the electric field. Moreover,  $\mu_\alpha$  is the electric mobility defined by equation (2.1) and  $\mathbf{E}$  is the magnitude of the electric field. This creates a mass flux of magnitude  $\mathbf{u}_\alpha n_\alpha$  along the direction of the field. In addition, because of various ionization and deionization mechanisms described earlier on, the number of electrons and ions at any point in a continuous domain may increase or decrease.

The total rate of change in the density of each species per time unit is determined by the mechanisms described above. Mathematically, this translates into a set of drift-diffusion-reaction equations given by

$$\frac{\partial n_\alpha}{\partial t} + \nabla \cdot (\pm \mu_\alpha \mathbf{E} n_\alpha - D_\alpha \nabla n_\alpha) = R_\alpha. \quad (3.2)$$

Here,  $\nabla \cdot (\dots)$  is the total divergence from a differential volume element due to advective and diffusive fluxes, and  $R_\alpha$  is a source term describing changes in the number density of the species  $\alpha$  caused by the various ionization and deionization processes.

Although the above discussion followed an heuristic approach, it is possible to rigorously derive equation (3.2) from the Boltzmann kinetic equation. The Boltzmann equation is formulated in terms of a velocity distribution function, containing detailed microscopic information within a six-dimensional phase space. In fact, the microscopic information may be used to deduce all macroscopic quantities like density, velocity, temperature, stresses and heat flux. This is done by taking velocity moments of the Boltzmann equation. The  $k$ 'th moment is found by multiplication of the velocity  $\mathbf{v}$  raised to the power of  $k$ , followed by integration over velocity space. The zeroth moment of the Boltzmann equation is then simply given by integration over velocity space, and yields the continuity equation for the particle number density. The first moment gives the equation for momentum conservation, and the second moment yields the equation for conservation of energy. However, all these equations are coupled and constitute an infinite chain of dependencies. In order to close the set of equations, so-called constitutive relations need to be inferred, which may either be obtained from experiments or from physical reasoning (approximations). Dujko et al. [57] solely rely on the latter approach in their derivation of (3.2) from the

continuity equation and momentum conservation equation. However, such approximations, allowing truncation of the chain of moment equations, lead to restrictions of the conditions under which the hydrodynamic equations are valid. More specifically, these equations are only valid when the local Knudsen number, defined as

$$\text{Kn}_\ell = \lambda_\alpha \frac{|\nabla n_\alpha|}{n_\alpha}, \quad (3.3)$$

have a value  $\text{Kn}_\ell > 0.05$  [58]. Here,  $\lambda_\alpha$  is the molecular mean free path associated with species  $\alpha$ . For a more detailed treatment of the topic discussed here, see for example the book by Cercignani [59].

### 3.2.1 Implementation

In the work presented here, equation (3.2) have been implemented for electrons and two generic types of ionic species; positive ions and negative ions. Denoting quantities relating to electrons, positive ions and negative ions by subscripts  $e, p$  and  $n$  respectively, the following set of hydrodynamic equation is used:

$$\frac{\partial n_e}{\partial t} + \nabla \cdot (-\mu_e \mathbf{E} n_e - D_e \nabla n_e) = R_e, \quad (3.4a)$$

$$\frac{\partial n_p}{\partial t} + \nabla \cdot (\mu_p \mathbf{E} n_p) = R_p, \quad (3.4b)$$

$$\frac{\partial n_n}{\partial t} + \nabla \cdot (-\mu_n \mathbf{E} n_n) = R_n. \quad (3.4c)$$

As seen in equations (3.4b) and (3.4c), the diffusion term for the ionic species is neglected. This is a valid and much used approximation, because the diffusivity of ions is normally as low as  $\sim 5 \times 10^{-6} \text{ m}^2/\text{s}$  [60]. Resultantly, movement due to ion diffusion is hardly measurable over the course of typical streamer inception and propagation time frames in short gap simulations, which are of the order of nanoseconds. Another common approximation, as for example used in [1, 51, 61, 62], is to additionally neglect ion advection. Although justified (over the course of 20 ns, advection typically cause ion movement of approximately 0.1 mm [1]), neglect of this term removes important physics relating to the boundary conditions of the model. As described earlier on, bombardment of ions at electrode and dielectric surfaces is an important advection-driven mechanism for creating free electrons. This effect may be added artificially through approximate boundary conditions, but such an approach decreases the model accuracy. Therefore, the model used in this work includes advection of ions.

Of course, only including two generic species for positive and negative ions is a simplified approximation. In reality, air contains a large number of different ions, such as  $\text{N}_2^+$ ,  $\text{O}_2^+$ ,  $\text{N}_4^+$ ,  $\text{O}_4^+$ ,  $\text{O}_2^+\text{N}_2$  and  $\text{O}_2^-$ , to name a few. Although some models do take this variety into account (see for example [63]), the majority of fluid models available in the literature include only two generic ionic species. This is a well tested model and it has proven to incorporate the major features defining

streamer inception and propagation [12].

### 3.2.1.1 Computation of the model source terms

Regarding the source terms  $R_e$ ,  $R_p$  and  $R_n$  in equations (3.4), seven distinct processes are incorporated into the model. These are ionization by electron impact, electron attachment and detachment, electron-ion recombination, ion-ion recombination, background ionization and photoionization. The source terms are computed as follows:

$$R_e = \alpha n_e u_e - \eta n_e u_e - \beta_{ep} n_e n_p + k_{det} n_n N + R_0 + R_{ph}, \quad (3.5a)$$

$$R_p = \alpha n_e u_e - \beta_{ep} n_e n_p - \beta_{pn} n_e n_p + R_0 + R_{ph}, \quad (3.5b)$$

$$R_n = \eta n_e u_e - \beta_{pn} n_p n_n - k_{det} n_n N. \quad (3.5c)$$

Here,  $n_e$ ,  $n_p$  and  $n_n$  are the volumetric densities given by equations (3.4) and  $N$  is the constant volumetric density of neutral molecules. Furthermore,  $\alpha$  is the electron ionization rate coefficient,  $\eta$  is the electron attachment rate coefficient,  $\beta_{ep}$  is the electron-ion recombination rate coefficient,  $\beta_{pn}$  is the ion-ion recombination rate coefficient and  $k_{det}$  is the rate coefficient of detachment. Moreover,  $u_e = |\mathbf{u}_e|$  is the absolute value of the electron drift velocity given by equation (3.1),  $R_0$  is the background ionization rate, and finally  $R_{ph}$  is the photoionization source term. In general,  $R_{ph}$  is very hard to compute (see section 3.2.1.3). However, as described earlier on, photoionization is an important process and should be included.

### 3.2.1.2 Transport coefficients and rate coefficients

The hydrodynamic equations (3.4), together with the source term expressions (3.5), takes a range of different transport and rate coefficients (jointly termed swarm parameters) as input parameters. These need to be calculated before solving the set of equations. In general, the swarm parameters are functions of the electron and ionic energies, the gas pressure and the gas composition. Since no energy equations are solved, the actual electron and ionic energies remain unknown. However, equilibrium between the electron distribution function in response to changes in the local electric field is achieved within 10 ps for typical electric field magnitudes associated with streamers at ground pressure [49]. At equilibrium, electron energy gain from the electric field is balanced locally by collisional energy losses [64]. Since streamer development is typically measured in nanoseconds, a valid and much used approximation is the local field approximation, in which all swarm parameters are assumed to only depend locally on the reduced electric field  $E/N$  for a given temperature. Here,  $N$  is the gas number density (in the previous chapter, the pressure  $p$  was used instead of  $N$ , but from the ideal gas law it follows that  $N \sim p$ , so both  $E/N$  and  $E/p$  express the same dependency). In order to further ease calculations, synthetic air with the mixture 80%  $N_2$  and 20%  $O_2$  is considered (the real composition of dry unpolluted air is roughly 78.1%  $N_2$ , 20.9%  $O_2$ , 0.9% Ar and 0.1% other compounds, including  $CO_2$ , Ne, He and  $CH_4$ , to name a few) [65].

The different swarm parameters were obtained from two sources; some were taken from the literature, and others were calculated using the freely available BOLSIG+ software package for solving the Boltzmann equation for the electron distribution function [66]. All the coefficients used here, including references to their respective origins, are summarized in table 3.1. The BOLSIG+ software solves the Boltzmann equation in uniform electric fields using the two-term approximation. That is, the electron distribution function is approximated by the two first terms of its spherical harmonics expansion. The output rate coefficients are given as functions of the reduced electric field  $E/N$  for a range of different field magnitudes. Rate coefficient magnitudes in between these fixed output values are found by linear interpolation. As input parameters, scattering cross section data describing interactions between the gas species must be provided. In this work, all BOLSIG+ simulations are run using a complete set of scattering cross sections for  $N_2$  [67, 68] and  $O_2$  [69, 70] respectively.

The rate coefficients taken from the literature are assumed not to change too much for the electric field magnitudes typically associated with streamer discharges and are therefore deemed constants. Besides, these coefficients are several orders of magnitude smaller than the coefficients obtained from the BOLSIG+ simulations, i.e  $\mu_e \gg \mu_p, \mu_n$  and  $\alpha, \eta \gg \beta_{ep}, k_{en} \gg k_{det}$ . Consequently, small variations in these rates do not largely affect small gap streamer simulations. However, recombination and attachment mechanisms are known to be of considerable impact for the dynamics of long gap streamers in low electric fields [49]. Other coefficient magnitudes than presented in table 3.1 may be found elsewhere [12, 49, 51, 71].

Parameter	Magnitude	Unit	Description	Reference
$\mu_e$	$f(E/N)$	$m^2/Vs$	Electron mobility	BOLSIG+
$\mu_p$	$2.00 \times 10^{-4}$	$m^2/Vs$	Positive ion mobility	[2]
$\mu_n$	$2.02 \times 10^{-4}$	$m^2/Vs$	Negative ion mobility	[2]
$D_e$	$f(E/N)$	$m^2/s$	Electron diffusion coefficient	BOLSIG+
$\alpha$	$f(E/N)$	$1/m$	Townsend's ionization coefficient	BOLSIG+
$\eta$	$f(E/N)$	$1/m$	Townsend's attachment coefficient	BOLSIG+
$\beta_{ep}$	$5.00 \times 10^{-14}$	$m^3/s$	Electron-ion recombination rate coef.	[2]*
$\beta_{pn}$	$2.07 \times 10^{-12}$	$m^3/s$	Ion-ion recombination rate coefficient	[2]
$k_{det}$	$1.00 \times 10^{-18}$	$m^3/s$	Electron detachment rate coefficient	[2]
$R_0$	$1.00 \times 10^9$	$1/m^3s$	Background ionization rate coefficient	[2]
$R_{ph}$	$f(\Psi_{0,\gamma}(\mathbf{x}, t))$	$1/m^3s$	Photoionization rate coefficient	Equation (3.10)

\*This value is wrongly stated as  $5.00 \times 10^{-4}$  in Singh's thesis [2].

**Table 3.1:** Magnitudes of the swarm parameters used in the model equations (3.4) and (3.5), including data references.

### 3.2.1.3 Photoionization

Calculating the photoionization source term is difficult, as a general treatment requires knowledge of the isotropic part of the photon distribution function  $\Psi_{0,\nu}(\mathbf{x}, t)$  for all photon frequencies

$\nu$ . In this context, isotropic means that the direction  $\Omega$  of photon propagation is unimportant; the important factor is the total number of photons at a given point. Subsequently,  $\Psi_{0,\nu}(\mathbf{x}, t)$  is found by integrating the full photon distribution function  $\Psi_\nu(\mathbf{x}, \Omega, t)$ , which is given by the radial transfer equation (3.13) treated in section 3.4, over all spatial angles [43];

$$\Psi_{0,\nu}(\mathbf{x}, t) = \int_{\Omega} d\Omega \Psi_\nu(\mathbf{x}, \Omega, t). \quad (3.6)$$

A general expression for the photoionization source term  $R_{ph}$  may be given as [43]

$$R_{ph} = c \int_0^\infty d\nu \alpha_\nu^{ph} \Psi_{0,\nu}(\mathbf{x}, t), \quad (3.7)$$

where  $c$  is the speed of light and  $\alpha_\nu^{ph}$  is the photon ionization coefficient describing the probability of ionization per unit length. Since photon ionization necessarily involves absorption of the ionizing photons, it is normal to express  $\alpha_\nu^{ph}$  through the relation [43]

$$\alpha_\nu^{ph} = \xi_\nu \kappa_\nu. \quad (3.8)$$

Here,  $\kappa_\nu$  is the photon absorption coefficient for frequency  $\nu$ , and  $\xi_\nu \in [0, 1]$  is the corresponding probability of ionization. Using equation (3.7) as it stands to calculate the photoionization source term is in reality not feasible, as it involves obtaining the isotropic part of the solution to the radial transfer equation for all possible frequencies  $\nu$ . Solving for this quantity on a computer is intrinsically difficult, as an exact direct solution under steady-state conditions involves a six-dimensional integral over the complete volume and over all solid angles for all points. Pursuing such an approach therefore requires introduction of simplifications and approximations. A widely used integral approach, based on consideration of only a small frequency range for calculation of  $R_{ph}$ , has been given by Zheleznyak et al. [72, 43]. However, this method still requires a quadrature over all of space for each point, and is therefore computationally expensive. Measures have been proposed to reduce the computational cost, and includes among others confining the occurrence of photoionization to a small region around the streamer head [62] and treatment of streamers as a set of uniformly emitting disks [73].

In this thesis, none of the above methods is used. Instead, the approach presented here relies on direct numerical solution of the radial transfer equation in the Eddington approximation in order to obtain  $\Psi_{0,\nu}(\mathbf{x}, t)$  (or rather  $\Psi_{0,\gamma}(\mathbf{x}, t)$ , where  $\gamma$  is approximated to be a very small monochromatic frequency range - see the next section). The Eddington approximation is a Helmholtz-type equation derived from the radial transfer equation under assumption that the photon distribution function is only weakly dependent on the photon propagation direction  $\Omega$ , i.e that there exist no preferred direction of propagation [43].

### 3.2.1.3.1. The multigroup approximation

In this work, the monochromatic multigroup approximation [13]

$$\Psi_\nu(\mathbf{x}, \boldsymbol{\Omega}, t) = \sum_{\gamma} \Psi_\nu(\mathbf{x}, \boldsymbol{\Omega}, t) \delta(\gamma) \quad (3.9)$$

is adopted for numerical computations. Here,  $\gamma$  is a generic variable denoting a sufficiently sharp-lined frequency band so that all frequencies within this band may be approximated to have the same value.  $\delta(\nu)$  is the Dirac delta function, reflecting the fact that the above approximation in effect discretizes the continuous variable  $\nu$  into a finite set of very narrow frequency bands  $\gamma$ .

In the monochromatic multigroup approximation (3.9), the integral over all frequencies in equation (3.7) reduces to an expression much more suitable for numerical computations, and the final equation for the source term  $R_{ph}$  is then

$$R_{ph} = \sum_{\gamma} c \xi_{\gamma} \kappa_{\gamma} \Psi_{0,\gamma}(\mathbf{x}, t). \quad (3.10)$$

The numerical code is implemented in a way that allows the user to easily add as many frequency bands as desired. Because photoionization in air is mainly maintained by photons emitted by molecular nitrogen within a narrow frequency range corresponding to the wavelengths 98 – 102.5 nm (see section 2.4.4 in the previous chapter), this frequency band has been implemented as a base case. Within this band, radiation from the three contributing singlet states mentioned earlier on have been included. Also included is the Dressler-Lutz transition from the excited state  $a''^1\Sigma_g^+$ , releasing photons of energy 12.27 eV [30]. However, this transition is not very significant.

Following [43], the ionization probability  $\xi_{\gamma}$  associated with the above included frequency band is set to one, giving an abnormally high ionization rate. However, although photons of higher frequencies than 98 eV is mainly absorbed by  $N_2$  molecules, a small fraction are in reality also absorbed by Oxygen, causing ionization. Due to quantum effects, there is an additional very small possibility that ionization might occur for photons carrying lower energies. There are also many other mechanisms not taken into account here that may release photons, such as for example bremsstrahlung radiation from accelerating electrons [48]. Therefore, if the above described frequency band is the only band included, a high value of  $\xi$  may be justified because it could account for these missing ionizing photons.

### 3.2.2 Boundary conditions

In the model presented here, free outflow conditions on the charged species are used on the domain boundaries. Such is chosen in order to prevent unphysical accumulation of charges at the domain walls. A free outflux condition (i.e out of the gas phase) is implemented as

$$F_{\alpha} = n_{\alpha} \mathbf{u}_{\alpha} \cdot \hat{\mathbf{n}}, \quad (3.11)$$

where  $F_{\alpha}$  is the outflux of the species  $\alpha$ . Moreover,  $n_{\alpha}$  is the volumetric density of the species and  $\mathbf{u}_{\alpha}$  is the corresponding drift velocity given by equation (3.1). Finally,  $\hat{\mathbf{n}}$  is a unit normal

vector pointing out of the gas phase. Of course, all of the quantities included in the above equation should be evaluated at the boundary of the gas phase.

At embedded dielectric or conductor surfaces the situation is different. As discussed in the previous chapter, several distinct physical mechanisms are active when electrons, ions and photons interact with such surfaces. The exact surface flux of charged particles is therefore determined by the specific mechanisms chosen to be included by the user. Typically, different boundary conditions applies to different setups and varies according to the intention of the simulations. The computer code is implemented such that new boundary conditions can be added through a small set of C++ abstractions (typically a handful of code lines). In this way, the user can compile his own boundary conditions into the code without affecting the source code. For implementation details on the mechanisms included in this work, see section 3.6.

### 3.3 Electrodynamic equations

The electric field  $\mathbf{E}$  is calculated as the negative gradient of the electric potential  $\Phi$ , given by Poisson's equation;

$$\nabla \cdot (\epsilon \nabla \Phi) = -q(n_p - n_e - n_n) + \sigma \quad (3.12a)$$

$$\mathbf{E} = -\nabla \Phi. \quad (3.12b)$$

Here,  $\epsilon = \epsilon_r \epsilon_0$  is the electric permittivity and  $q = 1.60 \times 10^{-19}$  C is the elementary charge. Moreover,  $\rho = q(n_p - n_e - n_n)$  is the net charge density distribution, whereas  $\sigma$  is the net distribution of dielectric surface charges obtained from equation (3.27).

In short gap streamer modeling, all magnetic effects can safely be neglected, as the electric currents associated with such discharges are very low. A rough estimate given in [74] suggests that the streamer channel width must be at least 0.4 m if the streamer current is to give rise to noticeable magnetic fields.

Solving Poisson's equation is regarded to be a bottleneck in streamer simulations [1]. The reason is that the Poisson equation is intrinsically non-local, meaning that every cell in the computational domain need to be solved for at each time step in order to obtain a solution. This is easily understood from a physical point of view, as the electric field at any point is a superposition of contributions from all domain charges. In contrast, the drift-diffusion equation (3.2) does not share this property, as advection or diffusion of a quantity between two time steps may only locally affect the neighbouring cells.

Another challenge associated with the Poisson equation is that the permittivity  $\epsilon$  is discontinuous at embedded dielectric interfaces. It is easily shown [75] that the component of the electric field normal to dielectric interfaces inherit the permittivity discontinuity, and when solving the Poisson equation, this discontinuity condition should in general be enforced. This is the reason

why solving the Poisson equation is not straightforward when using cut-cell representation of dielectric interfaces. The same condition does not apply for the field component parallel to such interfaces, as this remains continuous. An attempt has been made [76] to make the streamer code compatible with cut-cell representation of dielectric boundaries. However, it was found that the proposed method did not guarantee second order convergence of the solution  $\Phi$  in terms of the  $L^\infty$ -norm (the norm measuring maximal error). It was therefore concluded that a more involved treatment is necessary, such as the approach developed by Crockett et al. [18].

For the current implementation, the discontinuity condition on the electric field is not handled directly. Instead, by representing dielectric interfaces using the stepwise approach described in section 3.1.1, numerical computations of the electric field component normal to the interfaces are avoided altogether - see section 3.7.2.2 for details. Since the field component parallel to dielectric interfaces is continuous, the the discontinuity condition is never explicitly treated.

### 3.3.1 Boundary conditions

For the Poisson equation, appropriate boundary conditions are of Dirichlet or Neumann type. In the case of Dirichlet conditions, the solution  $\Phi$  is given at the boundary. This condition is typically used on conductor boundaries to control the voltage between the electrodes. In contrast, when using Neumann conditions, the flux of the solution  $\partial_n \Phi$  is specified at the boundary. Here, the operator  $\partial_n$  denotes the normal derivative with respect to a boundary unit normal vector  $\hat{n}$  pointing out of the gas phase. In order to restrict all of the voltage drop to occur inside of the computational domain, it is normal to use the condition  $\partial_n \Phi = 0$  on the domain walls running parallel to the gap.

## 3.4 Radiative transfer equation

As mentioned in section 3.2.1.3, the radiative transfer equation (RTE) is used to describe the spatiotemporal distribution of photons  $\Psi_\nu(\mathbf{x}, \boldsymbol{\Omega}, t)$  with a specific frequency  $\nu$  within the gas domain. As indicated, the distribution function depends in general on position  $\mathbf{x}$ , angular direction  $\boldsymbol{\Omega}$  and time  $t$ . In the following it is assumed that the only source of photons is radiative de-excitation processes from excited species  $u$ . Their corresponding volumetric densities are denoted as  $n_u$ . Moreover, it is assumed that photons move in straight lines with the same frequency until being absorbed by the gas. Collisional scattering and changes in photon frequencies due to various phenomena is therefore neglected. With these assumptions, the RTE may be stated as [43]

$$\frac{\partial \Psi_\nu(\mathbf{x}, \boldsymbol{\Omega}, t)}{\partial t} + c \boldsymbol{\Omega} \cdot \nabla \Psi_\nu(\mathbf{x}, \boldsymbol{\Omega}, t) + c \kappa_\nu \Psi_\nu(\mathbf{x}, \boldsymbol{\Omega}, t) = \sum_{u \rightarrow d} \frac{n_u(\mathbf{x}, t) \Phi_{u \rightarrow d}(\nu)}{4\pi \tau_{u \rightarrow d}}, \quad (3.13)$$

where  $\kappa_\nu$  is the photon absorption coefficient (also known as Beer's length) and  $c$  is the speed of light. The term on the right hand side of the equation is a source term describing spontaneous emission per unit solid angle  $4\pi$ . The summation is to be taken over all radiative transitions



from an excited state  $u$  to a lower state  $d$  contributing to emission of photons with frequency  $\nu$ . The function  $\Phi_{u \rightarrow d}(\nu)$  is a normalized emission line profile for each transition  $u \rightarrow d$ . Lastly, the factor  $1/\tau_{u \rightarrow d}$  is Einstein's coefficient for spontaneous emission, giving the probability per unit time for the de-excitation processes  $u \rightarrow d < u$  to occur. Unless stated otherwise, all of the following discussion is based on [43].

A valid simplification of (3.13) is to neglect the transient term, because photon propagation is nearly instantaneous within the time scale of streamer propagation in centimetre-sized gaps (typically some tens of nanoseconds), yielding

$$\boldsymbol{\Omega} \cdot \nabla \Psi_\nu(\mathbf{x}, \boldsymbol{\Omega}, t) + \kappa_\nu \Psi_\nu(\mathbf{x}, \boldsymbol{\Omega}, t) = \sum_{u \rightarrow d} \frac{n_u(\mathbf{x}, t) \Phi_{u \rightarrow d}(\nu)}{4\pi c \tau_{u \rightarrow d}}. \quad (3.14)$$

As already discussed in section 3.2.1.3, the solution to the above equation may be found by direct integration. The solution  $\Psi_\nu(\mathbf{x}, \boldsymbol{\Omega}, t)$  can then be used with equations (3.6) and (3.7) to find the photoionization source term  $R_{ph}$ . However, as previously explained, this procedure is prohibitively expensive in terms of computational power and memory. Therefore, an alternative approach where equation (3.14) is solved in the Eddington approximation is used in this thesis. The details are presented in the following.

### 3.4.1 The Eddington approximation

Using the monochromatic multigroup approximation (3.9), the RTE equation (3.14) reduces to a finite set of equations, one for each frequency band  $\gamma$ ;

$$\boldsymbol{\Omega} \cdot \nabla \Psi_\gamma(\mathbf{x}, \boldsymbol{\Omega}, t) + \kappa_\gamma \Psi_\gamma(\mathbf{x}, \boldsymbol{\Omega}, t) = \sum_{(u \rightarrow d)_\gamma} \frac{n_u(\mathbf{x}, t)}{4\pi c \tau_{u \rightarrow d}}. \quad (3.15)$$

Here, the summation on the right hand side of the above equation should include all radiative transitions contributing to photon emission within the frequency range  $\gamma$ . Also, the emission line function  $\Phi_{u \rightarrow d}(\nu)$  is dropped, under the assumption that no radiation from any of the included excited states  $u$  is released outside of  $\gamma$ . The photon distribution function may in general be expanded in the spherical harmonics, yielding

$$\Psi_\nu(\mathbf{x}, \boldsymbol{\Omega}, t) = \frac{1}{4\pi} \Psi_{0,\nu}(\mathbf{x}, t) + \frac{3}{4\pi} \boldsymbol{\Omega} \cdot \boldsymbol{\Psi}_{1,\nu}(\mathbf{x}, t) \quad (3.16)$$

if only the first two terms are kept. Here,  $\Psi_{0,\nu}(\mathbf{x}, t)$  is the isotropic part of the distribution function given by equation (3.6), and

$$\boldsymbol{\Psi}_{1,\nu}(\mathbf{x}, t) = \int_{\Omega} d\Omega \boldsymbol{\Omega} \Psi(\mathbf{x}, \boldsymbol{\Omega}, t) \quad (3.17)$$

is a vector quantity representing a first order anisotropy correction to the dominating isotropic

term  $\Psi_0(\mathbf{x}, t)$ .

Plugging (3.16) into the monochromatic multigroup RTE (3.15) and taking the zeroth and first angular moments of the resulting equation (analogues to the velocity moments of the Boltzmann equation discussed in section 3.2, but with multiplication of  $\Omega^k$  before integrating instead of  $\mathbf{v}^k$ ) yields the respective equations

$$\nabla \Psi_{1,\gamma}(\mathbf{x}, t) + \kappa_\gamma \Psi_{0,\gamma}(\mathbf{x}, t) = \sum_{(u \rightarrow d)_\gamma} \frac{n_u(\mathbf{x}, t)}{c\tau_{u \rightarrow d}} \quad (3.18)$$

and

$$\frac{1}{3} \nabla \Psi_{0,\gamma}(\mathbf{x}, t) + \kappa_\gamma \Psi_{1,\gamma}(\mathbf{x}, t) = 0. \quad (3.19)$$

If combined, these equations may be used to eliminate the flux term  $\Psi_{1,\gamma}(\mathbf{x}, t)$ , giving an equation which only depend on the isotropic part of the distribution function  $\Psi_{0,\gamma}(\mathbf{x}, t)$ . The emerging equation is then said to be the Eddington approximation (or more systematically the SP<sub>1</sub> approximation) of (3.15), and is given by

$$-\nabla \cdot \left( \frac{1}{3\kappa_\gamma} \nabla \Psi_{0,\gamma}(\mathbf{x}, t) \right) + \kappa_\gamma \Psi_{0,\gamma}(\mathbf{x}, t) = \sum_{(u \rightarrow d)_\gamma} \frac{n_u(\mathbf{x}, t)}{c\tau_{u \rightarrow d}}. \quad (3.20)$$

### 3.4.2 Computation of the RTE source term

The source term on the right hand side of (3.20) may be calculated directly if the number density  $n_{u,\gamma}$  and the corresponding spontaneous emission coefficient  $1/\tau_{u \rightarrow d,\gamma}$  for each excited state contributing to emission within the frequency band  $\gamma$  are known. In general, the hydrodynamic equation governing the motion of a neutral in the excited state  $u$  is given by

$$\frac{\partial n_u}{\partial t} - \nabla \cdot (D_u \nabla n_u) = k_{ex} n_e - \sum_{d < u} \frac{n_u}{\tau_{u \rightarrow d}} + \sum_{h > u} \frac{n_h}{\tau_{h \rightarrow u}} - S_u^- + S_u^+. \quad (3.21)$$

All the terms on the right hand side of the above equation are source terms due to various gain and loss mechanisms. The first source term describes excitation by electron impact expressed as the product between the specific electron excitation rate coefficient  $k_{ex}$  and the electron density  $n_e$ . The second term is a loss term and describes de-excitation of the excited state  $u$ . The factor  $1/\tau_{u \rightarrow d}$  is Einstein's coefficient for spontaneous emission as before. The third term expresses de-excitation of a higher state  $h > u$  to state  $u$ , and the fourth term includes quenching of the excited state  $u$ , i.e non-radiative transitions to lower states due to for example collisions. Finally, the last term is quenching of a higher state  $h$  to state  $u$ .

As seen by equation (3.21), a general treatment of an excited species  $u$  requires knowing the densities  $n_h$  and  $n_d$  of species of both higher and lower energies. Each of these densities must

be solved for by an equation identical to (3.21). In reality, a range of simplifications and approximations removing the coupling terms may be justified.

Here, the model provided by Zhelezniak et al. [72] is used, in which the diffusive term and both the source terms involving transitions from higher states  $h$  to the state  $u$  are neglected. The remaining three mechanisms, describing electron impact ionization, spontaneous radiative emission and quenching of the excited state  $u$  are further assumed to be in equilibrium, and the transient term therefore disappears. Moreover, the respective probabilities associated with all radiative and non-radiative transitions are absorbed into an overall probability factor  $1/\tau$ , where  $\tau$  is the average lifetime of the excited state [1]. Finally, the quantity  $\tau/\tau_{u \rightarrow d}$  can be written as  $p_q/(p + p_q)$ , yielding the equation

$$\frac{n_u}{\tau_{u \rightarrow d}} = \frac{p_q}{p + p_q} k_{ex} n_e. \quad (3.22)$$

Here,  $p_q$  is a so-called quenching pressure representing the effect of both radiative and collisional quenching and  $p$  is the gas pressure. For atmospheric air, the quenching pressure is  $p_q = 30$  Torr [48] and the coefficient  $k_{ex}$  is obtained from BOLSIG+ simulations. Using equation (3.22), the source term on the right hand side of the Eddington approximation (3.20) may now be restated as

$$\sum_{(u \rightarrow d)_\gamma} \frac{n_u(\mathbf{x}, t)}{c\tau_{u \rightarrow d}} = \frac{p_q}{c(p + p_q)} n_e \sum_{u_\gamma} k_{ex}, \quad (3.23)$$

where the last summation should be taken over all excitation rate constants  $k_{ex}$  associated with radiative states  $u$  releasing photons within the frequency band  $\gamma$ .

### 3.4.3 Boundary conditions

A suitable boundary conditions for the RTE in the Eddington approximation (3.20) is given by [13]

$$\frac{\partial \Psi_{0,\gamma}(\mathbf{x}, t)}{\partial n} + \frac{3\kappa_\gamma}{2} \frac{1 + 3r_1}{1 - 2r_2} \Psi_{0,\gamma}(\mathbf{x}, t) = \frac{g}{\kappa_\gamma}, \quad (3.24)$$

where the operator  $\frac{\partial}{\partial n} = \hat{\mathbf{n}} \cdot \nabla$  denotes the normal derivative at the boundary with respect to a unit normal vector  $\hat{\mathbf{n}}$  pointing out of the gas phase. The boundary condition (3.24) is of Robin type and includes two reflection coefficients,  $r_1$  and  $r_2$ , in addition to a general surface source term  $g$ . However, in this work, neither photon reflection nor photon injection at the boundaries is considered, so  $r_1 = r_2 = g = 0$ . In other words, free outflow of photons is practiced and the above equation collapses to

$$\frac{\partial \Psi_{0,\gamma}(\mathbf{x}, t)}{\partial n} = -\frac{3\kappa_\gamma}{2} \Psi_{0,\gamma}(\mathbf{x}, t). \quad (3.25)$$

From this relation it is possible to deduce an expression for the radiative photon flux out of the gas phase, defined as  $\mathbf{F}_\gamma(\mathbf{x}, t) = c\Psi_{1,\gamma}(\mathbf{x}, t)$ , where  $c$  is the speed of light. Making use of equation (3.19), this expression is given as

$$\hat{\mathbf{n}} \cdot \mathbf{F}_\gamma(\mathbf{x}, t) = \frac{c}{2}\Psi_{0,\gamma}(\mathbf{x}, t). \quad (3.26)$$

### 3.5 Scalar conservation equation at dielectric surfaces

At dielectric surfaces, a scalar equation of the form

$$\frac{\partial \sigma}{\partial t} = F \quad (3.27)$$

is solved in order to enforce charge conservation. As pointed out in the previous chapter, electrical charging of dielectrics is an important physical phenomenon. Here,  $\sigma$  is the net surface charge distribution on all dielectric surfaces, and  $F$  is the net dielectric charge flux. This flux is determined by the dielectric boundary conditions discussed in section 3.6.2.

### 3.6 Implementation of surface mechanisms

As described in the previous chapter, a range of different mechanisms can cause liberation of electrons from both conductor and dielectric surfaces. Such mechanisms should not be implemented blithely solely based on physical considerations. Also numerical considerations should be taken into account.

In the simulations considered here, the electric fields reaches maximum values of the order of 0.1 MV/cm. In such fields, the Schottky effect and field emission may be neglected, as these mechanisms require 10 – 100 times larger field magnitudes in order to become significant. As explained in the theory chapter, kinetic ejection by ion bombardment can also safely be neglected for the field magnitudes appearing in the simulations. Moreover, the simulations are designed in such a way that the electric field always points towards or along dielectric surfaces. Therefore, electron and negative ion bombardment at dielectric surfaces can be disregarded. However, this leads to an enhanced flux of positive ions at such surfaces, causing liberation of electrons through the Auger neutralization process (see section 2.2.2 in the theory chapter). This surface mechanism is indeed assumed to be significant for two reasons. Firstly, propagation of a positive streamer close to a dielectric surface necessarily also leads to an abundance of positive ions close to the surface. Secondly, the estimation (2.5) of the ion bombardment yield coefficient reveals that this mechanism is associated with a high electron yield coefficient. Based on these two criteria, photoemission is also identified as a significant mechanism necessary to include. A final mechanism which may potentially cause liberation of a sizable number of secondary electrons is bombardment of metastable atoms. At least, this mechanism is associated with a high estimated yield coefficient (again, see section 2.2.2 in the previous chapter). However,

estimating the number of metastable atoms present at the material surfaces is difficult. Therefore, this mechanism is not directly included in the implementation, but instead it is attempted to be compensated for by choosing a somewhat larger value of  $\gamma_{\text{ion}}$  than suggested by the estimate (2.5).

In fact, the action of accounting for lower impact mechanisms by using higher electron yield coefficients when implementing other more dominant mechanism is more than a convenient excuse for not dealing directly with such processes. Implementation of a large number of possible surface mechanism would give an impractical number of tunable electron yield parameters. Besides, the emission uncertainties associated with the most prominent mechanisms are in general much larger than the total emission due to low impact mechanisms.

### 3.6.1 Metal surfaces

All metal electrodes are assumed to be part of an external current, providing stable voltages to the anodes and cathodes. Therefore, full neutralization is expected to occur when a charged species is incident on anode and cathode surfaces. Consequently, free outflux (i.e. out of the gas phase) of charged species is implemented on all metal surfaces according to equation (3.11).

From a numerical point of view, the anode and the cathode should be treated differently when implementing inflow (i.e into the gas phase) of electrons caused by the various surface mechanisms. At the anode, the electric field points away from the surface, whereas at the cathode, the field points towards the surface. Electrons liberated from the anode surface will therefore, due to electric forces, be accelerated back towards the metal as soon as they are released.

#### 3.6.1.1 Anodes

Using the formulas (2.2) and (2.3a) from the previous chapter, the maximum kinetic energies of the released electrons due to respectively photoemission and Auger neutralization can be calculated. Using the ionization threshold of nitrogen (15.6 eV) and assuming that the incident photons have a wavelength of 98 nm, the kinetic energies are

$$E_k^{\text{ph}} \approx 8.2 \text{ eV}, \quad (3.28a)$$

$$E_k^{\text{n}} \approx 6.6 \text{ eV}. \quad (3.28b)$$

In the calculation of the above values, a typical metal work function of 4.5 eV was used (see table 2.4). As noted earlier on, the magnitude  $E$  of the electric field at the anode is of the order of 0.1 MV/cm in the simulations considered in this work. Using this value, the acceleration  $a$  of an electron in a uniform electric field can be calculated as [75]

$$a = \frac{qE}{m_e} \approx 1.8 \times 10^{18} \text{ m/s}^2. \quad (3.29)$$

Here,  $q$  is the elementary charge and  $m_e = 9.1 \times 10^{-31} \text{ kg}$  is the electron mass. With the

energies given in equations (3.28a) and (3.28b), the released electrons only propagate about  $0.1 \mu\text{m}$  into the gas before they are sucked back up to the anode again due to the massive deceleration quantified by the above relation.

Therefore, implementing an influx (i.e. into the gas phase) of electrons at the anode due to these surface mechanisms would be wrong for two reasons. Firstly, resolving the propagation would require the mesh cells to be smaller than  $0.1 \mu\text{m}$ , which would be impractical, inefficient and unnecessary for most simulations. Secondly and most importantly, the electron energies given in equations (3.28) are not sufficient to cause ionization. However, the way the source terms are implemented in equation (3.5), all electrons within the gas are in reality assumed to be ionizing (but the ionizing efficiency is controlled by the local electric field). Therefore, these electrons would give an unphysical contribution to ionization of the gas. Thus, due to numerical considerations, no influx of electrons should be implemented at the anode.

### 3.6.1.2 Cathodes

At the cathode, the situation is different. Here, the electrons are accelerated into the gas when released from the surface and no numerical restraints for inflow of electrons exist. Therefore, both ion bombardment and photoemission are included on cathode surfaces. These mechanisms are implemented as

$$F_{\text{ion}} = \gamma_{\text{ion}} F_{\text{p}}, \quad (3.30a)$$

$$F_{\text{ph}} = \gamma_{\text{ph}} F_{\text{ph}}, \quad (3.30b)$$

where  $F_{\text{ion}}$  is the electron influx caused by ion bombardment and  $F_{\text{ph}}$  is the influx of electrons due to photoemission. Furthermore,  $\gamma_{\text{ion}}$  and  $\gamma_{\text{ph}}$  are the electron yield coefficients defined in sections (2.2.2) and (2.2.1) in the previous chapter. Finally,  $F_{\text{p}}$  is the free volumetric flux density of positive ions at the surface given by equation (3.11) and  $F_{\text{ph}}$  is the photon surface flux obtained from equation (3.26).

#### 3.6.1.2.1. Electron yield coefficients

Deciding upon the specific values to be used for the electron yield coefficients is a difficult task. Firstly, as described in the theory chapter, the efficiencies of the surface mechanisms are in reality sensitive to the condition of the actual electrodes used in experiments (contamination, roughness, etc.). Secondly, experimental data on the yield coefficients is scarce for most materials. Thirdly, even with accurate data at hand, the simulations are not likely to produce the correct number of secondary electrons if compared to experiments. This is because any numerical model is based on simplifications and approximations and therefore cannot possibly encompass the richness of processes and interactions occurring in nature. For example, studying figure 2.2 it is evident that photoemission from metal surfaces occur for a wide range of photon wavelengths; not only for the narrow  $98 - 102.5 \text{ nm}$  band implemented in this model. To account for this, a somewhat

higher photon yield should therefore be used. However, such an approach does not account for the fact that low-frequency photons are associated with longer photon absorption lengths than high-frequency photons. In the end, all numerical streamer models should be tuned to fit experiments. And as the premise of various numerical models in general differ, the yield coefficients used in some models are not universally applicable to other models. For example, in [77] a value  $\gamma_{\text{ion}} = 0.15$  is used, whereas a value  $\gamma_{\text{ion}} = 0.1$  is used in [78]. In the latter work they additionally assume all other secondary electron yields to be absorbed into this coefficient. Moreover, in [79] the yields  $\gamma_{\text{ion}} = \gamma_{\text{ph}} = 0.005$  are used.

From the estimate (2.5) and by inspection of figure 2.2 in the energy range 12.1 – 12.7 eV, corresponding to the implemented 98 – 102.5 nm band, the values  $\gamma_{\text{ion}} = 0.1$  and  $\gamma_{\text{ph}} = 0.2$  are obtained. However, as explained earlier on, a somewhat higher value of  $\gamma_{\text{ion}}$  should be used to account for bombardment of metastable atoms. Assuming that this mechanism is capable of releasing half as many electrons as ion bombardment, the magnitude  $\gamma_{\text{ion}} = 0.15$  is used in this thesis. It is difficult to exactly quantify the uncertainty associated with this parameter value. However, in the measurements performed in [35], the value of the yield coefficient does typically not vary more than a factor of  $\sim 10$  for the different situations considered. Therefore, with  $\gamma_{\text{ion}} = 0.15$ , the mechanism of ion bombardment is assumed to be modeled with a reasonable degree of accuracy.

Concerning the photoemission yield coefficient, the magnitude given above is not adjusted to account for photons of other wavelengths than the 98 – 102.5 nm band. Therefore, using this value would lead to a serious underestimate of the number of secondary electrons released by photoemission. However, obtaining a good value for  $\gamma_{\text{ph}}$  also accounting for the variety of different photon energies is difficult. Depending on the metal work function, the lowest photon energies at which photoionization starts to become efficient varies, as seen in figure 2.2. For the case of magnesium ( $\phi = 3.7$ ) for example, photons carrying energies as low as 3.5 – 4 eV are associated with an electron yield coefficient of the order of  $10^{-2}$ . However, such photons would hardly liberate any secondary electrons from a gold ( $\phi = 5.1$ ) surface. Another aspect to consider is how the photon intensity distribution as a function of wavelength might look like. In reality, a range of different mechanisms produce photons of various wavelengths. These include among others radiative emission from molecular nitrogen and oxygen, emission from inelastic scattering, radiative emission from processes such as recombination and attachment and bremsstrahlung to name a few. Giving a general theoretical treatment of this topic is beyond the scope of this thesis. However, a very rough estimate of  $\gamma_{\text{ph}}$  may be found using the following two simplistic assumptions:

- i) Photoemission does only occur for photons carrying energies within range 4.5 – 15.6 eV. Here, the lower limit correspond to a typical metal work function and the upper limit is the ionization potential of molecular nitrogen.
- ii) Within this energy range, all photon wavelengths are associated with the photoyield  $\gamma_{\text{ph}} = 0.2$ . In addition, their spatial intensity distribution is identical to the one obtained for the photons in the implemented 98 – 102.5 nm band.

With these assumptions, the implemented 98 – 102.5 nm band is accountable for a fraction of  $(12.7 - 12.1) \text{ eV} / (15.6 - 4.5) \text{ eV} = 5\%$  of the total photoemission. Subsequently, absorbing this fact into the photon yield  $\gamma_{\text{ph}}$  gives an effective magnitude  $\gamma_{\text{ph}} = 0.2 / 0.05 = 4$ . Although this is

certainly not an accurate estimate, it clearly illustrates the need for adjusting the yield coefficient to account for the effect of other photons of various wavelengths not included in the model.

### 3.6.2 Dielectric surfaces

Influx of photons from dielectric surfaces is implemented the same way as described for cathode surfaces. However, the yield coefficients are different for dielectric materials than for metals (see the next section for a discussion). As for metal surfaces, a free outflux of charged species is also implemented on dielectric surfaces. However, such a condition has a different physical interpretation here than at metal surfaces, as neutralization of charges does not occur. At dielectric surfaces, free outflux of charged species means, according to equation (3.3), that the charges attach to the material, leading to charging of the surface. Assuming that all charges incident on dielectric surfaces attach to the surface is a bit rough, but as discussed in section 2.4.5.2, at least surface attachment of electrons is found to be a dominating process. However, the author has found no data on the efficiency of ion attachment to dielectric surfaces.

When electrons are liberated from dielectrics, the net surface charge increases positively. In the Auger neutralization process (see section 2.2.2), two electrons are removed from the surface (one is used to neutralize the positive ion, and one electron is released to the gas) for every bombarding ion. The surface charge should therefore increase by two elementary charge units for every electron liberated by this mechanism. With attachment of the bombarding ions, followed by an influx of electrons, the charge balance on dielectric surfaces is correctly computed according to the this mechanism.

#### 3.6.2.0.1. Electron yield coefficients

Estimation of the electron yield coefficients for dielectric surfaces is even more difficult than for metal surfaces, as the internal electron band structure is in general more complex. Moreover, experimental data seems to be even more scarce than for the case of metal surfaces. For the materials investigated in [35],  $\gamma_{\text{ion}}$  was found to be lower for dielectric surfaces than for metals. At most, the difference was measured to be of one order of magnitude. Therefore, the value  $\gamma_{\text{ion}} = 0.05$  is used here. This is about half an order of magnitude less than the value adopted for metal cathode surfaces.

As described in the following chapter, experimental work has been carried out with a dielectric rod of relative permittivity  $\epsilon_r = 4.6$ . From the theoretical relation 2.28 and table 2.5, the work function of this material can be estimated to be somewhere between that of polyethylene (4.9 eV) and nylon 6 (4.3 eV) based on its dielectric constant. Due to lack of experimental data for the specific material used, the photon yield coefficient  $\gamma_{\text{ph}}$  is approximated by the yield of polyethylene as presented in figure 2.5c within the energy range 12.1 – 12.7 eV, giving a value  $\gamma_{\text{ph}} = 0.08$ .

As done for the photon yield associated with metal surfaces, this value should also be adjusted to also account for photoemission caused by photons of other wavelengths. Using similar assumptions as presented in the points i) and ii) in section 3.6.1.2.1, a rough estimate of an effective



value of  $\gamma_{\text{ph}}$  may be obtained. However, the energies required for efficient photoemission is higher than for the case of metals. Inspection of the curve of polyethylene in figure 2.5c reveals that  $\gamma_{\text{ph}} < 10^{-4}$  for energies below 8.5 eV. Therefore, in the following estimate, only photons of energies in the range 8.5 – 15.6 eV are assumed to contribute to photoemission. The contribution from photons carrying lower energies is assumed to be negligible, and the upper limit is the ionization energy of nitrogen as used before. This is contradictory to the hypothesis of Dubinova [1], as discussed in section 2.4.5.3 in the previous chapter, stating that photons of energies 2.27 – 4.63 eV play an important role in photoemission from dielectric surfaces. However, such an effect has not been observed, neither in experiments nor in simulations. Moreover, the electron yield associated with these photon energies is probably in the range  $10^{-13} - 10^{-9}$  for polyethylene (see figure 2.5a), which is extremely low. Even though low-frequency photons are more abundant far from the streamer head than higher frequency photons, it is the author’s opinion that the associated yield is too low to expect significant photoemission contribution. Assuming that all photons within the frequency range 8.5 – 15.6 eV are associated with the yield coefficient  $\gamma_{\text{ph}} = 0.05$  and that they have the same photon intensity distribution as obtained from the implemented 98 – 102.5 nm band, this band is accountable for a fraction of  $(12.7 - 12.1) \text{ eV} / (15.6 - 8.5) \text{ eV} = 8\%$  of the total photoemission. Adjusting  $\gamma_{\text{ph}}$  to account for these “missing” photons gives  $\gamma_{\text{ph}} = 0.08/0.08 = 1$ . See figure 3.2a for a visualization of the underlying assumptions used here. The 98 – 102.5 nm band is shown in red.

As with the estimated yield coefficient associated with photoemission from metal surfaces, it must be emphasized that the above yield magnitude is highly uncertain. For this reason, simulations have been done for a selection of different photon yield magnitudes (see the next chapters). For increased accuracy, the simplistic photoemission model used here should be replaced by a more advanced model explicitly treating photoemission from a range of photon energies. This is done by adding more frequency bands to the multigroup approximation as discussed earlier on. However, addition of too many bands causes the computational load to become prohibitively large. In practice, there will therefore always exist a trade-off between accuracy, represented by the width of each frequency band, and computational speed. Of course, the accuracy also depends on the number of included photon sources within each frequency band and how these are modeled. Figure 3.2b depicts a situation where five other frequency bands (dark gray) have been included, in addition to the implemented 98 – 102.5 nm band (red).

## 3.7 Numerical method

### 3.7.1 Implementation details

The model is implemented on top of the Chombo framework [80, 81], offering capabilities to efficiently solve partial differential equations on block-structured adaptively refined Cartesian grids. The framework also supports cut-cell representation of the embedded boundaries. The Chombo library is written using a combination of C++ and Fortran and is designed for code execution on multiple cores through use of the Message Passing Interface (MPI) standard. It also provides a range of built-in solvers for solving various types of differential equations.

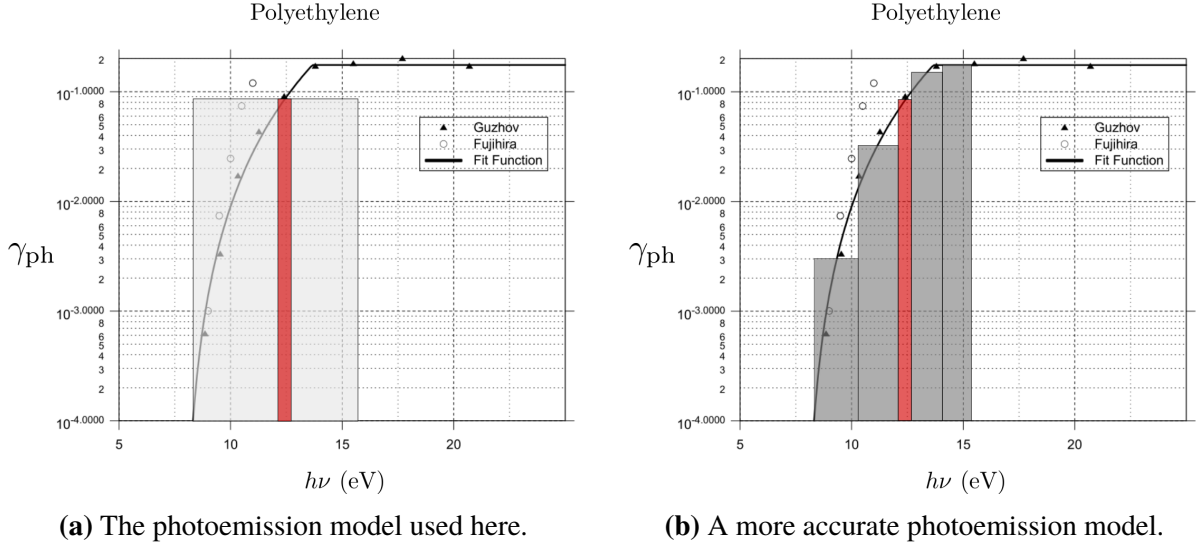


**Figure 3.2:** Illustration of two photoemission models: (a) All photons within the large energy band 8.5 – 15.6 eV (light gray region) are imparted the properties of the photons released within the implemented 98 – 102.5 nm band (red). (b) Five other frequency bands (dark gray) have been included, in addition to the implemented 98 – 102.5 nm band (red). Within each band, a monochromatic approximation is used.

## 3.7.2 Spatial discretization

### 3.7.2.1 Adaptive mesh refinement

As discussed in both the introduction and theory chapter, the dynamics of a streamer exhibit multiple different spatial scales, spanning from a few micrometres to the order of centimetres. In order to reduce the computational load and speed up the computations (especially for the case of three dimensional simulations), all equations presented in the previous sections are solved on an adaptive grids using adaptive mesh refinement techniques (AMR).

A typical simulation is plotted in figure 3.3, showing the electric field magnitude at the head of a positive streamer. As seen, the grid is much better resolved around the streamer head (read color) and in the streamer channel (blue color) than elsewhere. In fact, the computational domain consists of a hierarchy of various grids of unequal refinement. The grids are generated in such a way that the finest grid  $\Gamma^n$  is fully enclosed by a coarser grid  $\Gamma^{n-1}$ , which again is fully enclosed by yet a coarser grid  $\Gamma^{n-2}$  and so on, all the way up to the coarsest grid  $\Gamma^0$ . The refinement level between every two neighbouring grid levels is two, meaning that the grid spacing  $\Delta x$  of a coarser level is always twice the grid spacing of the next finer level.

Based on certain tagging criteria as discussed below, the computational grid is regenerated typically every 5 – 10 time steps in order to dynamically adapt the domain resolution as the streamer evolves. In the tagging stage, cells are tagged for refinement based on the tests summed up in table 3.2. As seen, similar tests are performed on the density  $n_\alpha$  of all the massive species, the charge density  $\rho = q(n_p - n_e + n_n)$  and for the electric potential  $\Phi$ . The user is self responsible

for setting the tagging threshold criteria. I.e. if one or more of the tests yield a magnitude which is above the threshold value set within a cell, the cell should be tagged for refinement. Obtaining good tagging threshold values for specific simulations typically requires some trial and error. In most cases it is sufficient to only include some of the tests in order to get satisfying meshing.

The use of a Cartesian grid makes the process of remeshing very efficient; if a cell is tagged for refinement it is subsequently cut into four smaller and equally sized rectangular cells in a straightforward manner. On unstructured grids, this operation would have been associated with significantly more computational overhead.

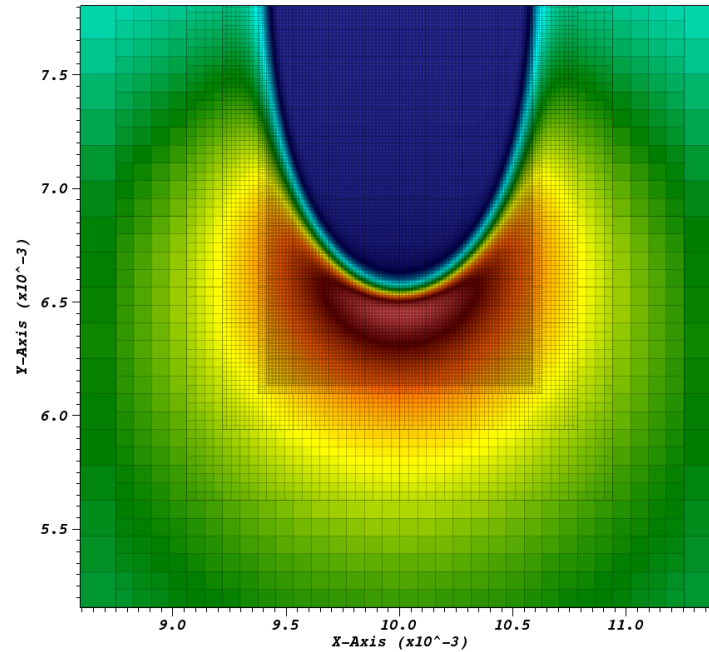


**Figure 3.3:** Illustration of the AMR hierarchy: various grid resolution is used in different parts of the computational domain. The figure displays the electric field magnitude of a positive streamer. The field is strongest in the red region just in front of the streamer head and weakest in the streamer channel (blue region). As seen, the mesh is best resolved in a close region around streamer and coarser resolution is used elsewhere.

Charged species $n_\alpha$	Charge density $\rho$	Electric potential $\Phi$
$\frac{ n_\alpha }{\max( n_\alpha )}$	$\frac{ \rho }{\max( \rho )}$	$\frac{ \Phi }{\max( \Phi )}$
$\frac{ \nabla n_\alpha }{\max( \nabla n_\alpha )}$	$\frac{ \nabla \rho }{\max( \nabla \rho )}$	$\frac{ \nabla \Phi }{\max( \nabla \Phi )}$
$\log( n_\alpha )$	$\log( \rho )$	$\log( \Phi )$
$\log( \nabla n_\alpha )$	$\log( \nabla \rho )$	$\log( \nabla \Phi )$
$\nabla n_\alpha \frac{dx}{n_\alpha}$	$\nabla \rho \frac{dx}{\rho}$	$ \nabla \Phi  \frac{dx}{\Phi}$

**Table 3.2:** Tagging tests performed on the volumetric densities of charged species  $n_\alpha$ , the charge density  $\rho = q(n_p - n_e + n_n)$  and the electric potential  $\Phi$  within each cell. If the magnitude of one or more of the tests within a cell are higher than a user-defined threshold, the cell is tagged for refinement.

### 3.7.2.2 The Poisson and Eddington equations

If compared, it may be noted that both the Poisson equation (3.12) and the RTE equation in the Eddington approximation (3.20) are similar. In fact, they are both elliptic Helmholtz-type equations, and their discretization is almost identical. The only difference is an extra diagonal term in the resulting discretization matrix in case of the Eddington equation. Both equations can therefore be solved using the same numerical routine, which is very advantageous. The two equations are discretized using a finite volume method, and since the approaches are analogous, the following discussion will limit itself to the Poisson equation.

Using a finite volume formulation, the Poisson equation (3.12) for a cell  $i$  may be written as [76]

$$\frac{1}{|V_i|} \left[ \sum_{faces \in V_i} \int_{face\ j} \hat{\mathbf{n}} \cdot \mathbf{F} \, dA \right] = \rho_i + \sigma_i. \quad (3.31)$$

Here,  $|V_i| = \nu_i \Delta x^D$  is the volume of the cell, where  $\nu_i$  is the cell volume fraction and  $D \in \{1, 2, 3\}$  is the dimensionality of the simulation. For cut-cells,  $\nu_i < 1$ , whereas for normal cells,  $\nu_i = 1$ . Furthermore,  $\mathbf{F} = \epsilon \nabla \Phi$  is the solution flux, and  $\hat{\mathbf{n}} \cdot \mathbf{F}$  is the part of the flux flowing normally through a cell face  $j$  ( $\hat{\mathbf{n}}$  is a unit vector normal to a given face pointing outwards).  $\rho_i$  and  $\sigma_i$  are respectively the charge density and the dielectric surface density within a cell. The sum is to be taken over all the cell faces and the integral over a cell face  $j$  is approximated using the midpoint method, giving

$$\int_{face\ j} \hat{\mathbf{n}} \cdot \mathbf{F} \, dA = \alpha_j \epsilon \Delta x^{D-1} \frac{\partial \Phi}{\partial n} \bigg|_{face\ centroid} \equiv F_j \quad (3.32)$$

As indicated in the above equation, the boundary flux for a face  $j$  should be evaluated at the face

centroid. For normal cells, all the face centroids coincide with the face centers, and the face fractions  $\alpha_j = 1$ . However, this is not in general true for cut-cells, where two of the cell faces are cut by an embedded boundary (EB). See figure 3.5 for an illustration. The magnitude of the electric permittivity  $\epsilon$  is stored at the centroid of all face cells.

All fluxes associated with faces having a face fraction  $\alpha_j = 1$  are calculated using the second order central difference approximation

$$\frac{\partial \Phi}{\partial n} = \frac{1}{\Delta x}(\Phi^+ - \Phi^-), \quad (3.33)$$

where  $\Phi^+$  and  $\Phi^-$  are respectively the cell centered values of the solution computed at the cells located at the high and low sides of the face in direction  $d$ . For normal cells, equation (3.31) thus reduces to the standard star-shaped 5(7)-point finite difference stencil in two (three) dimensions for the laplacian. Note that by using the stepwise approach for representation of dielectric interfaces when solving the Poisson equation, as discussed in section 3.1.1, all normal cell fluxes are either evaluated along the dielectric interface or at points fully embedded either within the gas phase or the dielectric. See figure 3.4 for a sketch. Since  $\mathbf{F} = \epsilon \nabla \Phi = \epsilon \mathbf{E}$ , this means that the electric field  $\mathbf{E}$  is never evaluated across any dielectric surfaces, and the discontinuity condition discussed in section 3.12 does not need to be invoked. Consequently, cells cut by dielectric interfaces do not need special treatment when solving the Poisson equation.

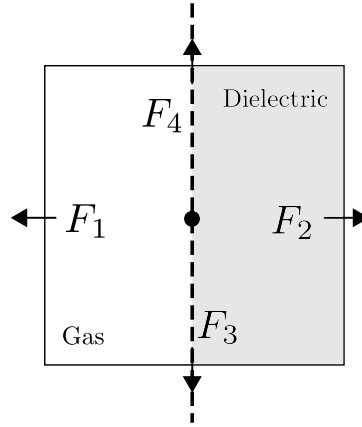


**Figure 3.4:** Sketch of a cell cut by a dielectric interface when solving the Poisson equation. The fluxes  $F_3$  and  $F_4$  are evaluated along the dielectric surface, whereas the fluxes  $F_1$  and  $F_2$  are fully embedded within the gas phase and the dielectric respectively. Since  $\mathbf{F} = \epsilon \nabla \Phi = \epsilon \mathbf{E}$ , this means that the electric field  $\mathbf{E}$  is never evaluated across any dielectric surfaces.

As described in in section 3.1.1, both conductor boundaries and dielectric boundaries are represented using cut-cells when solving the the Eddington equation, whereas when solving Poisson's equation, only conductor boundaries are represented in this way. Centroid fluxes associated with faces having a face fraction  $\alpha_j < 1$ , such as the fluxes  $F_2$  and  $F_4$  in figure 3.5b, are found through linear interpolation using nearby face-centered fluxes as described in [82].

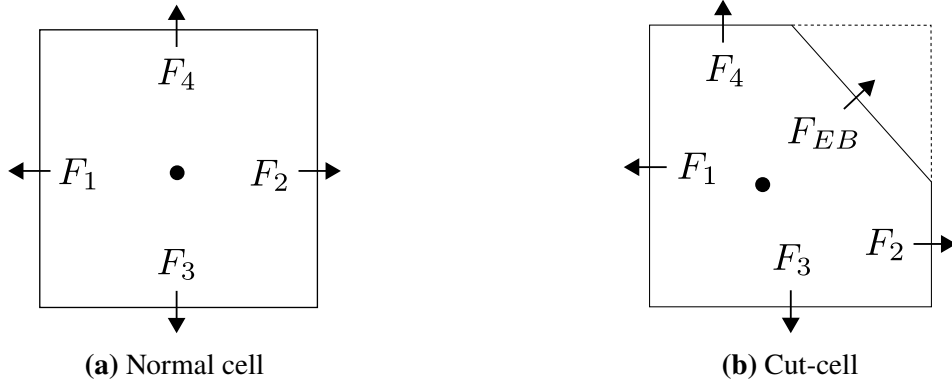


**Figure 3.5:** A two-dimensional illustration of the fluxes out of a cell  $i$  in the case of (a) a normal cell and (b) a cut-cell. The fluxes are computed according to equation (3.32) and added in confinement with equation (3.31). As indicated, all the fluxes are evaluated at the face centroids. The cell centroids are marked with a black dot and the flux denoted “EB” goes into an embedded boundary.

#### 3.7.2.2.1. Embedded boundary fluxes

As discussed in section 3.3.1, the Poisson boundary conditions are either of Neumann or Dirichlet type. In the case of Neumann conditions, the boundary fluxes, such as the flux  $F_{EB}$  in figure 3.5b, are given directly. However, if a Dirichlet condition is specified, the boundary fluxes need to be approximated. Specifics are given in [82], but the outline of the method used is as follows: a ray is cast into the gas phase normally from the centroid of the embedded boundary face. Second order interpolation of the cell-centered solution using nearby grid points is then used to obtain the value of  $\Phi$  at preferably two points along the ray. These points are then used to construct a Newton polynomial interpolation formula. Upon differentiation, the value of  $\partial_n \Phi$  at the embedded boundary face is then approximated with second order accuracy, provided that the interpolation formula was given with a third order accuracy (i.e the formula was based on three points along the ray). However, in some situations there are simply not enough cells available to obtain a third order Newton polynomial formula. In those cases, a first order approximation of  $\partial_n \Phi$  is obtained. If there are too few cells available even for a first order approximation, the derivative is approximated using a least squares method.

Regarding the Eddington equation, no values of the solution nor the solution flux are prescribed at embedded boundaries. Instead,  $\partial_n \Psi_{0,\gamma}$  is given by equation (3.25). Thus, the boundary fluxes may be found, provided that  $\Psi_{0,\gamma}$  is known at centroids of the embedded boundary faces. The boundary value of the solution is calculated using a second order Taylor series based extrapolation scheme (see for example [83]). Also in this case, lack of available stencil points may require the solver to drop to first order or to a least squares method.

### 3.7.2.2.2. Solver considerations

Numerical discretization of the Poisson and Eddington equations effectively transforms the continuous equations into a set of discrete equations. Canonically, such equation sets are described by the matrix equation

$$\mathbf{A}\mathbf{y} = \mathbf{b}, \quad (3.34)$$

where  $\mathbf{A}$  is the discretization matrix,  $\mathbf{y}$  is a vector containing the solution at all the discrete cell-centered domain points and  $\mathbf{b}$  is a vector containing the source term contributions at each of these points. All numerical approaches for solving (3.34) may be categorized as either direct or iterative solver methods [1]. In the latter case, the methods are also referred to as relaxation methods. Direct solver techniques are based on inversion of the discretization matrix  $\mathbf{A}$ , whereas iterative techniques involve repetitious improvement upon an initial guess until satisfactory convergence to the real solution is achieved.

Multiple software packages, such as the PETSc package [84], provide solvers which can be readily used to solve (3.34). Direct solvers may take advantage of the fact that the matrix  $\mathbf{A}$  is sparse, symmetric and positive definite for increased efficiencies [1]. However, inversion of  $\mathbf{A}$  is generally still a computational inefficient process. In addition, such a process requires a large amount of memory. On static grids, inversion of the matrix may only need to be done once and then stored for later usage. However, on dynamical adaptive grids, as used in this work, a new inverted matrix would be required after each regridding operation.

Because of the above described limitations of direct methods, an iterative solver for solving the Poisson and Eddington equations was chosen for efficiency. In addition, iterative solvers require less memory than direct solvers. In general, iterative methods can be very efficient, depending on the smoothness of the solution. However, the convergence rate of iterative methods often quickly decays as the number of iterations increases. This is an inherent issue associated with such methods and the reason can be understood by expanding the error  $\mathbf{e}$ , defined as

$$\mathbf{e} = \mathbf{y}_{\text{true}} - \mathbf{y}_{\text{num}}, \quad (3.35)$$

into a Fourier series. Here,  $\mathbf{y}_{\text{true}}$  is the exact solution to (3.34), while  $\mathbf{y}_{\text{num}}$  is the numerical solution. Examining the Fourier series, it may then be shown [85] that relaxation methods very efficiently removes the high-frequency Fourier components of the error. However, the magnitudes of the smooth low-frequency components are not efficiently reduced. In this work, a geometric multigrid solver method has been adopted. This method overcomes the issue of slow convergence by defining and solving the equations over a hierarchy of grids of different refinements. On each grid, conventional relaxation approaches are applied. The method basics are outlined in the following.

## 3.7.2.2.3. The AMR multigrid method

The geometric multigrid method is highly compatible with adaptive meshing and has a theoretical optimal run time [83]. The implementation used here is provided by Chombo and follows the work of Martin and Cartwright [86]. For a full introduction to the subject of multigrid, see for example the book by Briggs [85]. The following text is largely based on previous work [76] done by the author.

From equations (3.34) and (3.35) it can easily be shown that the error  $e$  obeys the relation

$$\mathbf{A}e = \mathbf{r}, \quad (3.36)$$

where

$$\mathbf{r} = \mathbf{b} - \mathbf{A}\mathbf{y}_{\text{num}} \quad (3.37)$$

is termed the *residual*. The equation (3.36) is therefore referred to as the residual equation, and it has the same form as the main equation (3.34). The multigrid method is actually formulated in terms of this equation, rather than (3.34). After a good estimate of the error is obtained, starting from an initial guess, the solution  $\mathbf{y}_{\text{true}}$  is found through the relation (3.35).

The basic idea behind the multigrid method is that a smooth wave looks more oscillatory on a coarse grid than on a fine grid, because the number of points used to resolve the wave is then reduced. When the convergence speed of iterative solvers starts to decay, it means that mostly long-waved Fourier components of the error is left. When this happens, the approach is to restrict the entire problem, in form of the residual equation, onto a coarser grid. Here, the iterative solver may again be effective. This method is successively applied over a hierarchy of coarser and coarser grids. On the coarsest grid, the number of cells is so massively reduced that the error can efficiently be found by a direct solver. After the direct solution has been obtained, the process is reversed; the error is now interpolated onto the finer grids, all the way up to the finest grid. The interpolated values are added to the error estimates already obtained on the way down the cycle and represent a correction to these earlier estimates. After adding the errors, a few iterations of the iterative solver is performed, before the error again is interpolated onto a finer grid. The multigrid cycle is finished when the finest grid has been updated with interpolated values, and the full process is referred to as a V-cycle (see figure 3.6). A number of such V-cycles is performed in order to get the desired solution accuracy. After each cycle, the estimated solution gets more and more accurate, because the output of one V-cycle is used as the starting point for the next. In this work, the iterative solver is a Gauss-Seidel solver with red-black ordering. This solver is well suited for parallel computations.

The above scheme is not confined to the AMR grid hierarchy. Theoretically, the coarsening may continue until the computational domain only consist of  $2 \times 2$  cells. However, this would cause the embedded boundaries to be significantly under-resolved. Also, cases may arise where the stencils used to calculate the conductor fluxes on coarser grids are no longer a good approximation of the corresponding fluxes calculated at finer grids. Both these issues cause the



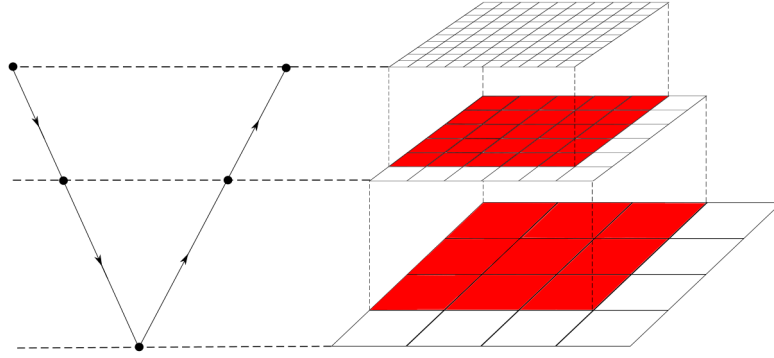


**Figure 3.6:** Illustration of the concept of AMR multigrid. The V-cycle is depicted to the left. At all points marked with a black dot, a few iterations of an iterative solver is performed. On the way down the cycle, the problem, in form of the residual equation (3.36), is restricted onto coarser and coarser grids. On the coarsest grid level, an exact solution is obtained by means of a direct solver. The solution is then interpolated back up the chain of nested grids until the finest grid level is reached, completing the process. The figure is taken from [76]

convergence rate to drop. In reality, the direct solver is therefore set to kick in before the coarsening gets this far. However, the AMR multigrid method is generally most efficient the longer the coarsening is allowed to continue. When using complex geometries, a reduced efficiency is therefore unavoidable. Moreover, due to the complexity of the algorithm, the method is typically less robust than for example direct solver methods.

### 3.7.2.3 The hydrodynamic equations

For the spatial discretization of the hydrodynamic equations, the second order accurate Godunov's method with Van Leer Limiting has been implemented. The method is rather involved mathematically, and the reader is referred to [87] for details. As described in the theory section, streamers in air at STP are associated with a micrometer-thin layer of positive space charge surrounding the streamer channel, slowly expanding outwards due to ambipolar diffusion. This layer may be seen as a shock-front, and accurate modeling of this phenomenon requires special methods associated with minimal numerical diffusivity. Simple low-order upwind schemes are for example too diffusive, and would lead to the shock front being smeared out in space as the streamer evolved. As a countermeasure, unphysical artificial viscosity is therefore often added to such schemes [83]. However, Godunov's method is very little diffusive, and shock fronts modeled using this discretization method largely retains its shape as time progresses. However, when modeling shock waves using high resolution schemes, spurious oscillations are often induced around the shock front due to the steep solution gradient [88]. In order to prevent this phenomenon, so-called flux limiters, such as that of Van Leer as used here, are introduced. The effect of flux limiters is to limit the solution gradient around discontinuities so that solution wiggles are avoided.

3.7.2.3.1. *Embedded boundary fluxes*

The embedded boundary fluxes are calculated by the same approach as used for the Eddington equation, i.e a second order Taylor series based extrapolation scheme is adopted in order to obtain  $n_\alpha$  at the embedded boundary centroids. If a second order stencil cannot be constructed, a first order approach is used instead. As a last resort, the fluxes are calculated by a least squares based extrapolation.

## 3.7.3 Temporal discretization

## 3.7.3.1 Time stepping method

In this work, a second order explicit Runge-Kutta method has been implemented for solving the hydrodynamic equation (3.2) and the scalar conservation equation (3.27). Both equation types can be collapsed to the generic form

$$\frac{\partial y}{\partial t} = f(t, y). \quad (3.38)$$

In the case of the drift-diffusion-reaction equation,  $y = n_\alpha$  and  $f = R_\alpha - \nabla \cdot (\pm \mu_\alpha \mathbf{E} n_\alpha - D_\alpha \nabla n_\alpha)$ , whereas for the scalar conservation equation,  $y = \sigma$  and  $f = F$ . The method for advancing the solution from a time  $t_n = n\Delta t$  to a time  $t_{n+1} = t_n + \Delta t$  is given by [13]

$$y_{n+1} = y_n + \Delta t \left[ \left(1 - \frac{1}{2\alpha}\right) f_n + \frac{1}{2\alpha} f_{n+\alpha} \right], \quad (3.39a)$$

where

$$f_n = f(t_n, y_n), \quad (3.39b)$$

$$f_{n+\alpha} = f(t_n + \alpha\Delta t, y_n + \alpha\Delta t f_n). \quad (3.39c)$$

Here, the notation  $y_n$  is used to denote the solution  $y$  at time  $t_n$  and  $\alpha \in (0, 1]$  is a coefficient determining an intermediate time step at which the state of the system should be evaluated. With  $\alpha = 0.5$  and  $\alpha = 1$ , the scheme (3.39) reduces to the midpoint method and Heun's method respectively. Note that the expression  $y_n + \alpha\Delta t f_n$  included in (3.39c) for  $f_{n+\alpha}$  is a first order approximation of  $y_{n+\alpha}$ , i.e

$$y_{n+\alpha} \approx y_n + \alpha\Delta t f_n. \quad (3.40)$$

This effectively means that the solution needs to be obtained at two points in time, namely at  $t_n$  and at  $t_{n+\alpha}$ , in order to calculate the solution at  $t_{n+1}$ . Since both the hydrodynamic equation and the scalar conservation equation is a function of the electric field  $E$ , in addition to the photon

distribution function  $\Psi_{0,\gamma}$ , it is necessary to also solve the Poisson and Eddington equations at both  $t_n$  and at  $t_{n+\alpha}$ . In contrast, the common 4'th order Runge-Kutta routine would have required calculation of  $y$ ,  $E$  and  $\Psi_{0,\gamma}$  at *four* separate points in time in order to obtain  $y_n$ . This consideration was the reason why only a second order method was adopted, as the use of a higher order method would have significantly increased the code execution time.

### 3.7.3.2 Time step restrictions

In order to ensure stable and accurate temporal evolution of the model equations, three different restriction criteria on the time step  $\Delta t$  has been implemented. Firstly, the Courant-Friedrichs-Lewy (CFL) criterion is given by

$$\Delta t_{CFL} = \eta_{CFL} \min \left( \sum_{d=0}^{D-1} \frac{\Delta x}{u_d} \right), \quad (3.41)$$

where  $D$  is the simulation dimensionality,  $u_d$  is the electron fluid velocity magnitude in the spatial direction  $d$  and  $\Delta x$  is the corresponding spatial discretization length. The min operator runs over all the domain cells. Furthermore,  $\eta_{CFL} \in (0, 1)$  is a user-controlled fudge factor for managing the above criterion. Since an explicit time stepping scheme is used, a necessary stability criterion is that  $\eta_{CFL} < 1$ .

The second time step restriction criterion determines how much the electric field  $\mathbf{E}$  is allowed to vary within a single time step. From Ampère's law, the temporal variation of the electric field  $\mathbf{E}$  is given by

$$\epsilon_0 \frac{\partial \mathbf{E}}{\partial t} = \mathbf{J} \quad (3.42)$$

if all magnetic effects are neglected. Here,  $\mathbf{J} = -q\mu_e n_e \mathbf{E}$  is the electron current ( $q$  is the elementary charge). Using an explicit forward Euler discretization scheme, equation (3.42) can be discretized as

$$\epsilon_0 \frac{\mathbf{E}_{n+1} - \mathbf{E}_n}{\Delta t} = \mathbf{J}. \quad (3.43)$$

The dielectric relaxation time  $\Delta t_\epsilon$  is computed by requiring that the electric field in the above equation should not change more than  $\eta_\epsilon \mathbf{E}_n$  between two time steps, i.e.  $\mathbf{E}_{n+1} - \mathbf{E}_n = \eta_\epsilon \mathbf{E}_n$ . Here,  $\eta_\epsilon$  is yet a fudge factor, allowing the user to fine-tune the restriction threshold value. The criterion is given as

$$\Delta t_\epsilon = \eta_\epsilon \min_d \left( \frac{\epsilon_0 E_d}{J_d} \right), \quad (3.44)$$

where  $E_d$  and  $J_d$  is respectively the electric field and the electric current in the spatial direction  $d$  evaluated at the current time step  $t_n$ . Furthermore, the  $\min_d$  operator is applied on all cells

and in all spatial directions.

Finally, a last restriction on the time step is set by imposing that the electron and ion densities should not grow more than  $\eta_n n_\alpha$  between two time steps. This condition is only applied to the cell(s) where  $n_\alpha$  has a maximum. Discretizing the temporal term of the hydrodynamic equation (3.2) using a forward Euler scheme and requiring that  $n_\alpha^{n+1} - n_\alpha^n = \eta_n n_\alpha^n$  yields

$$\Delta t_n = \eta_n \frac{n_\alpha}{f_\alpha}. \quad (3.45)$$

Here,  $f_\alpha = R_\alpha - \nabla \cdot (\pm \mu_\alpha \mathbf{E} n_\alpha - D_\alpha \nabla n_\alpha)$  and both  $n_\alpha$  and  $f_\alpha$  should be evaluated at the current time step  $t_n$ .

With all three of the above criteria (3.41), (3.44) and (3.45) calculated, the actual time step used is computed as

$$\Delta t = \min(\Delta t_{CFL}, \Delta t_\epsilon, \Delta t_n). \quad (3.46)$$

A similar way of limiting the time step is for example used in [89].

### 3.8 Model limitations

The streamer model presented here is based on several simplifications and approximations, each placing certain restrictions on the model. When performing simulations, it is important to keep these limitations in mind so that the model is only used within the range of validity of the underlying approximations.

The biggest limitation is that the model itself is based on a fluid approximation. As described earlier on, this approximation is only valid as long as the local Knudsen number defined in equation (3.3) is larger than 0.05. In cases where the densities of the massive species are very low, as for example in the early inception phase, the model is in general not valid. In such situations, more general particle-based approaches, as outlined in chapter 1, must be used. In addition, the model is deterministic, meaning that repetitive runs using identical input parameters gives the same results. In reality, streamers discharges are stochastic. In fact, it is the stochastic nature of streamers which gives rise to streamer branching. This phenomenon is therefore not possible to recreate in a deterministic model.

Another limitation is the use of the Eddington approximation for modeling photon transport. The foundation of this approximation is, as described in section 3.4.1, that the spherical harmonic expansion of the photon distribution function is very dominated by the first isotropic term  $\Psi_{0,\nu}(\mathbf{x}, t)$ . Therefore, the expansion may be truncated after the second term involving the first anisotropy correction  $\Psi_{1,\nu}(\mathbf{x}, t)$ . In the Eddington approximation, this quantity is given by equation (3.19), which is restated here for convenience (but in a slightly different form):

$$\Psi_{1,\gamma}(\mathbf{x}, t) = -\frac{1}{3\kappa_\gamma} \nabla \Psi_{0,\gamma}(\mathbf{x}, t). \quad (3.47)$$

Firstly, in order for the Eddington approximation to be valid,  $\Psi_{1,\gamma}(\mathbf{x}, t)$  should be small compared to  $\Psi_{0,\gamma}(\mathbf{x}, t)$ . More specifically, the factor

$$\Re = \frac{|\Psi_{1,\gamma}(\mathbf{x}, t)|}{\Psi_{0,\gamma}(\mathbf{x}, t)} \sim \frac{1}{\kappa_\gamma} \frac{|\nabla \Psi_{0,\gamma}(\mathbf{x}, t)|}{\Psi_{0,\gamma}(\mathbf{x}, t)} \quad (3.48)$$

should be much less than one. Here, equation (3.47) was used in the last transition. The validity of the Eddington approximation is in other words dependent on the inverse of the photon absorption length  $\kappa_\gamma$ . For very short-waved photons,  $\kappa_\gamma$  is small, and the Eddington approximation is justified. However,  $\kappa_\gamma$  is larger for long-waved photons, meaning that the approximation is more questionable (unless the factor  $|\nabla \Psi_{0,\gamma}(\mathbf{x}, t)|/\Psi_{0,\gamma}(\mathbf{x}, t)$  is small).

Secondly, it must be noted that equation (3.47) has the same form as Fick's law of diffusion [90]. Resultantly, all domain points associated with a nonzero photon distribution function are subject to photon diffusion. Far away from sharp geometrical objects, this effect proposes no physical discrepancies. However, photon diffusion leads to a non-physical bending of photon paths around sharp corners. This effect is an intrinsic property embedded in the Eddington approximation and cannot be "turned off" or in any way reduced.

Of more easily fixable limitations is the fact that only two generic ionic species is used in this work. As described earlier on, this is a valid and much used approximation. However, more sophisticated models should include more ionic species for increased accuracy. A good starting point is the article by Kossyi et al. [91], providing several hundred empirical and theoretical rate coefficients for a range of different physicochemical reactions occurring in nitrogen-oxygen mixtures. Based on a selection of these reactions, Pancheshnyi et al. [63] have for example proposed a model consisting of seven distinct ionic species.

For better accuracy, a more sophisticated photoionization model including more photon bands should also be implemented. This would in addition allow for a more accurate calculation of photoemission. Finally, a method such as that proposed by Crockett et al. [18] should be adopted in order to permit dielectric interfaces to be represented using cut-cells when solving the Poisson equation.



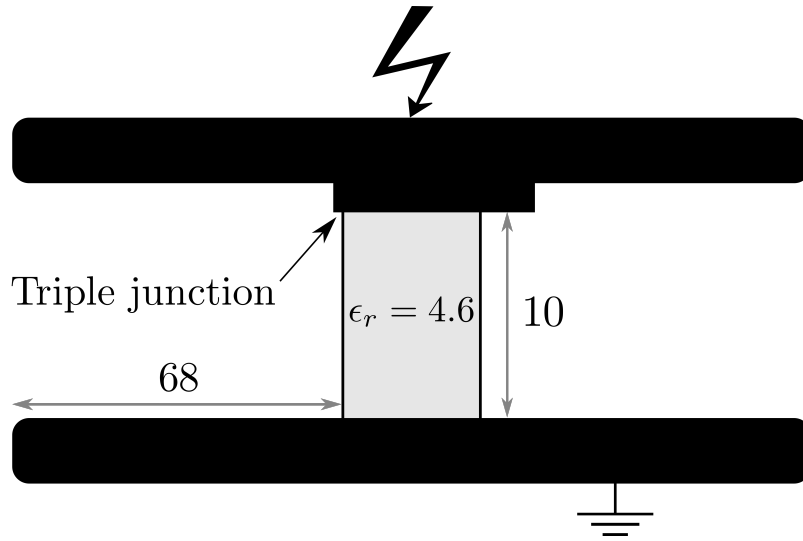
# Chapter 4

## METHOD

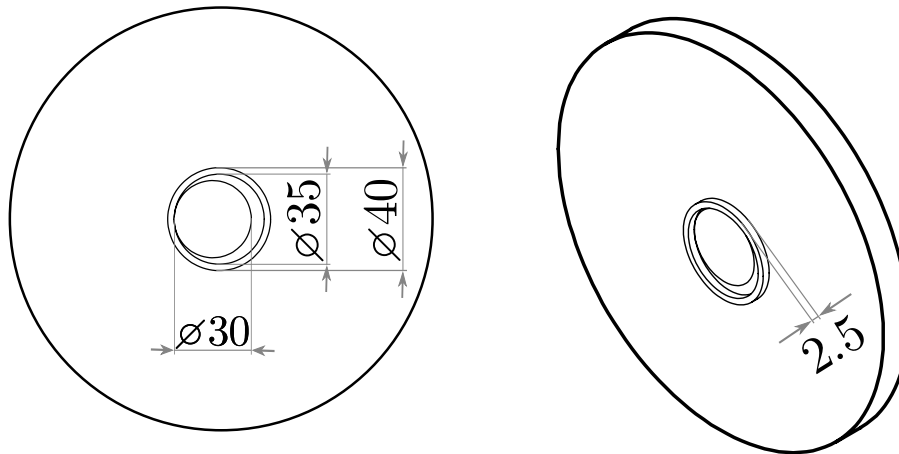
As described in the introduction chapter, both numerical simulations and experimental work have been conducted over the course of this thesis. The process of obtaining experimental data of comparable quality to numerical data is in general not straightforward. Firstly, laboratory discharges are conventionally measured in terms of macroscopic quantities like discharge currents, voltages and total discharge luminosities. However, such data holds no information about the fine-scale spatial distribution of for example electron and ion densities, the electric field and photon intensities as obtained from numerical simulations. Therefore, direct comparison between such data outputs cannot be performed. Secondly, even when modeling streamer discharges within the fluid approximation and making use of AMR, streamer simulations are still computationally expensive (especially in 3D). In practice, limited computational resources and run time considerations effectively put upper limits on the spatial dimensions feasible for streamer simulations. In order for proper comparison, the experimental and numerical configurations should be identically scaled. However, performing experimental measurements on small configurations poses strict demands to the accuracy of the measurement devices, as discharges on such length scales usually occur over the course of some tens of nanoseconds. Nevertheless, despite of the above mentioned challenges, an effort has been made to obtain comparable experimental data using a high-speed camera.

### 4.1 Experiments

The experimental configuration is shown in figure 4.1, along with exact geometrical measures. Two parallel aluminum discs are joined by a cylindrical 10 mm dielectric rod of relative permittivity  $\epsilon_r = 4.6$  running through their centers. The rod is made of POM with added 25% glass fiber and has a diameter of 30 mm. A small metal ring encircling the rod is attached obliquely to the top electrode so that it only touches the dielectric cylinder at one point, effectively forming a triple junction.



(a) Side view of the configuration seen from the position of the camera.



(b) Top electrode/anode geometry.

**Figure 4.1:** Experimental configuration (not to scale!): A cylindrical dielectric POM rod of relative permittivity  $\epsilon_r = 4.6$  is attached between two parallel aluminum disks through holes in their centers. A small metal ring is fixed obliquely around the center hole of the top electrode in such a way that it touches the dielectric only at one point, forming a triple junction. The geometry of the upper electrode (the anode) is shown in (b). The anode is put under a positive DC high-voltage stress, whereas the lower electrode (the cathode) is grounded. All the sizes indicated in the figures have the unit of millimetres.



The anode was stressed with a 20 kV 1.2/50  $\mu\text{s}$  positive DC pulse for positive streamer inception, generated by a 1.2 MV impulse generator. This means that the time for the signal to rise between 30% and 90% of maximal magnitude was 1.2  $\mu\text{s}$  and that the decay time to 50% of maximal value was 50  $\mu\text{s}$ . The spatiotemporal dynamics of the streamers were encaptured by an Imacon 468 ICCD high-speed camera producing 7 frames, each with a minimal exposure time of 10 ns. The camera was triggered by a delay-generator whose delay time was set manually. The work of tuning the delay time so that the camera was triggered at the exact moment when the streamer discharges occurred was a painstaking process. In addition to requiring nanosecond precision, capturing a discharge also involves a large portion of chance, as streamer inception is an inherent stochastic process. Therefore, arresting a streamer discharge typically required more than ten attempts. In between every attempt, the dielectric rod should have been wiped clean with isopropanol in order to remove any excess charge remaining on the material surface from the previous discharge. However, the camera was only available to the author for a limited amount of time. The process of wiping the rod after every try was therefore unfortunately not feasible in practice, as it would simply take up too much time. The rod was subsequently wiped clean only in between every 4-5 attempts.

The high-speed camera was used with a 85 mm f/1.8 Nikkor lens and placed within a Faraday cage at a distance of approximately 1 m from the experimental object. The lens is very light-sensitive, but lacks the property of optical zoom. Due to practical considerations, the object could not be moved closer to the camera, and as a result, the centimetre-sized gap was not resolved to a fully satisfactory degree. Therefore, all images were digitally processed for enhanced resolution. Also, since streamers do not emit much light, the contrast and brightness in each image was increased. For unbiased comparison between the different frames, all parameters were adjusted to the same levels.

To supplement the images, both the discharge current and the total discharge light intensity were measured. In addition, the anode voltage was also measured. The light intensity was recorded using a Philips AVP photomultiplier (PMT), with a supply voltage of 2.5 kV. A filter was applied to restrict the photon detection range to 350 – 600 ns. Further details about the full experimental set-up is found in the article by Meyer et al. [92], depicting a set-up identical to that used here. All experiments were carried out in ambient air at a temperature of 22°C, a pressure of 0.98 atm and a 34% relative air humidity.

## 4.2 Simulations

### 4.2.1 Triple junction geometry

The triple junction geometry used for 2D simulations is shown in figure 4.2, and was taken as the cross section of the experimental configuration. The dielectric rod is indicated in gray, whereas the aluminum ring is colored black. At the triple point, the distance between the metal ring and the dielectric rod was estimated to be 0.2 mm. Moreover, the radius of curvature of the corners of the cross sectional representation of the ring was approximately 0.15 mm.

The aluminum disc-shaped electrodes are not included in the computational domain. Instead,

their effects on the electric potential  $\Phi$  are included through Dirichlet boundary conditions. As described in the previous section, a pulsed positive DC voltage was applied to the anode in the laboratory experiments. However, the voltage does not change too much within the nanometer time frame of the streamer discharges. Therefore, a constant potential of 18.5 kV was set as boundary conditions on the upper domain wall and on the metal ring. As seen in figure 5.2 in the next chapter, this value approximately corresponds to the inception voltage measured in the experiments. At the lower domain wall, the potential was set to zero. On both the domain boundaries running parallel to the dielectric rod, zero flux conditions ( $\partial_n \Phi = 0$ ) were used.

All the simulations were initiated with a density of  $10^4$  electron-positive ion pairs per  $\text{cm}^3$ , corresponding to a normal background ionization level as discussed in section 2.4.4 in the theory chapter. As argued in the previous chapter, the values  $\gamma_{\text{ion}} = 0.05$  and  $\gamma_{\text{ph}} = 1$  were adopted for positive ion and photon bombardment on dielectric surfaces.

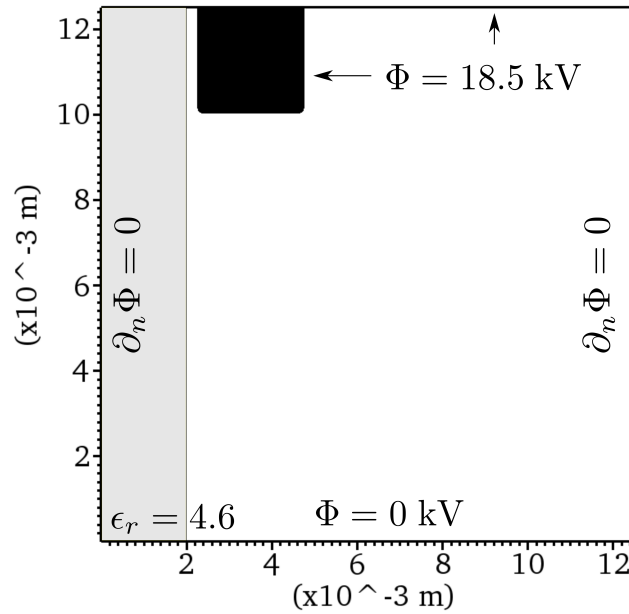


**Figure 4.2:** Triple junction geometry: The geometry is based on the cross section of the experimental configuration. The cross section of dielectric rod ( $\epsilon_r = 4.6$ ) is shown in gray, whereas the cross section of the aluminum ring is colored black. The electrode discs are present in form of Dirichlet boundary conditions applying to the electric potential  $\Phi$  on the upper and lower domain walls. These are indicated, along with the Neumann boundary conditions used on the two other domain boundaries. The distance between the dielectric and the metal ring at the point of the triple junction is 0.2 mm and the radius of curvature on the corners of the cross section of the ring is taken to be 0.15 mm.

### 4.2.2 Rod-plane geometry

The second geometry used for 2D simulations is depicted in figure 4.3. A metal rod (black) with a hemispherically capped tip is placed at a distance of 0.5 mm above a dielectric plate (gray) of relative permittivity  $\epsilon_r = 4.6$ . The tip of the rod has a radius of curvature of 0.1 mm. All

other sizes may be found using the figure axes. The boundary conditions used with the Poisson equation are also indicated in the figure. The rod (anode) and the upper domain wall are stressed with a positive voltage of 6 kV for positive streamer inception, whereas the lower domain wall is grounded ( $\Phi = 0$ ). Like for the case of the triple junction simulations, the initial background ionization was set to  $10^4$  electron-positive ion pairs per  $\text{cm}^3$ .

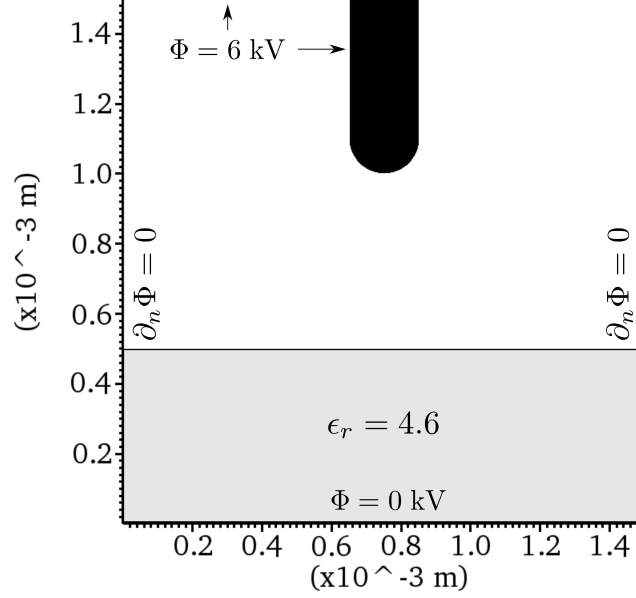


**Figure 4.3:** Rod-plane geometry: A hemispherically capped metal rod (black) is placed a distance of 0.5 mm above a dielectric plate (gray) of relative permittivity  $\epsilon_r = 4.6$ . The hemispherically shaped tip has a radius of curvature of 0.1 mm and the rod diameter is 0.2 mm. The Poisson boundary conditions used on the domain walls and on the conductor surface are indicated.

As described in section 3.6.2 in the previous chapter, the magnitude of the electron yield coefficient  $\gamma_{\text{ph}}$  for photon bombardment on dielectric surfaces is highly uncertain. In order to probe how the dynamics of streamers propagating on the surface of dielectrics are affected by variations in this coefficient, several simulations with different values of  $\gamma_{\text{ph}}$  have been carried out. The magnitudes tested for was  $\gamma_{\text{ph}} = \{0.1, 1, 10\}$ .



# Chapter 5

## RESULTS AND DISCUSSION

### 5.1 Experiments

The best image series recorded, along with the measured anode voltage and PMT readings are shown in figures 5.1 and 5.2. The electrodes are indicated with yellow dashed lines and a coloring scheme is used to indicate the temporal positioning of the frames with respect to the measured anode voltage and the PMT signal. An exposure time of 190 ns was used for the first frame, whereas the second and third frames were obtained using exposure times of 10 ns. In later frames, the streamer channel starts to thermalize. As this thesis only consider the first streamer stage, these frames are therefore excluded.

Frames 2 and 3 (figures 5.1b and 5.1c respectively) clearly show streamer activity. From inspection of the PMT signal at the times when these frames were exposed, it is evident that the emitted light is intense enough to put the recordings out of range, as only PMT voltages within the interval  $-0.8 - 0.2$  were measured. Studying the figures, most of the streamer activity occurs on the left side of the rod, where the triple junction is located. However, some activity may also be seen on the other side of the rod. The discharge on the left side of the rod can be characterized as a bright channel with diffuse “edges”, which are most likely a result of strong streamer branching to either sides along the dielectric surface. However, due to the limited resolution of the images it is not possible to identify individual streamer paths. Despite this fact, it seems to be the case that most of the branching streamers actually propagate on the surface of the dielectric, rather than in the surrounding air (although in frame 3, the width of the discharge channel has increased, suggesting that a larger portion of the branching streamers propagate in the air just next to the dielectric). This indicates that the presence of the dielectric has a guiding effect on the discharge path.

In contrast to frames 2 and 3, no activity is seen in frame 1. Since frame 2 shows streamer activity along the entire rod length, it means that the discharge has crossed the gap in less than 10 ns, equivalent to the frame 2 exposure time. This gives a lower streamer velocity estimate  $v = 1 \text{ mm/ns}$ . However, the PMT recordings clearly indicate light activity towards the end of

the frame 1 exposure, after approximately  $8.74 \mu\text{s}$ . An explanation to why the camera did not capture this is that the emitted light was very dim so that only the PMT, being more sensitive than the camera, was able to record it. In this case, the discharge captured in frame 2 is not a primary streamer discharge, but rather a secondary streamer propagating in the ionized channel produced by the first streamer. The abundance of electrons would most likely cause the secondary streamer to propagate with a higher velocity than the first streamer discharge. The lower bound velocity estimate given above is then not directly comparable to the velocity obtained in the triple junction simulation, as only primary streamers are considered in the simulations. A second explanation is that the first discharge captured by the PMT occurred on the backside of the rod. Since the PMT was placed at a different position than the camera, only the PMT was able to record it. In this situation, the impact of the primary streamer exerted on the secondary streamer depends on the relative distance between the discharges. Due to lack of time, these theories were not investigated further. It must also be noted that charges from previous discharges were most likely present on the dielectric rod prior to the measurements. In this respect, the lower bound estimate given above is only vaguely related to the numerical simulations.

Others have also measured the velocities of streamers propagating along dielectric surfaces. However, as far as the author is concerned, all previous measurements are performed with larger gap sizes. For example, Liming et al. [52] have measured streamer velocities along dielectric surfaces using a 10 cm gap and average field strengths between 4.5 kV/cm and 7.5 kV/cm. Depending on the dielectric material and the field strength, the streamer velocities was found to be in the range 0.1 – 1.2 mm/ns. Akyuz et al. [53] came to similar conclusions in their measurements of surface streamer velocities in a 35 cm gap, using comparable average electric field strengths. In the experiments performed in this work, the average electric field strength is  $18.5 \text{ kV}/1 \text{ cm} = 18.5 \text{ kV/cm}$ . This is one order of magnitude higher than what was used in the cited experiments. With increasing field strength, more ionization occur in and around the streamer head, giving increased propagation velocity. In this respect, a higher streamer velocity than what was found in these measurements should be expected. This means that a discharge velocity above the lower bound estimate  $v = 1 \text{ mm/ns}$  is to be expected, regardless whether the streamer is a primary or a secondary streamer. However, from the experimental data it is not possible to determine the discharge velocity with a better accuracy.

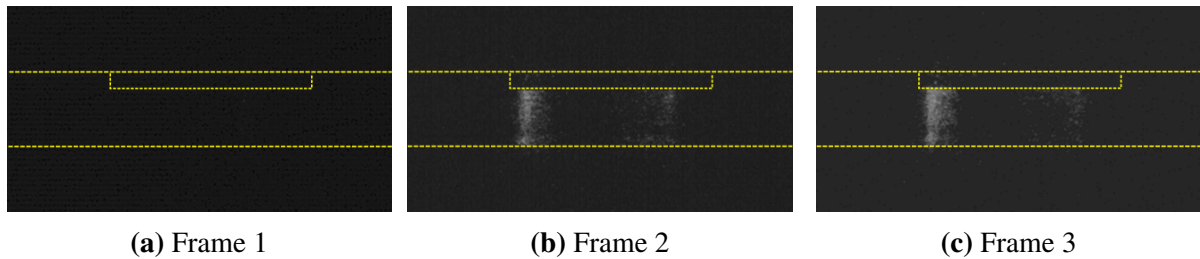


**Figure 5.1:** Image series depicting a discharge. The exposure time used to obtain frame 1 was 190 ns, whereas the exposure time used for frame 1 and 2 was 10 ns.

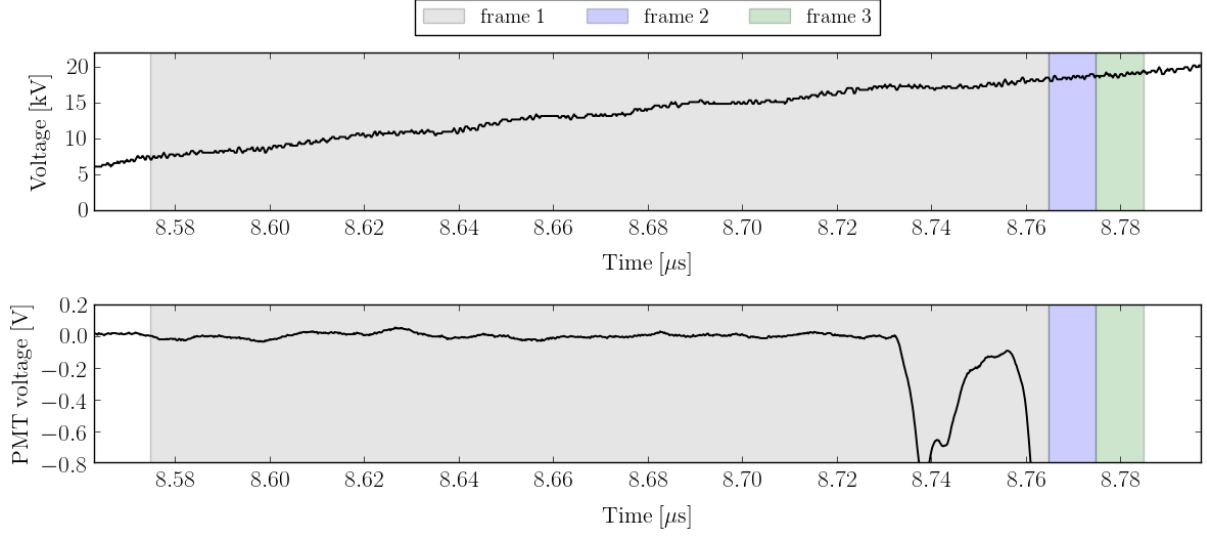


**Figure 5.2:** Top plot: The anode voltage measured in the experiment. Bottom plot: The recorded PMT signal. A coloring scheme is applied to indicate the temporal positioning of the frames presented in figure 5.1 with respect to the above plots.

## 5.2 Simulations

Through numerous simulations using the configurations described in the previous chapter, several numerical errors were identified in the streamer code. Mostly, the nature of the errors was very technical and their specifics will not be elaborated here. The search for numerical errors was initiated because the streamers were observed to be very thin when propagating close to dielectric surfaces. Their widths were found to only span across a few cells when using fine spatial resolutions of  $1 - 3 \mu\text{m}$ . Behind the streamers, a thin layer of positive charge is left just outside of the surface (see the next sections for plots).

Ahead of performing the simulations, it was expected that the streamers should retain a somewhat wider profile when propagating along dielectric surfaces, due to incoming electron avalanches produced as a result of photoionization. These electron avalanches were presumed to have an effect of “pulling” the streamer head away from the dielectric. At equilibrium, the “pull” from these avalanches should be equal to the “pull” towards the dielectric surface from the secondary electrons produced by photoemission and ion bombardment. These effects have been demonstrated earlier in low pressure nitrogen, both experimentally and through simulations [1]. In pure nitrogen, photoionization is suppressed because of the lack of oxygen. Under such conditions, the streamers were found to be very thin and exclusively propagate on the dielectric surface. However, when the effect of photoionization was artificially introduced in the simulations in form of a background ionization of  $10^{10}$  electrons/ $\text{cm}^3$ , the diameter of the streamers was found to increase significantly. With abundance of electrons in the surrounding gas, it was shown that the discharges did not have the same affinity towards the dielectric and tended to propagate in the gas rather than on the dielectric surface.

Although several errors in the code were exposed and corrected, none of these were found to have any direct impact on the thickness of the streamers propagating along dielectric surfaces. Also,

most of the bugs were relatively easily fixable, without requiring too much change in the code. However, larger issues were also uncovered. Because of stiffness in the set of coupled equations making up the streamer model, it was found that prohibitively small time steps of the order of  $10^{-13} - 10^{-15}$  s is required for the simulations to run stable when modeling streamer discharges near dielectric surfaces. This is an intrinsic weakness associated with explicit time stepping methods, such as the second order Runge-Kutta scheme used here. In order to maintain stability when using explicit solvers, the sizes of the time steps should match the smallest time scale present, even though satisfactory accuracy could be achieved with a much larger stepsize [83]. When solving a set of equations with a low degree of stiffness, this is usually of no concern, as only one time scale is associated with the solutions. Therefore, the sizes of the time steps required for stability coincide with the stepsizes required for the solver to remain accurate. In contrast, the independent variables on which the solutions to a stiff set of equations depend are associated with two or more very different scales. In such cases, the stepsizes required for stability may be much smaller than the stepsizes required for tolerable accuracy. Subsequently, a large number of “wasteful” time iterations must be performed, simply because the numerics.

The best measure for ensuring numerical stability is to replace the explicit Runge-Kutta method with an implicit method. In contrast to explicit solvers, implicit schemes are known to be unconditionally stable for linear systems. Also in a more general context, implicit methods provide better stability than explicit methods [83]. However, it must be noted that implicit methods are more computationally expensive than explicit schemes. Still, this is a small price to pay in exchange for stability. Furthermore, by allowing larger stepsizes, the reduced number of time steps needed is likely to more than make up for the extra run time associated with an implicit method.

In addition to switching to an implicit time stepper, a reduction in the stiffness associated with the set of equations would also be beneficial. Adopting a logarithmic formulation, such as that used by Singh [2], could lead to reduced stiffness, because large scale differences even out within such a formulation. Moreover, this would also make the code less prone to rounding errors. Another positive effect of using a logarithmic formulation is that the electron and ion densities always remain positive. This is in general not ensured within the current formulation of the drift-diffusion equations (3.4), as the densities may become negative if the “sink” terms become too dominating. In order to prevent this, negative concentrations are explicitly always set to zero.

Another major issue with the code was encountered in the form of memory leakage, limiting the maximal number of time steps possible to about 13 000. An effort was made to locate the memory leakages within the code, and several leakages were indeed discovered. However, debugging such a large code requires time and resources. Unfortunately, this job could not be completed within the time frame of this master’s thesis. The current requirement of very small time steps, in combination with an existing upper limit on the number of time steps allowed, give a relatively small time window in which the simulated streamer discharges can propagate, before the simulations are aborted. Subsequently, only propagation distances of less than one millimeter along dielectric surfaces could be simulated.



### 5.2.1 Triple junction geometry

In this section, the results of a simulation using the described triple junction geometry is presented. The electric field magnitude, the charge density, the electron density and the positive ion density are presented in figure 5.3 and 5.4 at three different times. At  $t = 10.42$  ns, the ion density reaches about  $7 \times 10^{11}$  positive ions/cm<sup>3</sup>. In accordance with experimental observations, as discussed in the theory chapter, this density is high enough to start distorting the background field. When simulating the inception stage and the early stages of streamer propagation, the code was found to run stable, allowing for a time step of the order of  $10^{-12}$ . However, as the streamer propagated towards the dielectric material, smaller and smaller time steps were required.

As seen in figure 5.4a, the densities of electrons and positive ions in the streamer channel are of the order of  $10^{13}$  cm<sup>-3</sup>. As discussed in chapter 2, this is within the typical range observed experimentally. Another characteristic feature which has been discussed earlier on is the existence of a very thin positive charge layer surrounding the streamer channel. This space charge layer is clearly visible in the charge density plot in figure 5.3a and measures about  $10 - 20$   $\mu\text{m}$ .

After the streamer has collided with the dielectric surface, a very thin streamer discharge starts propagating along the dielectric surface. The charge density in the innermost layer of cells is very high, with a maximal value of  $158.3$   $\mu\text{C}/\text{cm}^3$ , as indicated in figure 5.3c. The total width of the streamer only spans over three layers of cells, if the charge density is used as a measure. This means that the diameter is about  $9$   $\mu\text{m}$  (a resolution of  $3.05$   $\mu\text{m}$  was used). Moreover, by studying the charge density plots, the surface streamer is found to move at a velocity  $v = 0.05$  mm/ns. This is far less than what was observed experimentally, where a rough lower bound estimate  $v = 1$  mm/ns was obtained. However, as explained earlier on, the experimental result is not directly comparable with the simulations. Nevertheless, a difference of two orders of magnitudes is significant.

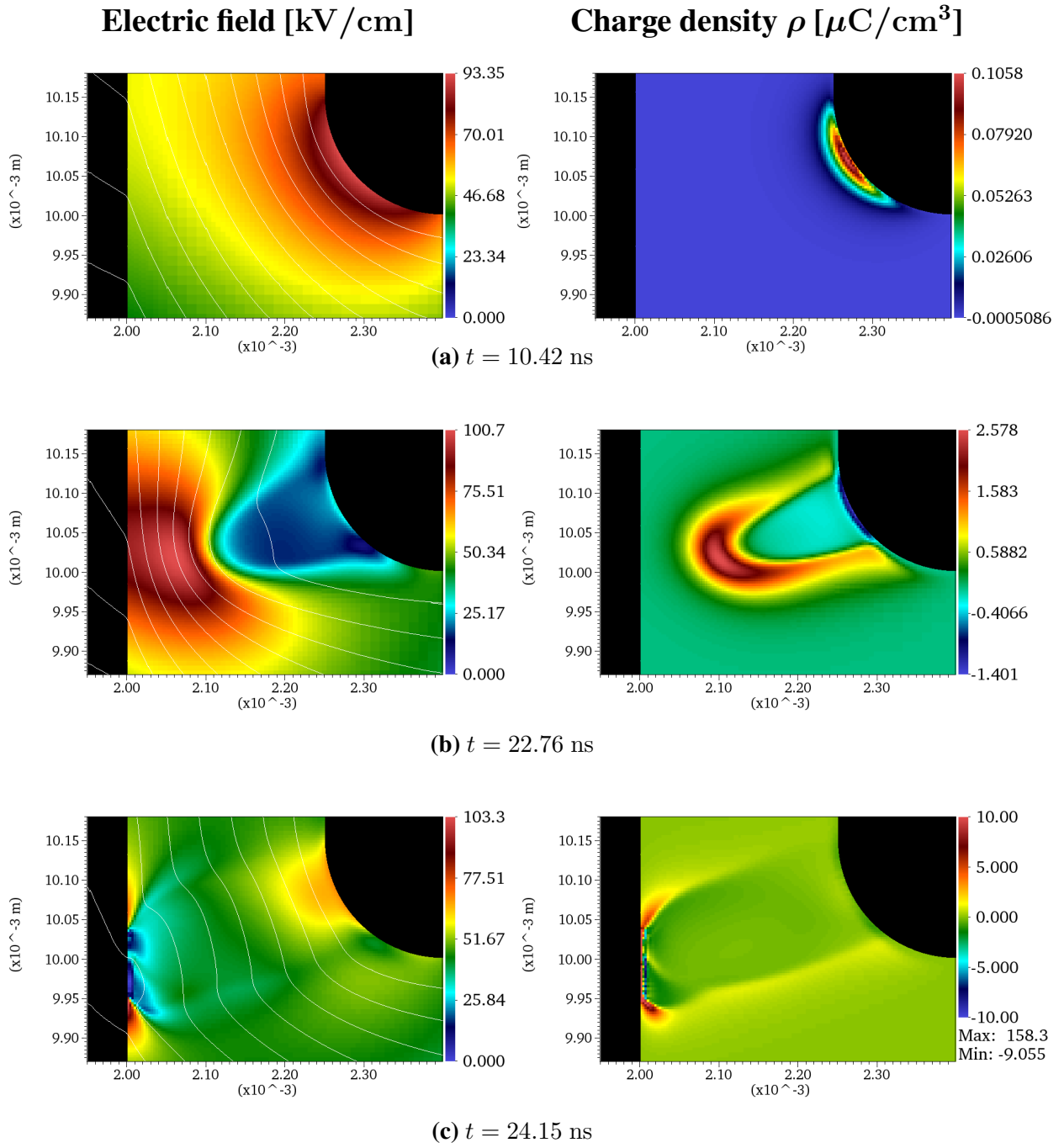


**Figure 5.3:** Zoomed view of the triple junction geometry: The magnitude of the electric field with indicated equipotential lines (left column) and the charge density (right column) are plotted at various times.

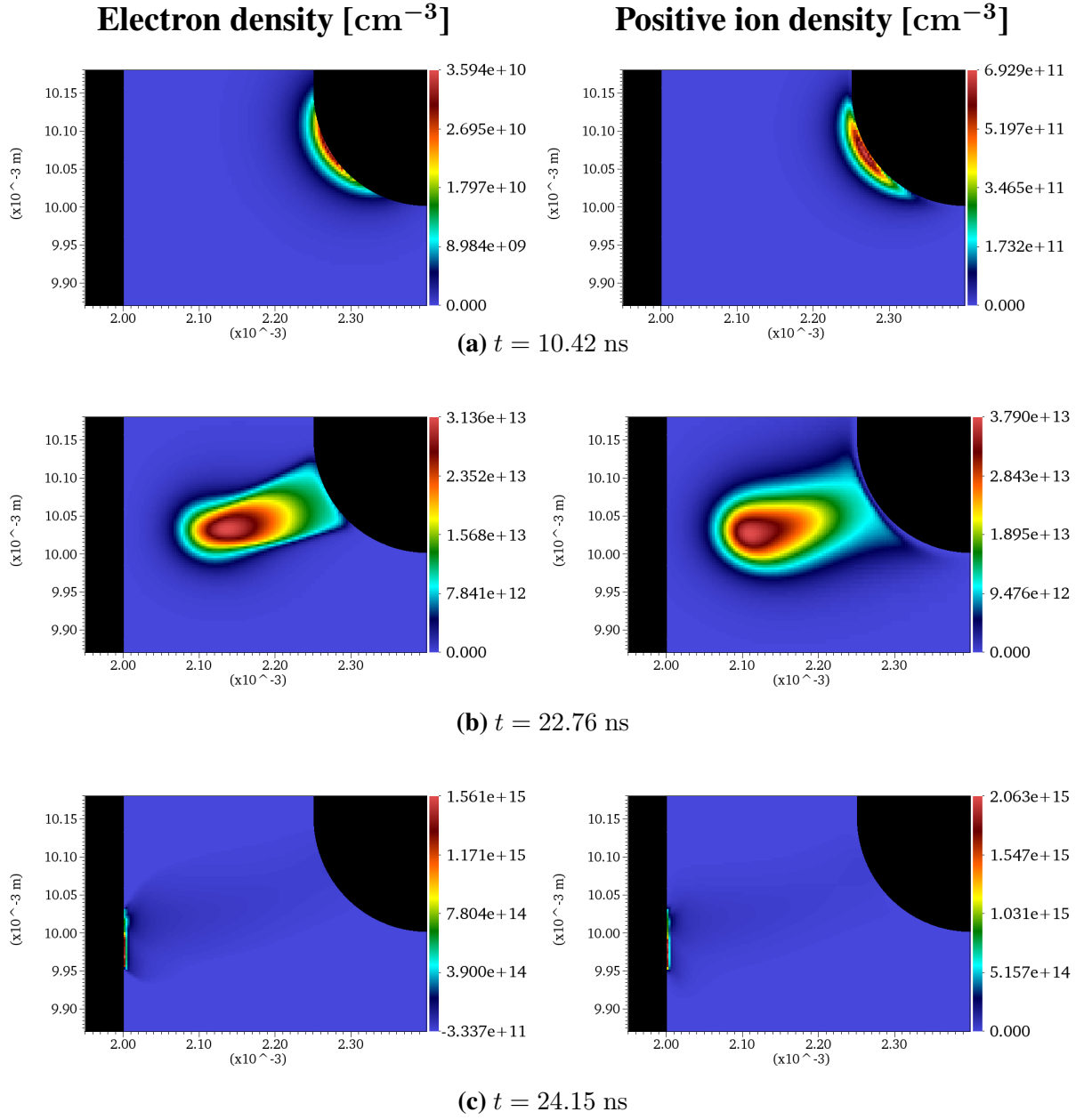


**Figure 5.4:** Zoomed view of the triple junction geometry: The electron density (left column) and the positive ion density (right column) are plotted at various times.

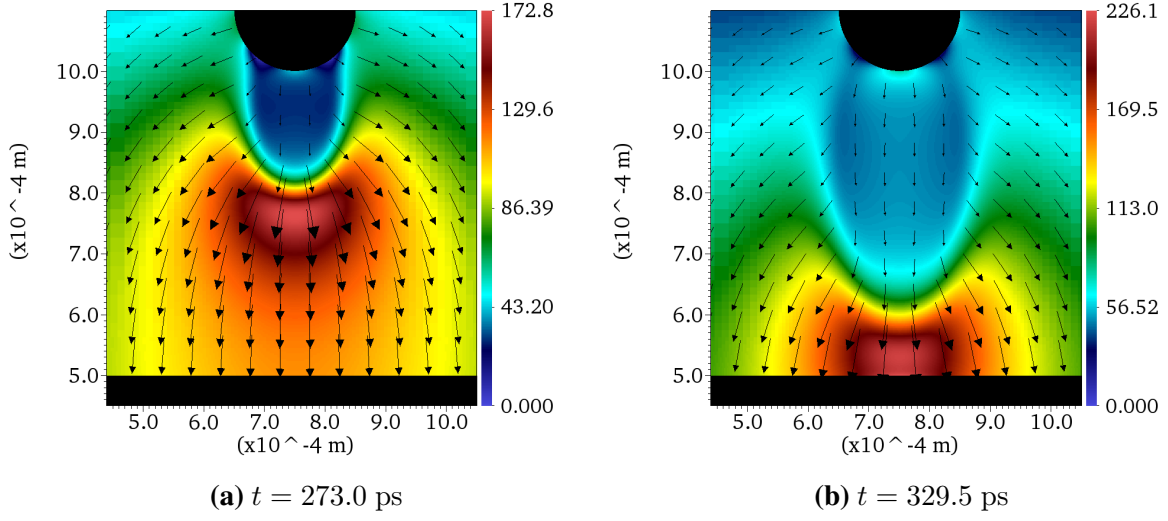
## 5.2.2 Rod-plane geometry

### 5.2.2.1 Propagation in air

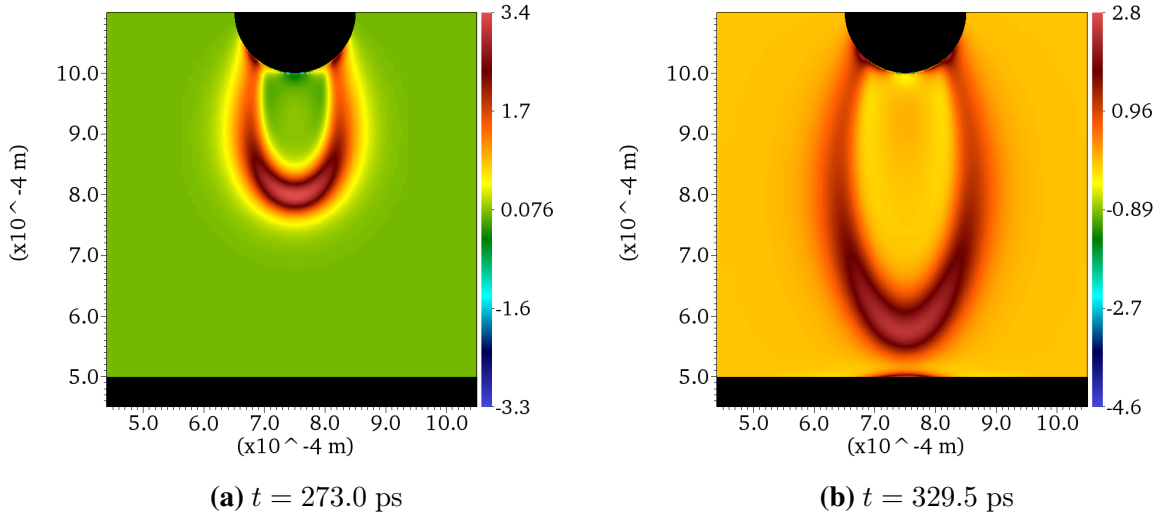
In this section, an analysis of the streamer dynamics in the rod-plane air gap for the simulation when  $\gamma_{\text{ph}} = 1$  is performed. Based on the electric field and charge density plots presented in figure 5.5 and 5.6, the streamer propagates with an average velocity of 2.61 mm/nm. Moreover, measurements of the streamer channel give an approximate channel diameter  $d = 0.29$  mm. Using this diameter value, the empirical streamer formula (2.27) provided by Briels et al. [44] for the streamer velocity yields  $v = 0.04$ . This is significantly lower than what is obtained from the simulation. However, as explained earlier on, it was found that the formula underestimates the velocity of narrow streamers with diameters of 0.20 mm with about a factor of five. Adjusting for this gives  $v = 0.21$  mm/nm, which is still notably lower than what is seen in the simulation. The discrepancy can be explained by the fact that the experimental data was obtained using a much larger gap (40 mm), in addition to a 17% lower anode voltage (5 kV), compared to what is used in the simulation (0.5 mm gap and 6 kV anode voltage). In the experimental case, the average electric field is 0.13 kV/cm. Such a background field is too low to sustain propagation of positive streamers, if compared to the minimal required magnitude stated in section 2.4.3 in chapter 2. This is confirmed by the experiments, where the 0.20 mm streamer only propagated about 8 mm into the air before dissolving. In contrast, the average electric field in the simulation is 120 kV/cm, which is three orders of magnitudes larger than in the experimental case, and more than enough to sustain propagation of positive streamers. Subsequently, the streamer head and the local region around it is subject to a higher degree of ionization, giving a higher streamer propagation velocity, compared to the experimental case. Lastly, it must be noted that the experiments were conducted without the presence of a grounded dielectric plane, as used in the simulations. However, when the streamer is far from the dielectric, the effect of the dielectric is assumed negligible.

An interesting phenomenon can be seen in figure 5.6b. When the positively charged streamer head approaches the dielectric surface, a significant positive layer of space charge is induced just outside of the dielectric. The charge density within this layer is comparable to what is found in the streamer head. Figure 5.7b, visualizing the photon intensity, indicate that the dielectric surface is under strong bombardment of photons as the streamer approaches the surface. This process is believed to liberate a large number of secondary electrons, which subsequently are accelerated towards the streamer head. On their paths, these electrons ionize the gas, and left behind is the observed positive space charge layer.

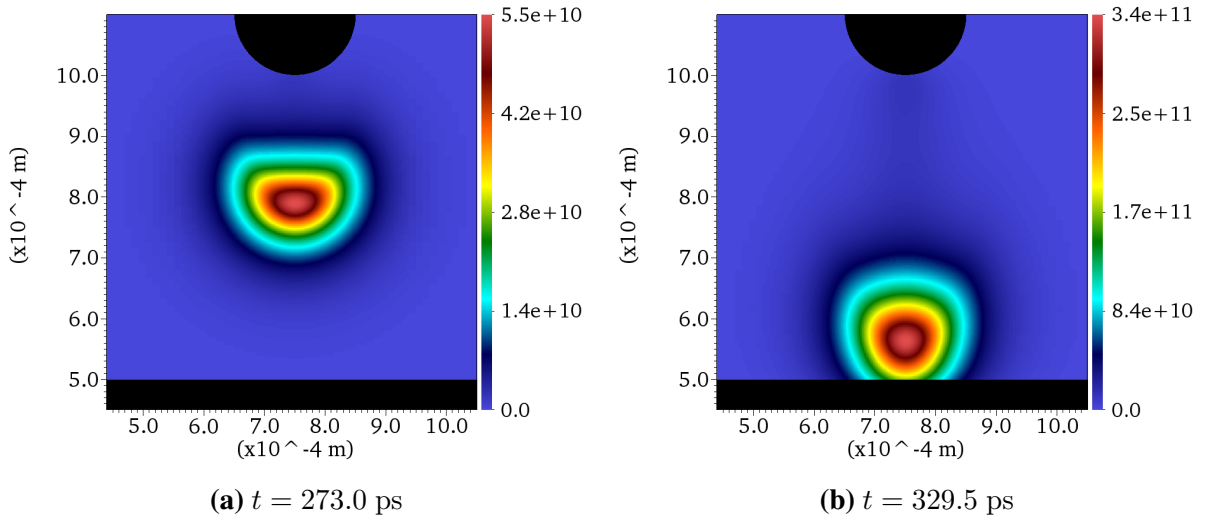
**Zoomed view of the rod-plane geometry.  $\gamma_{\text{ph}} = 1$ .**



**Figure 5.5:** Electric field  $E$  [kV/cm]



**Figure 5.6:** Charge density  $\rho$  [ $\mu\text{C}/\text{cm}^3$ ]

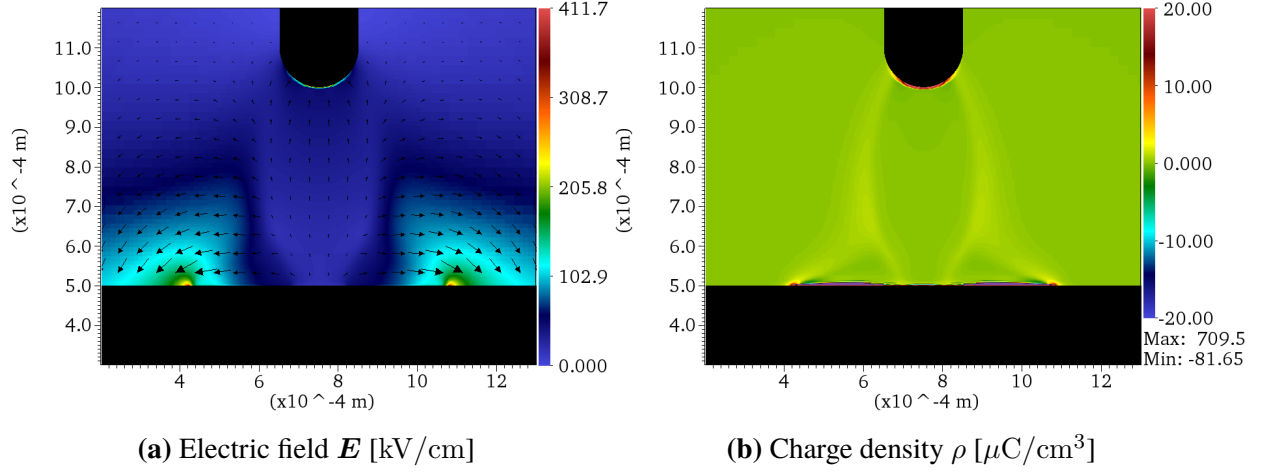
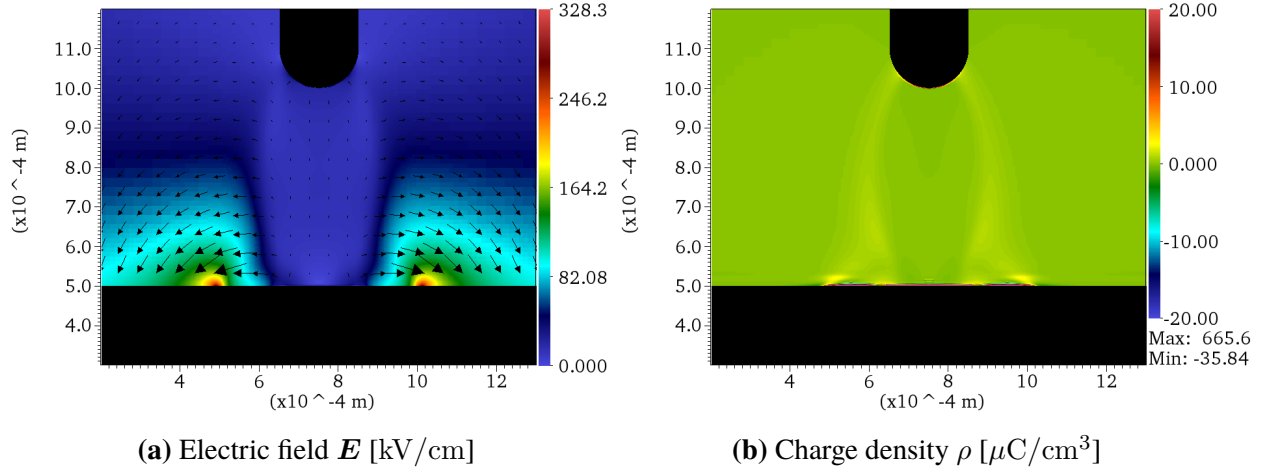
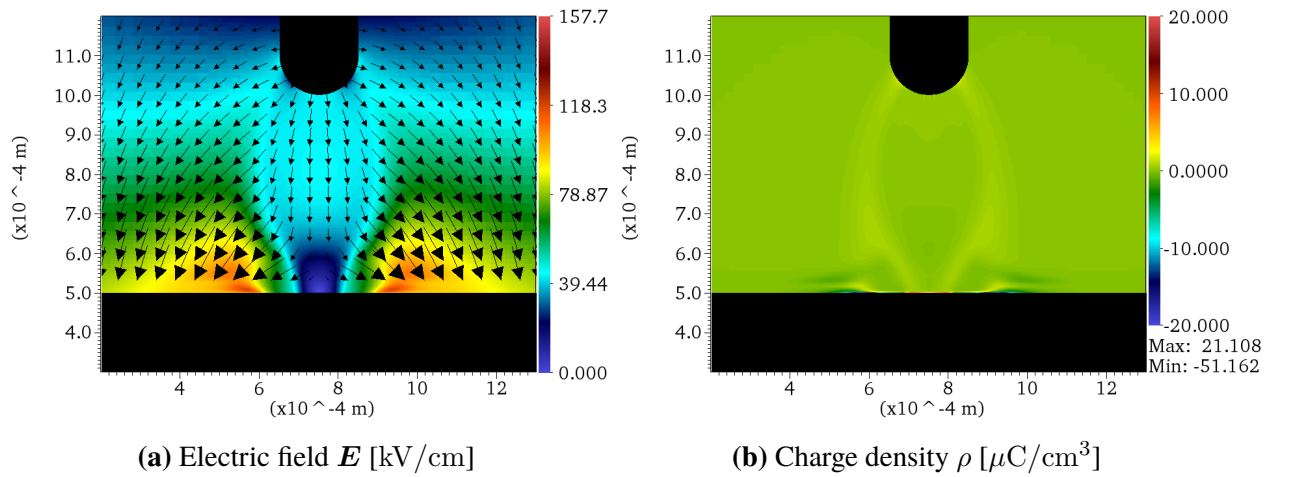


**Figure 5.7:** Photon intensity [ $\text{cm}^{-3}$ ]

### 5.2.2.2 Propagation along the dielectric surface

In figure 5.8, 5.9 and 5.10, snapshots of the electric field and the charge density is presented for the three respective cases  $\gamma_{ph} = 0.1$ ,  $\gamma_{ph} = 1$  and  $\gamma_{ph} = 10$  at time  $t \approx 418$  ps. Here, the streamer has collided with the dielectric surface, and two surface discharges is seen propagating in each direction. The plots look quantitatively similar for the two first cases. However, for the latter case, the plots are distinctly different. When using  $\gamma_{ph} = 0.1$  and  $\gamma_{ph} = 1$ , the dielectric surface is significantly positively charged upon the streamer collision, and the maximal surface charge densities reaches a value of about  $2 \mu\text{C}/\text{cm}$  in both cases. In fact, the accumulated charge on the dielectric surface causes the field within the streamer channel to be reversed. This was very unexpected, but the phenomenon is assumed to be enabled by the free outflux condition used on the massive species. In other words, almost the whole positively charged streamer head is poured onto the dielectric surface, making the surface more positively charged than the anode. However, such a phenomenon is not observed for the case when  $\gamma_{ph} = 10$ . In this case, photoemission is strong enough for a large number of electrons to be emitted from the dielectric surface long before the streamer actually gets close to the dielectric. Due to attachment, a negative space charge layer is formed next to the dielectric surface, as portrayed in figure 5.11a. When the streamer eventually collides with the surface, the electric field is strongly reduced due to the presence of the negative space charge layer (see figure 5.11b). Compared to the case where  $\gamma_{ph} = 1$ , as displayed in figure 5.5a, the maximal magnitude of the electric field is reduced by a factor of 12. However, the charging of the dielectric as the streamer collides with the surface is in fact even more significant than described for the two other cases, and the surface charge density reaches a maximal value of  $4.7 \mu\text{C}/\text{cm}$ . However, field screening in the streamer channel due to the remains of the space charge layer next to the dielectric surface prevent field reversal from occurring.

In all three cases, the emerging surface streamers are very thin, as observed for the streamer in the triple junction simulation. However, an even finer resolution of  $1.47 \mu\text{m}$  was used in the rod-plane simulations. This suggest that the very narrow width of the streamers is not simply caused by poor resolution. A more thorough discussion is found in the next section. For the simulations where  $\gamma_{ph} = 0.1$  and  $\gamma_{ph} = 1$ , the electric fields are very localized and strong in the fronts of the surface discharges. Also the charge densities reaches very high values here. In contrast, for the case where  $\gamma_{ph} = 10$ , the fronts are much more spread out in space. Subsequently, both the maximal magnitude of the electric field and the maximal charge densities are much lower than seen in the two other cases.

Figure 5.8:  $\gamma_{\text{ph}} = 0.1$ ,  $t = 418.36$  psFigure 5.9:  $\gamma_{\text{ph}} = 1$ ,  $t = 418.67$  psFigure 5.10:  $\gamma_{\text{ph}} = 10$ ,  $t = 416.83$  ps

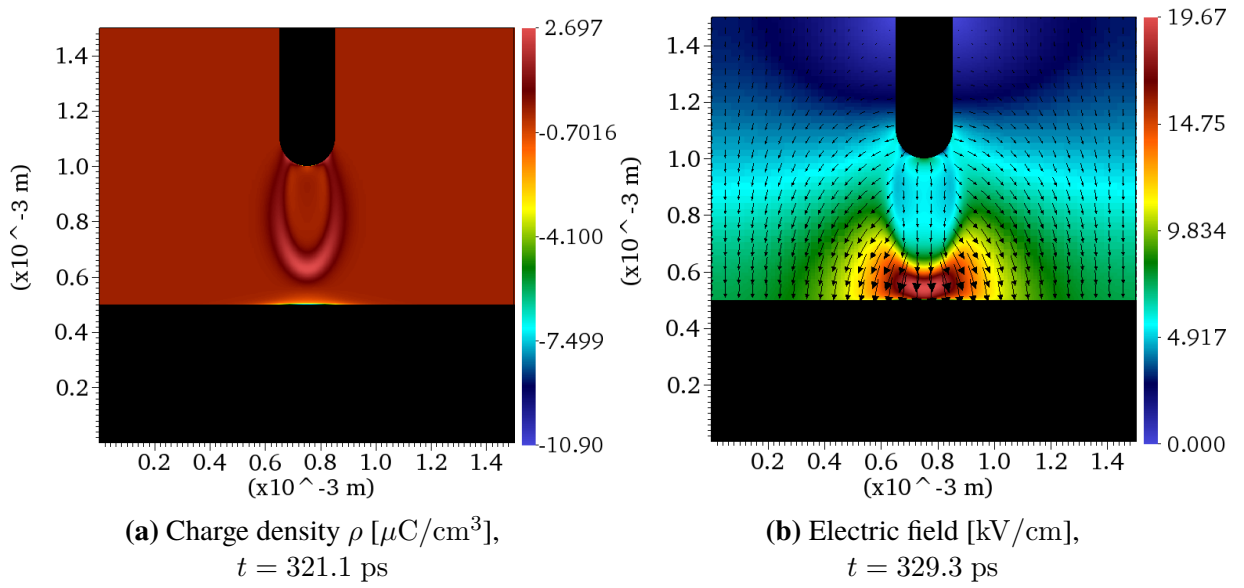


**Figure 5.11:** Snapshot of the charge density just before the streamer is about to collide with the dielectric (a) and the electric field as the streamer is colliding with the surface (b). In this simulation, a photo yield coefficient  $\gamma_{\text{ph}} = 10$  is used. Note that a negative space charge layer is formed next to the dielectric surface as the streamer approaches the dielectric. Upon collision with the surface, the layer of space charge causes the electric field magnitude to be significantly reduced.



## 5.3 Evaluation

In all the simulations performed, the streamers were found to be very thin when propagating along dielectric surfaces. Even when using fine spatial resolutions of about  $1 - 3 \mu\text{m}$ , the widths of the streamers typically only spanned across three layers of cells. The simulated surface discharges are therefore significantly under-resolved. However, it is unlikely that a finer resolution is necessary. The exact cause of the narrow surface streamers is not fully understood, but most likely they develop as a combined effect of the simplistic boundary conditions used on the electron and ion concentrations and the fact that only one photon frequency band is included in the current model. Although the results suggest that the model is adequate for simulating streamers propagating in air, it is most probable too simplistic for satisfactory modeling of photoemission from dielectric surfaces. For example, the rod-plane simulations clearly showed that the presence of a negative layer of space charge, caused by photoemission from the dielectric long before the streamer collided with the surface, had a profound effect on the streamer behavior. With inclusion of an additional lower photon frequency band, this effect would most likely have been observed without using a very high photon yield coefficient, as lower frequency photons are associated with longer absorption lengths. Subsequently, such photons are able to cause photoemission far from where they are created, in contrast to higher frequency photons. Moreover, the rod-plane simulations also revealed that free outflux of charged species may cause extreme phenomena, such as field reversal, to occur. Therefore, a more sophisticated model for charging of dielectrics should be implemented.

A hypothesis is that the development of very thin surface streamers is caused by a self-enhanced process. As seen in the simulations, the streamers propagating on the surfaces of dielectrics are associated with a very small, but densely charged streamer front. The front is as known the main source of photons, but because of its very small size, photon production is essentially confined to a few cells. Thus, only a small number of photons are produced, and since the absorption length of the photon band implemented is relatively small, these photons are not able to produce enough electrons around the streamer head for enabling the streamer to grow in size. This inevitable leads to a reduction in photoemission from the dielectric surface. With fewer electrons available, the streamer becomes even smaller, which again leads to fewer photons being produced, and so on. This process would eventually cause the surface streamers to loose their velocities, and the propagation would most likely stop. However, none of the simulations have been able to run long enough to verify this hypothesis.



# Chapter 6

## CONCLUSION

A novel fluid discharge model has been presented and tested with two different case configurations in a nitrogen-oxygen mixture under normal conditions. In all the simulations, streamers were observed propagating along dielectric surfaces. These streamers were found to be very thin, only spanning across three layers of cells, if the charge density is used as a measurement. A hypothesis is that such a development is caused by a self-enhanced process, occurring as an effect of reduced photon production in the streamer head, due to its small size. Since only one photon band has been implemented in the model, the produced photons are not able to create enough electrons around the streamer head for enabling the streamer to grow in size. With fewer electrons available, the streamer becomes even smaller, which again leads to fewer photons being produced, and so on. Implementation of a second photon band associated with a higher absorption length could provide the necessary ionization around the streamer head needed for the streamers to maintain a wider profile. From simulations performed with various photon yield coefficients, it was found that a yield of 10 gave a different streamer dynamics as the discharges collided with the dielectric surfaces than what was observed when the yield values 0.1 and 1 were used. The different behavior is caused by the presence of a dense negative space charge layer next to the surface, developing long before the streamer collided with the dielectric, due to the strong photoemission. In all the simulations, it was found that the dielectric surfaces were significantly positively charged upon collision of the positive streamers. It was further pointed out that a more sophisticated model should be implemented in order to simulate the charging process more accurately, as a very simplistic model assuming free flux of charges through dielectric surfaces is currently used.

Due to use of an explicit second order Runge-kutta method for advancing the hydrodynamic equations in time, restrictions on the sizes of the time steps had to be followed to avoid instability. Because of stiffness in the equation set, time steps of the order of  $10^{-12} - 10^{-15}$  was found to be required for stability. It is suggested that a logarithmic formulation of the equations could reduce the numerical stiffness. Furthermore, implementation of an implicit method for time-stepping is highly recommended for increased stability, allowing larger time steps to be used. Moreover, it was found that memory leakages within the code caused the simulations to crash after approximately 13 000 time-iterations. Subsequently, streamer propagation along the full

lengths of the dielectric surfaces could not be simulated.

Also experimental work has been presented. A triple junction configuration similar to that used in the simulations was adopted to study propagation of positive streamers. The anode was stressed with a 20 kV 1.2/50  $\mu$ s positive DC pulse, and by means of a high-speed camera with a minimal exposure time of 10 ns, streamer discharges along the dielectric rod was arrested. From the obtained data, a lower bound propagation velocity of 1 mm/ns was estimated, which is two orders of magnitudes higher than what was found numerically (0.05 mm/ns). However, it must be noted that excess charge present on the rod from earlier experiments could have influenced the streamer propagation velocity found experimentally. Therefore, these results are not directly comparable. However, the data do support the theory outlined above, i.e. that missing photoionization in the simulations causes the surface streamers to be unphysically thin. It is a known fact that wider streamers tend to propagate with higher velocities than narrow streamers.

# BIBLIOGRAPHY

- [1] A. A. Dubinova, *Modeling of streamer discharges near dielectrics*. PhD thesis, Eindhoven University of Technology, 2016.
- [2] S. Singh, *Computational framework for studying charge transport in high - voltage gas - insulated systems*. PhD thesis, Chalmers University of Technology, 2015.
- [3] U. Ebert, C. Montijn, T. M. P. Briels, W. Hundsdorfer, B. Meulenbroek, A. Rocco, and E. M. van Veldhuizen, “The multiscale nature of streamers,” *Plasma Sources Science and Technology*, vol. 15, no. 2, pp. S118–S129, 2006.
- [4] A. Bourdon, V. P. Pasko, N. Y. Liu, S. Célestin, P. Ségur, and E. Marode, “Efficient models for photoionization produced by non-thermal gas discharges in air based on radiative transfer and the Helmholtz equations,” *Plasma Sources Science and Technology*, vol. 16, no. 3, pp. 656–678, 2007.
- [5] U. Kogelschatz, “Dielectric-barrier discharges: Their History, Discharge Physics, and Industrial Applications,” *Plasma Chemistry and Plasma Processing*, vol. 23, no. 1, pp. 1–46, 2003.
- [6] L. A. Rosocha, D. M. Coates, D. Platts, and S. Stange, “Plasma-enhanced combustion of propane using a silent discharge,” in *Physics of Plasmas*, vol. 11, pp. 2950–2956, 2004.
- [7] M. G. McHarg, H. C. Stenbaek-Nielsen, and T. Kammae, “Observations of streamer formation in sprites,” *Geophysical Research Letters*, vol. 34, no. 6, pp. 1–5, 2007.
- [8] C. Tran Duy, N. Bonifaci, A. Denat, O. Lesaint, L. Caliap, A. Girodet, B. Gelloz, and P. Ponchon, “Partial discharges at a triple junction metal/solid insulator/gas and simulation of inception voltage,” *Journal of Electrostatics*, vol. 66, no. 5-6, pp. 319–327, 2008.
- [9] K. R. Venna and H. H. Schramm, “Simulation analysis on reducing the electric field stress at the triple junctions & on the insulator surface of the high voltage vacuum interrupters,” *Proceedings - International Symposium on Discharges and Electrical Insulation in Vacuum, ISDEIV*, pp. 53–56, 2014.
- [10] H. C. Miller, “Flashover of Insulators in Vacuum Review of the Phenomena and Techniques to Improve Holdoff Voltage,” *IEEE Transactions on Electrical Insulation*, vol. 28, no. 4,

pp. 512–527, 1993.

- [11] M. Akyuz, *Positive streamer discharges in air and along insulating surfaces : experiment and simulation*. PhD thesis, Uppsala University, 2002.
- [12] G. E. Georghiou, A. P. Papadakis, R. Morrow, and A. C. Metaxas, “Numerical modelling of atmospheric pressure gas discharges leading to plasma production,” *Journal of Physics D: Applied Physics*, vol. 38, no. 20, pp. R303–R328, 2005.
- [13] R. Marskar, “Three-dimensional fluid plasma simulations on adaptive grids with internal boundaries,” 2017. In preparation.
- [14] V. I. Kolobov and R. R. Arslanbekov, “Towards adaptive kinetic-fluid simulations of weakly ionized plasmas,” *Journal of Computational Physics*, vol. 231, no. 3, pp. 839–869, 2012.
- [15] D. Tskhakaya, K. Matyash, R. Schneider, and F. Taccogna, “The particle-in-cell method,” *Contributions to Plasma Physics*, vol. 47, no. 8-9, pp. 563–594, 2007.
- [16] Shen C., *Rarefied Gas Dynamics*. Berlin: Springer, 2005.
- [17] S. Zabelok, R. Arslanbekov, and V. Kolobov, “Adaptive kinetic-fluid solvers for heterogeneous computing architectures,” *Journal of Computational Physics*, vol. 303, pp. 455–469, 2015.
- [18] R. K. Crockett, P. Colella, and D. T. Graves, “A Cartesian grid embedded boundary method for solving the Poisson and heat equations with discontinuous coefficients in three dimensions,” *Journal of Computational Physics*, vol. 230, no. 7, pp. 2451–2469, 2011.
- [19] K. C. Kao, *Dielectric Phenomena in Solids*. San Diego: Academic Press, 2004.
- [20] P. Osmokrovic, M. Vujisic, K. Stankovic, A. Vasic, and B. Loncar, “Mechanism of electrical breakdown of gases for pressures from  $10^{-9}$  to 1 bar and inter-electrode gaps from 0.1 to 0.5 mm,” *Plasma Sources Science and Technology*, vol. 16, no. 3, pp. 643–655, 2007.
- [21] D. Xiao, *Gas Discharge and Gas Insulation*, vol. 6. Berlin: Springer, 2016.
- [22] J. M. Meek and J. D. Craggs, *Electrical Breakdown of Gases*. London: Clarendon Press, 1953.
- [23] E. Kuffel, W. Zaengl, and J. Kuffel, *High Voltage Engineering*. Oxford: Newnes, 2 ed., 2000.
- [24] J. S. Townsend, *The Theory of Ionisation of Gases by Collision*. London: Constable & Company, 1910.
- [25] L. B. Loeb and J. M. Meek, “The mechanism of spark discharge in air at atmospheric pressure. I,” *Journal of Applied Physics*, vol. 11, no. 6, pp. 438–447, 1940.
- [26] L. B. Loeb and J. M. Meek, “The mechanism of spark discharge in air at atmospheric pressure. II,” *Journal of Applied Physics*, vol. 11, no. 7, pp. 459–474, 1940.
- [27] H. Raether, *Electron avalanches and breakdown in gases*. London: Butterworths, 1964.

- [28] J. M. Meek, "A theory of spark discharge," *Physical Review*, vol. 57, no. 8, pp. 722–728, 1940.
- [29] G. V. Naidis, "Dynamics of streamer breakdown of short non-uniform air gaps," *Journal of Physics D: Applied Physics*, vol. 38, no. 21, pp. 3889–3893, 2005.
- [30] R. E. Jorgenson, L. K. Warne, A. A. Neuber, J. Krile, J. Dickens, and H. G. Krompholz, "Effect of dielectric photoemission on surface breakdown: An LDRD report," tech. rep., Sandia National Laboratories, 2003.
- [31] C. Vernon, *The Lightning Flash*. London: The Institution of Engineering and Technology, 2 ed., 2014.
- [32] I. Gallimberti, "The mechanism of the long spark formation," *Le Journal de Physique Colloques*, vol. 40, no. C7, pp. C7–193–C7–250, 1979.
- [33] H. B. Michaelson, "The work function of the elements and its periodicity," *Journal of Applied Physics*, vol. 48, no. 11, pp. 4729–4733, 1977.
- [34] L. K. Warne, R. E. Jorgenson, and S. D. Nicolaysen, "Ionization Coefficient Approach to Modeling Breakdown in Nonuniform Geometries," tech. rep., Sandia National Laboratories, 2003.
- [35] I. A. Abroyan, M. A. Ereemeev, and N. N. Petrov, "Excitation of electrons in solids by relatively slow atomic particles," *Soviet Physics-Uspeski*, vol. 10, no. 3, pp. 332–367, 1967.
- [36] F. B. Dunning, A. C. H. Smith, and R. F. Stebbings, "Secondary electron ejection from metal surfaces by metastable atoms. I. Measurements of secondary emission coefficients using a crossed beam method," *Journal of Physics B: Atomic and Molecular Physics*, vol. 4, no. 12, pp. 1683–1695, 1971.
- [37] F. B. Dunning and A. C. H. Smith, "Secondary electron ejection from metal surfaces by metastable atoms. II. Measurements of secondary emission coefficients using a gas cell method," *Journal of Physics B: Atomic and Molecular Physics*, vol. 4, no. 12, pp. 1696–1710, 1971.
- [38] R. H. Fowler and L. Nordheim, "Electron Emission in Intense Electric Fields," *Proceedings of the Royal Society A: Mathematical, Physical and Engineering Sciences*, vol. 119, no. 781, pp. 173–181, 1928.
- [39] P. Osmokrovic, T. Zivic, B. Loncar, A. Vasic, and N. Arsic, "The validity of the similarity law for the electrical breakdown of gases," *Digest of Technical Papers-IEEE International Pulsed Power Conference*, vol. 15, no. 4, pp. 431–434, 2007.
- [40] K. Petcharaks, "A contribution to the streamer breakdown criterion," *11th International Symposium on High-Voltage Engineering (ISH 99)*, vol. 1999, no. 3, pp. v3–19–v3–19, 1999.
- [41] A. Pedersen, "On the Electrical Breakdown of Gaseous Dielectrics: An Engineering Approach," *IEEE Transactions on Electrical Insulation*, vol. 24, no. 5, pp. 721–739, 1989.

- [42] F. Mauseth, J. S. Jørstad, and A. Pedersen, “Streamer inception and propagation for air insulated rod-plane gaps with barriers,” in *2012 Annual Report Conference on Electrical Insulation and Dielectric Phenomena*, (Montreal), pp. 729–732, 2012.
- [43] P. Ségur, A. Bourdon, E. Marode, D. Bessieres, and J. H. Paillol, “The use of an improved Eddington approximation to facilitate the calculation of photoionization in streamer discharges,” *Plasma Sources Science and Technology*, vol. 15, no. 4, pp. 648–660, 2006.
- [44] T. M. P. Briels, J. Kos, G. J. J. Winands, E. M. van Veldhuizen, and U. Ebert, “Positive and negative streamers in ambient air: measuring diameter, velocity and dissipated energy,” *Journal of Physics D: Applied Physics*, vol. 41, no. 23, p. 234004, 2008.
- [45] T. Christen, H. Böhme, A. Pedersen, and A. Blaszczyk, “Streamer Line Modeling,” in *Scientific Computing in Electrical Engineering SCEE 2010*, pp. 173–181, Berlin: Springer, 2012.
- [46] J. Qin and V. P. Pasko, “On the propagation of streamers in electrical discharges,” *Journal of Physics D: Applied Physics*, vol. 47, no. 43, p. 435202, 2014.
- [47] É. Lozanskii, “Development of electron avalanches and streamers,” *Uspekhi Fizicheskikh Nauk*, vol. 117, no. 11, p. 493, 1975.
- [48] S. Pancheshnyi, “Photoionization produced by low-current discharges in O<sub>2</sub>, air, N<sub>2</sub> and CO<sub>2</sub>,” *Plasma Sources Science and Technology*, vol. 24, no. 1, p. 015023, 2014.
- [49] N. Liu and V. P. Pasko, “Effects of photoionization on propagation and branching of positive and negative streamers in sprites,” *Journal of Geophysical Research: Space Physics*, vol. 109, no. A4, pp. 1–18, 2004.
- [50] A. N. Heays, J. M. Ajello, A. Aguilar, B. R. Lewis, and S. T. Gibson, “The high-resolution extreme-ultraviolet spectrum of N<sub>2</sub> by electron impact,” *The Astrophysical Journal Supplement Series*, vol. 211, no. 2, p. 28, 2014.
- [51] G. Wormeester, S. Pancheshnyi, A. Luque, S. Nijdam, and U. Ebert, “Probing photoionization: simulations of positive streamers in varying N<sub>2</sub>:O<sub>2</sub> mixtures,” *Journal of Physics D: Applied Physics*, vol. 43, no. 50, p. 505201, 2010.
- [52] W. Liming, M. Xiaobo, M. Hongwei, and G. Zhicheng, “Characteristics of streamer propagation along insulation surface: influence of dielectric material and shed configuration,” *20th International Conference on Gas Discharges and their Applications*, pp. 6–10, 2014.
- [53] M. Akyuz, L. Gao, V. Cooray, T. G. Gustavsson, S. M. Gubanski, and A. Larsson, “Positive streamer discharges along insulating surfaces,” *IEEE Transactions on Dielectrics and Electrical Insulation*, vol. 8, no. 6, pp. 902–910, 2001.
- [54] D. J. M. Trienekens, S. Nijdam, and U. Ebert, “Stroboscopic images of streamers through air and over dielectric surfaces,” *IEEE Transactions on Plasma Science*, vol. 42, no. 10, pp. 2400–2401, 2014.
- [55] C. F. Gallo, W. L. Lama, and W. L. Lama, “Classical Electrostatic Description of the Work



- Function and Ionization Energy of Insulators,” *IEEE Transactions on Industry Applications*, vol. IA-12, no. 1, pp. 7–11, 1976.
- [56] K. Kaneto, “Photoelectric Emission and Contact Charging of Some Synthetic High Polymers,” *Japanese Journal of Applied Physics*, vol. 18, no. 1, pp. 1–8, 1979.
- [57] S. Dujko, A. H. Markosyan, R. D. White, and U. Ebert, “High-order fluid model for streamer discharges: I. Derivation of model and transport data,” *Journal of Physics D: Applied Physics*, vol. 46, no. 47, p. 475202, 2013.
- [58] F. J. Alexander and A. L. Garcia, “The Direct Simulation Monte Carlo Method,” *Computers in Physics*, vol. 11, no. 6, pp. 588–593, 1997.
- [59] C. Cercignani, *The Boltzmann Equation and Its Applications*. New York: Springer, 1988.
- [60] Y. V. Serdyuk, “Propagation of Cathode-Directed Streamer Discharges in Air,” in *2013 COMSOL Conference in Rotterdam*, no. 1, pp. 1–5, 2013.
- [61] A. Luque, V. Ratushnaya, and U. Ebert, “Positive and negative streamers in ambient air: modelling evolution and velocities,” *Journal of Physics D: Applied Physics*, vol. 41, no. 23, p. 234005, 2008.
- [62] S. Pancheshnyi, S. M. Starikovskaia, and a. Y. Starikovskii, “Role of photoionization processes in propagation of cathode-directed streamer,” *J. Phys. D: Appl. Phys.*, vol. 34, no. 1, pp. 105–115, 2000.
- [63] S. Pancheshnyi, M. Nudnova, and A. Starikovskii, “Development of a cathode-directed streamer discharge in air at different pressures: Experiment and comparison with direct numerical simulation,” *Physical Review E - Statistical, Nonlinear, and Soft Matter Physics*, vol. 71, no. 1, pp. 1–12, 2005.
- [64] W. G. Min, S. H. Lee, H. S. Kim, and S. Y. Hahn, “Local field approximation modeling of plasma display panels using a flux-corrected transport scheme on an unstructured grid,” *IEEE Transactions on Magnetics*, vol. 39, no. 4 II, pp. 2133–2136, 2003.
- [65] P. Brimblecombe, *Air composition and chemistry*. Cambridge: Cambridge University Press, 2 ed., 1996.
- [66] G. J. M. Hagelaar and L. C. Pitchford, “Solving the Boltzmann equation to obtain electron transport coefficients and rate coefficients for fluid models,” *Plasma Sources Science and Technology*, vol. 14, no. 4, pp. 722–733, 2005.
- [67] A. V. Phelps and L. C. Pitchford, “Anisotropic scattering of electrons by N<sub>2</sub> and its effect on electron transport,” *Physical Review A*, vol. 31, no. 5, pp. 2932–2949, 1985.
- [68] “SIGLO database, <http://www.lxcat.laplace.univ-tlse.fr>, retrieved June 4, 2013.”
- [69] S. a. Lawton and A. V. Phelps, “Excitation of the b  $1\Sigma^+g$  state of O<sub>2</sub> by low energy electrons,” *Journal of Chemical Physics*, vol. 69, no. 3, pp. 1055–1068, 1978.
- [70] “SIGLO database, <http://www.lxcat.laplace.univ-tlse.fr>, retrieved June 4, 2013.”

- [71] R. Morrow and J. J. Lowke, “Streamer propagation in air,” *Journal of Physics D: Applied Physics*, vol. 30, no. 4, pp. 614–627, 1999.
- [72] M. B. Zheleznyak, A. K. Mnatsakanyan, and S. V. Sizykh, “Photoionization of Nitrogen and Oxygen Mixtures By Radiation From a Gas Discharge,” *High Temperature*, vol. 20, p. 357, 1982.
- [73] A. A. Kulikovskiy, “The role of photoionization in positive,” *Journal of Physics D: Applied Physics*, vol. 33, no. 12, pp. 1514–1524, 2000.
- [74] U. Ebert, W. Van Saarloos, and C. Caroli, “Propagation and structure of planar streamer fronts,” *Phys. Rev. E*, vol. 55, no. 2, pp. 1530 – 1549, 1997.
- [75] D. J. Griffiths, *Introduction to Electrodynamics*. Harlow, UK: Pearson, 4th ed., 2014.
- [76] S. G. Midttun, *An embedded boundary method for solving Poisson’s equation with discontinuous coefficients on adaptively refined Cartesian grids*. Specialization project, Norwegian University of Science and Technology (NTNU), 2016.
- [77] A. N. Bhoj and M. J. Kushner, “Avalanche process in an idealized lamp: II. Modelling of breakdown in Ar/Xe electric discharges,” *Journal of Physics D: Applied Physics*, vol. 37, no. 18, pp. 2510–2526, 2004.
- [78] F. Pechereau, J. Jánský, and A. Bourdon, “Simulation of the reignition of a discharge behind a dielectric layer in air at atmospheric pressure,” *Plasma Sources Science and Technology*, vol. 21, no. 5, p. 055011, 2012.
- [79] A. Hallac, G. E. Georgiou, and A. C. Metaxas, “Secondary emission effects on streamer branching in transient non-uniform short-gap discharges,” *Journal of Physics D: Applied Physics*, vol. 36, no. 20, pp. 2498–2509, 2003.
- [80] M. Adams, P. Colella, D. T. Graves, J. Johnson, N. Keen, T. J. Ligocki, D. F. Martin, P. McCorquodale, D. Modiano, P. Schwartz, T. Sternberg, and B. V. Straalen, “Chombo Software Package for AMR Applications -Design Document,” tech. rep., Lawrence Berkeley National Laboratory, 2012.
- [81] P. Colella, D. T. Graves, T. J. Ligocki, G. Miller, D. Modiano, P. O. Schwartz, B. V. Straalen, J. Pilliod, D. Trebotich, M. Barad, B. Keen, A. Nonaka, and C. Shen, “EBChombo software package for cartesian grid, embedded boundary applications,” tech. rep., Lawrence Berkeley National Laboratory, 2003.
- [82] H. Johansen and P. Colella, “A Cartesian Grid Embedded Boundary Method for Poisson ’s Equation on Irregular Domains,” *Journal of Computational Physics*, vol. 85, pp. 60–85, 1998.
- [83] W. H. Press, B. P. Flannery, S. A. Teukolsky, W. T. Vetterling, and P. B. Kramer, *Numerical recipes: the art of scientific computing*. Cambridge: Cambridge University Press, 2 ed., 1987.
- [84] S. Balay, S. Abhyankar, M. Adams, J. Brown, P. Brune, K. Buschelman, L. Dalcin, V. Ei-

- jkhout, W. Gropp, D. Kaushik, M. Knepley, L. C. McInnes, K. Rupp, B. Smith, S. Zampini, H. Zhang, and H. Zhang, “PETSc Web page.” <http://www.mcs.anl.gov/petsc>.
- [85] W. L. Briggs, V. E. Henson, and S. F. McCormick, *A Multigrid Tutorial*. Philadelphia: SIAM, 2nd ed., 2000.
- [86] D. F. Martin and K. L. Cartwright, “Solving Poisson’s Equation using Adaptive Mesh Refinement,” tech. rep., University of California, Berkeley, 1996.
- [87] B. van Leer, “Towards the ultimate conservative difference scheme. V. A second-order sequel to Godunov’s method,” *Journal of Computational Physics*, vol. 32, no. 1, pp. 101–136, 1979.
- [88] R. J. LeVeque, *Numerical Methods for Conservation Laws*. Berlin: Birkhäuser Verlag, 1992.
- [89] P. A. Vitello, B. M. Penetrante, and J. N. Bardsley, “Simulation of negative-streamer dynamics in nitrogen,” *Physical Review E*, vol. 49, no. 6, pp. 5574–5598, 1994.
- [90] M. Frank and A. Klar, “Approximate models for radiative transfer,” *Bulletin of the Institute of Mathematics*, vol. 2, no. 2, pp. 409–432, 2007.
- [91] I. A. Kossyi, A. Y. Kostinsky, A. A. Matveyev, and V. P. Silakov, “Kinetic scheme of the non-equilibrium discharge in nitrogen-oxygen mixtures,” *Plasma Sources Science and Technology*, vol. 1, no. 3, pp. 207–220, 1992.
- [92] H. K. Hygen Meyer, F. Mauseth, M. Husøy, J. Ekeberg, and A. Pedersen, “Breakdown in short rod-plane air gaps under positive lightning impulse stress,” 2017. In preparation.